Master of Science Thesis

Aeroelastic Roll Control for High Aspect Ratio Wings

J.H. van Emden BSc.

February 8, 2013

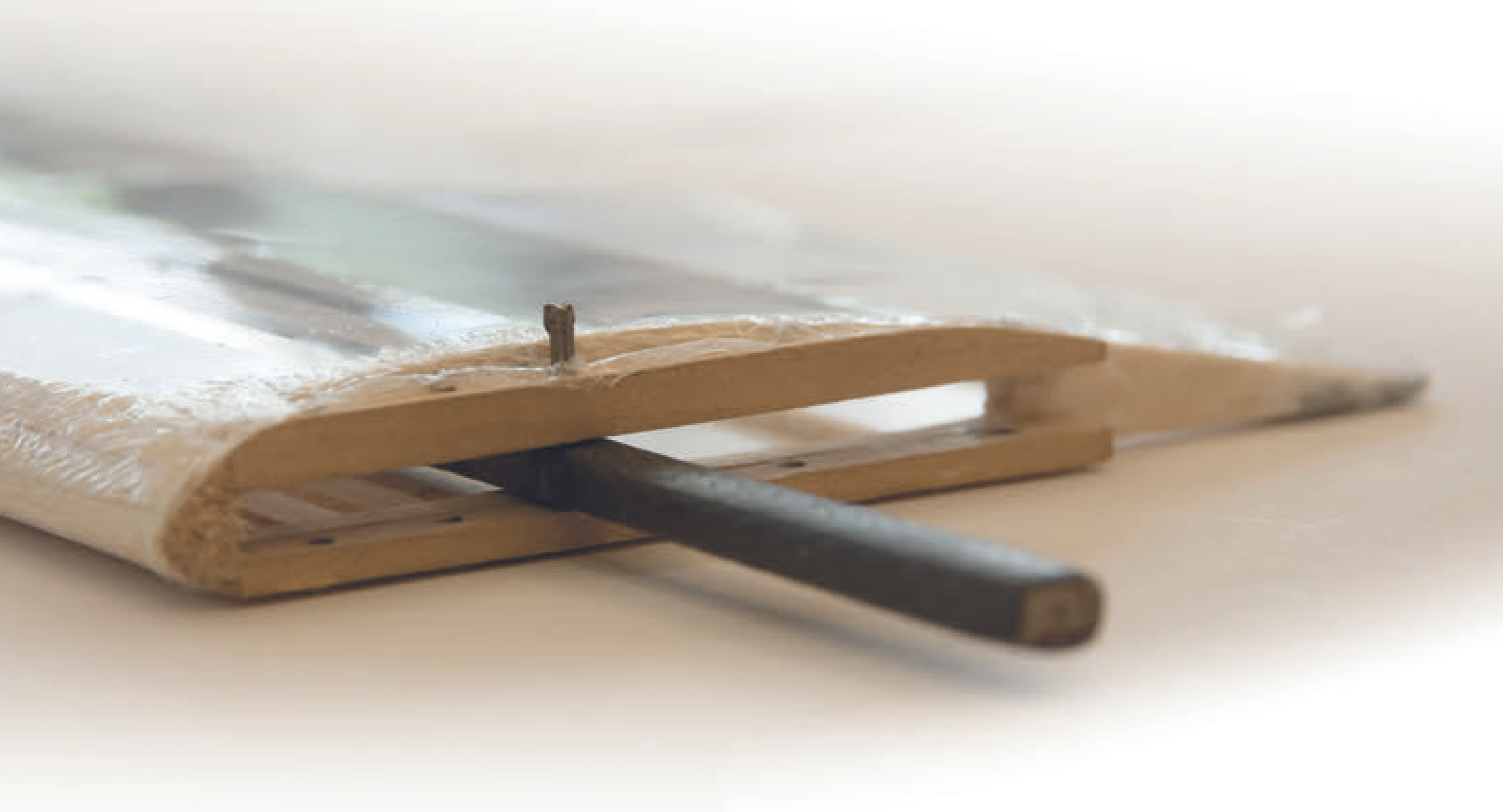

Faculty of Aerospace Engineering · Delft University of Technology

Challenge the future

Aeroelastic Roll Control for High Aspect Ratio Wings

Master of Science Thesis

For obtaining the degree of Master of Science in Aerospace Engineering at Delft University of Technology

J.H. van Emden BSc.

February 8, 2013

Faculty of Aerospace Engineering · Delft University of Technology

Copyright © J.H. van Emden BSc.
All rights reserved.

DELFT UNIVERSITY OF TECHNOLOGY
DEPARTMENT OF
FLIGHT PERFORMANCE & PROPULSION

The undersigned hereby certify that they have read and recommend to the Faculty of Aerospace Engineering for acceptance a thesis entitled **"Aeroelastic Roll Control for High Aspect Ratio Wings"** by **J.H. van Emden BSc.** in partial fulfillment of the requirements for the degree of **Master of Science**.

Dated: February 8, 2013

Chairman: ______________________
Dr.ir. L.L.M. Veldhuis

Supervisor: ______________________
Dr.ir. R. Vos

Reader: ______________________
Dr.ir. R. de Breuker

Summary

Modern aircraft tend to be light and slender. The high aspect ratio reduces the induced drag, increase fuel efficiency, and provide enough lift at low speeds. Therefore such wing types are used for long endurance unmanned aerial vehicles (UAV). A drawback of these wings is that they are more vulnerable for aeroelastic phenomena like divergence, aileron reversal, and flutter. To increase the dynamic pressure, at which one of these phenomena occurs, the stiffness of the wing needs to be increased leading to an increase of the wing weight. Instead of increasing the wing weight, the flexibility of the wing can be used to change the shape of the wing to optimize flight performance or to control the rolling motion of the aircraft. This research area of Active Aeroelastic Wings has grown in the recent years. With this concept, very little control surface motion is used to employ the energy of the airstream to achieve the desirable wing twist.

In this thesis work, an Active Aeroelastic Wing is designed, built and tested in a low-speed wind tunnel. After testing, the possibility to predict the performance accurately with a state-of-the-art modeling tool is verified. First, a qualitative background overview is given about the three most important aeroelastic phenomena. These phenomena are torsional divergence, control reversal, and classical flutter and are described to understand the effects of the different wing parameters on the deformations. Secondly, an overview is given of the techniques that have been used to change the shape of the wing. From these concepts, the sweepable spar method has been chosen. This method uses the ability to change the position of the elastic axis, so that the twist deformations can be increased or decreased. Based on this method, a test article has been built that has similar planform shape as the Global Hawk. Instead of ailerons for roll control, the test article is equipped with an aeroelastic outer wing segment that can change its elastic axis. With this aeroelastic outer wing part, the wing is able to provide a rolling moment.

Afterwards, its performance has been tested in the Open Jet Facility of the TU Delft. The results of the bench tests showed that the moveable spar is able to change the position of the elastic center at the wing tip. With the main spar at different positions, a change in the torsional stiffness of the wing has been observed. During the wind tunnel test the influence of the sweep angle on the rolling moment has been analyzed. The results did not clearly indicate a beneficial effect of the sweep angle on the rolling moment coefficient. Therefore the wing configuration is set to sweep angle of zero degrees to continue the testing. For this configuration, the main spar moved aft on the left and forward on the right wing, the maximum achievable roll helix angle is similar to that of a Boeing 747-200 during cruise. However, the roll performance of the Global Hawk is about five times larger than the test article. Note that aeroelastic effects have been neglected for the Global Hawk, which reduces the aileron control effectiveness.

Finally, the results of the wind tunnel experiments are compared with the simulation results of Proteus. Proteus is an analysis and design framework that uses a non-linear beam model combined with lifting line theory to determine the aeroelastic effects. To analyze the test article some structural and aerodynamic modifications have been made in Proteus, to integrate the effects of a sweepable elastic axis and cambered airfoils. With these modifications the predicted rolling moment coefficient was about 40% smaller compared to the wind tunnel results. Therefore it is concluded that Proteus is currently not able to predict the results accurately.

Acknowledgements

This master thesis would not have been possible without the help of some people.

First of all, I would like to thank my supervisor, Roelof Vos, for his expertise and support during the past year. Furthermore, I would like to thank Hans Weerheim for his help with the manufacturing and bench tests of the test article. During the wind tunnel test Nico van Beek supported me with the test setup. Roeland de Breuker for his expertise on the field of aeroelastic modeling and his help for the adjustments to the modeling tool.

In addition, I would like to thank my (ex)fellow students for their support, and pleasant and busy time in our graduation room. Finally, I want to thank my family for their support during my thesis and my time at the university.

Delft, The Netherlands
February 8, 2013

Jeroen van Emden

Contents

List of Figures

List of Tables

Nomenclature

Latin Symbols

Æ	Aspect Ratio	[-]
A	Cross sectional area	$[\mathrm{m}^2]$
a	Beam width	[m]
a_o	Lift curve slope	[-/rad]
b	Beam height	[m]
B	Tunnel width	[m]
b	Wing span	[m]
b_e	Effective vortex span	[m]
c	Chord	[m]
c_{l_α}	Airfoil lift curve slope	[-/rad]
$c_{m_{ac}}$	Airfoil pitching moment about the aerodynamic center	[-]
C_D	Drag coefficient	[-]
C_m	Moment coefficient	[-]
C_{L_a}	Lift increment of the aileron	[-]
$C_{l_{\delta a}}$	Aileron control effectiveness	[-/rad]
C_l	Rolling moment coefficient	[-]
C_{lp}	Rolling damping coefficient	[-]
C_{LW}	Wing lift coefficient	[-]
C	Wind tunnel cross sectional area	$[\mathrm{m}^2]$
D	Diameter	[m]
E	Young's modulus	[GPa]
EI	Flexural rigidity	$[\mathrm{N\ m}^2]$
e	Eccentricity factor	[-]
F	Force	[N]
G	Shear modulus	[GPa]
GJ	Torsion rigidity	$[\mathrm{N\ m}^2]$

h	Tunnel height	[m]
I	Second moment of inertia	$[\mathrm{m}^4]$
J	Torsion constant	$[\mathrm{m}^4]$
k	Span-to-tunnel-width ratio	[-]
K_θ	Torsional stiffness	[N/rad]
L	Beam length	[m]
L	Lift force	[N]
l	Length	[m]
M	Mach number	[-]
M	Moment	[Nm]
$\dot{p}$	Roll acceleration	$[\mathrm{rad/s}^2]$ or $[\mathrm{deg/s}^2]$
p	Roll rate	[rad/s] or [deg/s]
q	Dynamic pressure	[Pa]
S	Wing area	$[\mathrm{m}^2]$
T	Torque	[Nm]
t	Beam wall thickness	[m]
V	Velocity	[m/s]
y	Spanwise position	[m]

Greek Symbols

α	Angle of attack	[rad] or [deg]
α_δ	Theoretical flap lift factor	[-]
Γ	Circulation	$[\mathrm{m}^2/\mathrm{s}]$
δ	Deflection angle	[rad] or [deg]
δ	Deflection	[m]
δ	Boundary correction factor	[-]
η_δ	Lift effectiveness factor	[-]
θ	Pitch deflection angle	[rad] or [deg]
θ	Twist angle	[rad]
Λ	Sweep angle	[rad] or [deg]
λ	Taper ratio	[-]
λ	Tunnel aspect ratio	[-]
ξ	Chordwise position of the elastic center	$[-]$
ρ	Density	$[\mathrm{kg/m}^3]$
τ_2	Downwash correction factor	[-]

Subscripts

0	Control neutral
AC	Aerodynamic Center
avg	Averge
div	Divergence
elas	Aeroelastic segment (outboard)
e	Equivalent
fixed	Fixed segment (inboard)
rev	Reversal
ξ	Leading edge to elasic center distance
a	Aileron
$c/4$	Quarter chord
dc	Downwash correction
d	Control deflected
f	Flap
i	Inboard position
i	i^{th} element
o	Outboard position
r	Root
sc	Streamline curvature correction
sp	Main spar
t	Tip

Abbreviations

3AS	Active Aeroelastic Aircraft Structures
AAW	Active Aeroelastic Wing
AC	Aerodynamic Center
AFW	Active Flexible Wing
EA	Elastic Axis
FEM	Finite Element Method
ISR	Intelligence, Surveillance and, Reconnaissance
LDPE	Low density polyethylene
LE	Leading Edge
MSL	Mean sea level
OJF	Open Jet Facility
TE	Trailing Edge
UAV	Unmanned Aerial Vehicle

Chapter 1

Introduction

Worldwide usage of unmanned aerial vehicles (UAV) is becoming more popular. The operational costs are lower and the endurance is larger compared to manned vehicles[1]. These savings lead to an increase of UAVs that are used for intelligence, surveillance, and reconnaissance (ISR) missions.

For these ISR missions the endurance of an UAV is a one of the most important characteristic. To obtain such long endurance, this type of UAV is equipped with very high aspect ratio wings to reduce the induced drag, increase fuel efficiency and provide enough lift at low speeds. Examples of these long endurance UAVs are, e.g. the MQ-1 Predator, the MQ-9 Reaper, and the RQ-4 Global Hawk shown in Figure 1.1.

(a) MQ-1 Predator (b) MQ-9 Reaper (c) RQ-4 Global Hawk

Figure 1.1: Long Endurance UAVs[2]

A drawback of high aspect ratio configurations is that their wings are more flexible and therefore more susceptible to aeroelastic phenomena such as divergence, aileron reversal, and flutter. To reduce these effects, the stiffness of the wing has to be increased resulting in an increased wing weight. This increase reduces the amount of payload and fuel. The flexibility of the wing can be decreased but it is more beneficial to use this flexibility to control the aircraft. Additionally the weight saved can be used to increase the payload or fuel capacity. Such type of control is called Active Aeroelastic Wing (AAW) control and uses the twist deformations of the wing to increase or decrease the lift of a wing.

Vos et al.[3] showed that it is possible to get some control on a small UAV by altering the position of the elastic axis. Wind tunnel test showed that the lift coefficient can be increased with 35% and that a 9.1° variation of the twist angle is possible over the rotation range of the sweepable spar. Nevertheless there are no results shown about the variation of the rolling moment coefficient. The goal of this thesis is to verify if the roll performance of the active aeroelastic wing can be predicted accurately enough with a state-of-the-art modeling tool. Therefore a wing has to be designed, built and its roll performance tested in the low-speed wind tunnel. Based on this goal the following research questions are drawn:

Given the same planform parameters, how does an Active Aeroelastic Wing compare to a conventional aileron-controlled wing?

How well can roll performance be predicted using a non-linear beam model combined with lifting line theory?

Report Overview

The report is divided into four main chapters, followed by a conclusive chapter. In Chapter 2 background information is given about the aeroelastic effects that occur on a wing. After the principles of aeroelasticity are introduced, a historical overview is given of concepts that have been used in the past to achieve variable geometries. The chapter ends with a method that is used to calculate the roll performance of the wing.

In Chapter 3 the different experimental setups are defined. First, the creation of the test article is discussed. Herein the internal structure is presented which forms the base, followed by the implementation of the sweepable spar. The section about the test article is finished with the application of the leading edge cover and skin cover. Secondly, the bench test setup is presented that has been used to determine the flexural rigidity and torsional rigidity of the two wing sections. The chapter is concluded with a section about the wind tunnel test setup. This part also consists of a description of the measurement system that has been used. Since the measurements do not fully represent the results in "free air", the applied correction factors are discussed as well.

With the concepts discussed, the modeling of the test article is presented in Chapter 4. An analysis tool is selected that is capable to model the behavior of the sweepable main spar. The necessary modifications are presented that have been included in the selected tool, to simulate the test article.

The results of the performed tests are presented in Chapter 5. The results of the bench tests are presented first, followed by the results of the design and simulation program. Then, the results of the wind tunnel tests are shown. Finaly, the results of the dynamic tests are discussed. In the final section the results of the simulation are compared with the wind tunnel test results, followed by a comparison based on the roll performance of test article with the Global Hawk and Boeing 747-200.

Finally, the conclusion and recommendations are presented in Chapter 6 that follow from the discussion and comparison of the obtained results.

Chapter 2

Background Information

This chapter serves as background information for the research that is done for this thesis. First, a qualitative discussion is given in Section 2.1 of the different aeroelastic phenomena to identify the influence of some wing parameters. In Section 2.2 an overview of different wing geometry manipulation technologies is given, varying from the swing wing to the F/A-18 Active Aeroelastic Wing, which have been used in the past. Finally, a quantitative description is given in Section 2.3 of the parameters that are needed to compare the roll performance.

2.1 Aeroelastic Phenomena

Modern aircraft tend to be light and slender. This reduces the induced drag and tends to increase the structural flexibility at the same time. As a result of the structural flexibility, aeroelastic phenomena may arise when structural deformations induce additional aerodynamic forces. These additional aerodynamic forces could produce extra structural deformations which induce even larger aerodynamic forces. This phenomenon in which interaction occurs between aerodynamic flows and elastic structures is called aeroelasticity. Such interactions may tend to become smaller and smaller until a condition of stable equilibrium is reached, or they may tend to diverge and destroy the structure.

However the term aeroelasticity is not completely descriptive since many important aeroelastic phenomena involve inertial forces as well as aerodynamic and elastic forces. Therefore earoelastic phenomena can be divided into two groups, dynamic and static phenomena. Interactions among inertia, aerodynamic, and elastic forces are involved by dynamic phenomena. The static group only involves the interactions between aerodynamic and elastic forces.

In Figure 2.1 Collar's triangle[4] is shown, it is used for visualizing aeroelastic problem types. At the vertices of the triangle the three types of forces are placed, aerodynamic, elastic and inertia, represented by A, E, and I. On the diagram each aeroelastic phenomenon can be located according

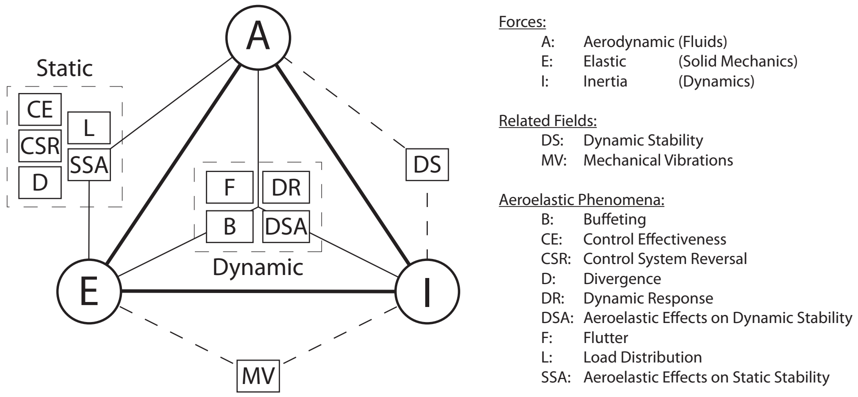

Figure 2.1: Collar's Triangle

to its relation to the three vertices. Static aeroelastic phenomena such as wing divergence, D, lie outside the triangle on the upper left side, as they involve only aerodynamic and elastic forces. Dynamic aeroelastic phenomena (e.g. flutter (F)), lie within the triangle, since they involve all three types of forces. The most important aeroelastic phenomena are described in the upcoming section.

2.1.1 Torsional Divergence

The first type of aeroelastic instability that was recognized and understood was divergence. It is obvious that a perturbation in the angle of attack α tends to increase the deflection angle θ and thus also the angle of attack and lift force L which is shown in Figure 2.2. If the torsional stiffness K_θ is large enough to resist the pitching moment, there are no consequences. Nevertheless as the dynamic pressure q increases, the aerodynamic forces become larger despite the fact that the spring is unchanged. That results in an increase of the deflection angle.

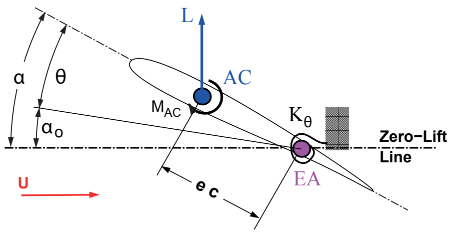

Figure 2.2: Typical section for the divergence problem [5]

From Figure 2.2 can be seen that the dynamic pressure, q_{div}, when torsional divergence occurs, depends on the distance between the aerodynamic center (AC) and elastic axis (EA) and the torsional stiffness. If the aerodynamic center is positioned downstream of the elastic axis, i.e. $e \leqslant 0$, the configuration is unconditionally stable. Whereas the increased lift force is always reduced by a decrease of the angle of attack. When the aerodynamic center is in front of the elastic axis, i.e. $e > 0$, the configuration is conditionally stable depending on the torsional stiffness K_θ.

2.1.2 Control Reversal

The actuation of trailing-edge control devices normally changes the pressure distribution so that the center of pressure shifts aft. Combining this with Figure 2.3a it becomes clear that a positive control (downwards) deflection gives therefore a nose-down pitching moment that tends to reduce the angle of attack of the configuration, shown in Figure 2.3b, as the torsional stiffness K_θ is unchanged. When a certain speed q_{rev} is reached a positive control deflection decreases the angle of attack sufficiently enough to have no change in lift force. At higher speeds, the decrease in angle of attack can be large enough to decrease the lift on the wing such that control is reversed.

When the same structural design is applied to a wing with a larger aspect ratio, the torsional stiffness of this wing is lower (shown in Appendix A). Therefore the control reversal velocity is lower. To improve the control reversal velocity, the torsional stiffness needs to be increased. As a consequence the weight of the wing is increased. [7]

2.1.3 Flutter

Flutter is a word used to describe self-sustained oscillations arising from fluid–structure interactions. Meaning that under certain conditions the oscillations can grow without bound. By plotting the

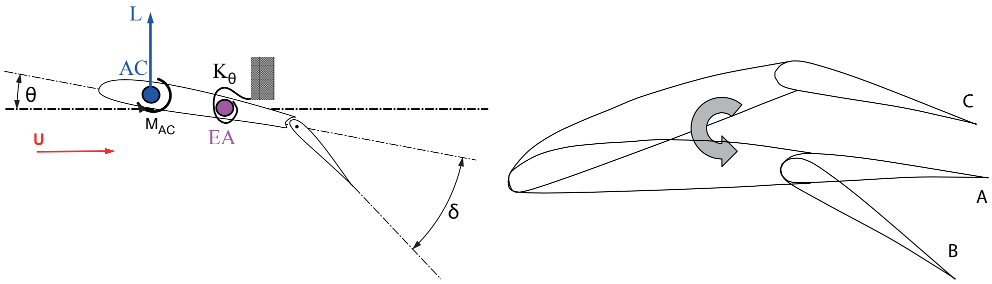

(a) Typical section for the control reversal problem[5]

(b) Nose-down pitching moment[6]

Figure 2.3: Aileron reversal

flutter points in a velocity–altitude diagram, a "safe" operating range can be determined. Such a flutter point is defined as the point where a damped oscillation transitions to one growing in amplitude.

The idea that flutter is a transition between damped and growing oscillations is repeatedly used in analysis techniques. It implies that the response at the flutter point is of constant amplitude. This makes the determination of a flutter point often easier than computing the general response of a configuration. Despite this, determining the flutter boundary of an aircraft is a major job. While the point where flutter occurs is far from its normal operating point it can lead to the appearance of difficult features such as strong shock waves and boundary layer separation. Besides these complex aerodynamic phenomena the flutter speed varies also with the aircraft configuration. Therefore it is necessary to consider multiple flutter modes that vary with the fuel amount, payload, and the configuration in case of a military aircraft (e.g. usage of external stores and weapons). The combination of the latter configuration options lead to a large number of scenarios that must be analyzed.

For the overview of the calculation methods, only the case of "Classical Flutter" is considered. Which is associated with potential flow and usually, but not necessarily, involves two or more degrees of freedom. Far more difficult to analyze, on a theoretical basis, is the "nonclassical" type of flutter. This may involve many different aerodynamic phenomena such as separated flow, periodic breakaway and reattachment of the flow, stalling conditions, and various time-lag effects between the aerodynamic forces and motion.[4]

Calculation Methods

To calculate the response of a system, a number of efficient methods are available. Each of these methods avoids the costs of the brute-force approach, where the response needs to be calculated for each velocity and frequency of the applied force. They generate directly an approximated flutter diagram.

Three of these methods are called the k method, the p-k method, and the p method. The first two methods assume that only harmonic aerodynamic data are available. This assumption is sufficient to predict the flutter boundaries. In the k method a fictitious structural damping term is added to the equations of motions to keep the response purely harmonic. When this fictitious damping becomes zero a flutter point is reached. The p-k method compensates for the non-physical behavior in the appearance of more frequencies and damping solutions than the number of degrees of freedom. A structured approach for these two methods is given by Hulshoff[5] where a more detailed description is given by Theodorsen[8] and Hassig[9] about respectively the k method and p-k method.

The p method is more advanced as it can also predict the response away from the flutter boundary. Therefore a larger set of aerodynamic data is required to construct an approximate model that includes growing and decaying motions.[5]

2.1.4 Comparison of Critical Wing Speeds

Based on the discussed phenomena, a conventional wing has three critical speeds. These critical speeds are the flutter speed, the divergence speed, and the aileron reversal speed. For conventional straight swept wings of conventional construction, wing torsional divergence speed is usually higher than the aileron reversal speed. The bending-torsion flutter speed is lower than the aileron reversal speed and therefore the critical speed. A qualitatively relation between critical speeds for a typical wing with varying amount of rearward and forward sweep is shown in Figure 2.4. After a certain amount of sweep back, the aileron reversal speed becomes the limiting factor. For a forward swept wing the divergence speed becomes the critical speed.

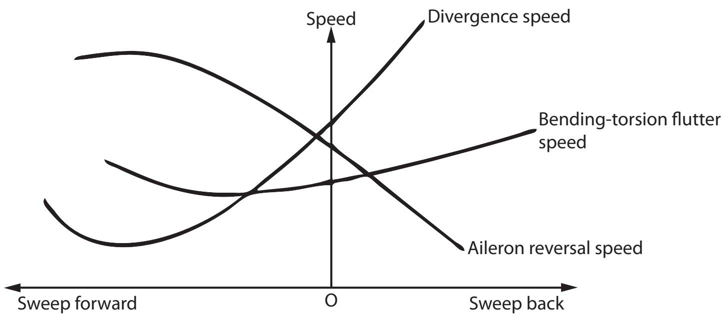

Figure 2.4: Comparison of wing critical speeds[4]

2.1.5 Aerodynamic Twist

A different phenomenon is introduced when the wing is swept backwards. This phenomenon is called aerodynamic twist and is caused by the lift force that is bending the wing upwards. This upward force applies usually near the elastic axis, therefore the points A and B will deflect approximately the same distance, as shown in Figure 2.5. However, in streamwise direction the wing station, section BC, is subjected to a progressive decrease in angle of attack towards the tip. The larger upward deflection of point B is caused by a larger distance to the area A, perpendicular to the elastic axis, than point C. Therefore this decrease in angle of attack causes a relieve in loading of the wing tip and the aerodynamic center shifts more inboard.[4,6]

When the same wing is swept forward, the opposite effect is gained. Point C' is deflected more upwards than point B. This effect causes a progressive increase in angle of attack towards the tip. Due to the increase in angle of attack the wing loading of the wing tip is aggravated and the aerodynamic center shifts outboard. An increase of the loading on the outboard part could be beneficial when aeroelastic control is applied.

2.2 Means of Achieving Variable Wing Geometry

In the past, much research was conducted into adjusting the characteristics of aircraft by changing the configuration of the aircraft in flight. This enables today's aircraft to maximize their performance

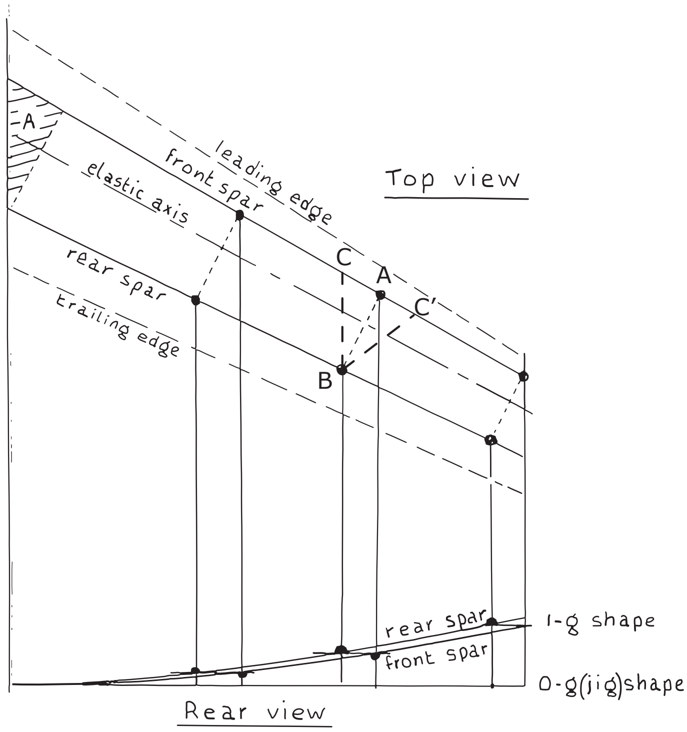

Figure 2.5: Bending of a swept wing due to lift[6]

during flight at radically different flight conditions.[10] These configuration changes can take place in any part of the aircraft, e.g. fuselage, wing, engine, and tail. This chapter however, focuses on the ability of changing the characteristics of the wing.

These concepts that utilize the ability to adjust the wings configuration can be classified based on the method of actuation that is used to change the wing. The two different categories are "discrete translation and rotation" and "morphing". In Figure 2.6 this classification scheme is shown. Each category is described in a separate section. After all the concepts have been treated, a concept is chosen based on their advantages and disadvantages.

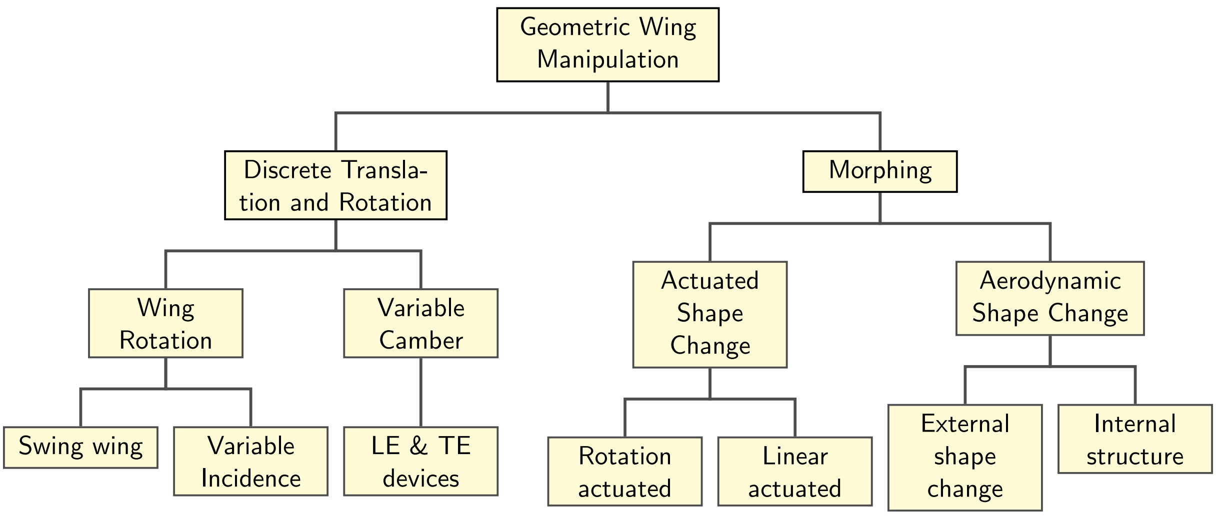

Figure 2.6: Classification of Geometric Manipulation Technologies

2.2.1 Discrete Translation and Rotation

Discrete translation and rotation devices are systems that can be used to change the sweep angle and/or incidence angle of the wing. For example to create a change of the incidence angle, leading and/or trailing edge devices can be deflected. These devices are used to increase the performance of the aircraft during a maneuver. A short overview of the commonly used methods are provided in this section.

Swing Wing

The most popular and successful method, so far, is the variable sweep wing (also known as swing wing) design. By sweeping the wing around a certain point, an aircraft is able to adjust its aerodynamic performance to perform well at both low and high speed regimes. Furthermore, it also helps the aircraft during take-off and landing.

The first aircraft with variable sweep was the Messerschmitt P-1101, developed in 1944. Its sweep angle could be varied from $35°$ until $45°$. Nevertheless, the sweep angle could only be changed while the aircraft was on the ground. Bell Aircraft Company created the first aircraft, the Bell X-5 shown in Figure 2.7b, that was able to achieve an in-flight change of the sweep angle, from $20°$ to $60°$ within twenty seconds. This concept was successfully demonstrated by showing a reduction in wave drag and improvement of the performance near the speed of sound. One of the major challenges faced by the designers was to compensate for the change in aerodynamic center location of the aircraft when the wing is rotated about its pivot.

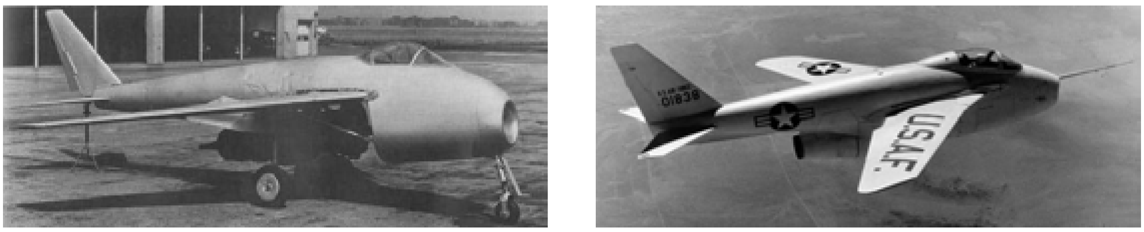

(a) Messerschmitt P-1101 (1944)

(b) Bell X-5 (1951)

Figure 2.7: The first swing wing aircraft

The first production aircraft with swing wing capability was the General Dynamics F-111 "Aardvark" (1964). This aircraft has been developed to create a single aircraft that could fulfill a fleet defense interceptor (navy) and a supersonic strike aircraft requirement (air force). The aircraft could take-off and land in as little as 2000 feet with fully extended wings. With the wings fully swept back it could reach a speed in excess of Mach 2. Despite these benefits, the F-111 exhibited a very high trim drag at supersonic velocities due to inboard mounting of the pivot point. In the design for the F-14 this has been corrected by applying a more outboard pivot location. Other high performance aircraft that posses the swing wing ability are e.g. MiG-23 (1967), and Rockwell B-1B "Lancer" (1974).[10,11]

Variable Incidence Wing

A variable incidence wing has been used to reduce the landing and take-off distances by changing the incidence angle of the wing to increase the lift force. Therefore this concept is different from the variable sweep wing that reduces the wave drag of the wing at higher velocities. The first aircraft that has been equipped with a variable incidence angle was the Republic XF-91 "Thunderceptor"

Figure 2.8: F-111 Aardvark, swing wing aircraft

(1949). It was able to change the incidence angle from $-2°$ to $5.65°$. Where the high incidence angle has been used for take-off and landing, while the low angle-of-attack configuration has been used for high speed flight.

In 1955 another variable incidence wing was built, the Vought F-8U "Crusader" shown in Figure 2.9b. The wing incidence angle could be changed up to $7°$ by rotating the wing about its rear spar. Besides low speed take-off and landing capabilities, the variable wing incidence angle also allows the pilot to have better visibility during landing as the elevated incidence angle allowed the fuselage to be kept parallel to the runway.

(a) Republic XF-91B "Thunderceptor" (b) Vought F-8U "Crusader"

Figure 2.9: The variable incidence aircraft

Variable Camber

A broadly utilized method of camber control on wings is the usage of control surfaces and high lift devices. In these designs discrete and rotating leading and trailing edge controls are mostly used.

High lift devices are used to increase the lift coefficient during low speed flight such as take-off and landing or during maneuvers (fighters). Leading edge devices or slats slightly reduce the lift coefficient at low angles of attack, while they increase the maximum lift coefficient at higher angle of attack, as is illustrated in Figure 2.10. The function of trailing edge devices is to shift the lift curve upwards.

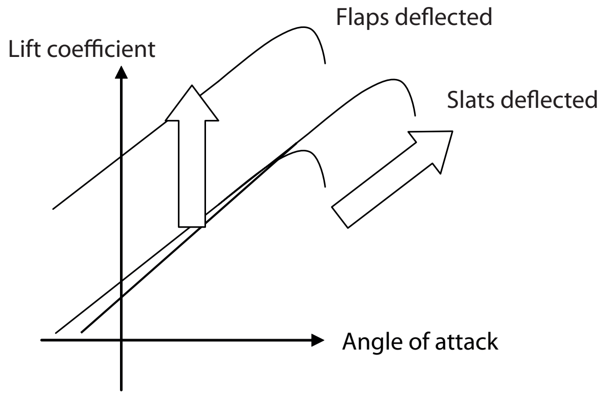

Figure 2.10: Effect of flaps and slats on the lift curve[6]

For primary roll control, wings are equipped with control surfaces called ailerons. By deflecting them asymmetrically a rolling moment is produced. A negative side effect of a downward deflected aileron is that the produced lift is applied behind the elastic axis of the wing, producing a leading edge down torsion moment. This moment twists the wing and produces a decrease in local angle of attack. At high dynamic pressures this structural deformation is enlarged and may lead to aileron reversal, where the resulting change in lift of the outboard wing counteracts the lift due to aileron deflection and causing a rolling motion in the opposite direction.

Especially high aspect ratio swept back wings are more susceptible for aileron reversal as they are more flexible and therefore have larger deformations. Since aft sweep decreases the angle of attack of the outboard sections due to the aerodynamic twist which has been discussed in Section 2.1.5. This effect is increased by a downwards deflection of an aileron which causes the lateral position of the lift force to shift outboard. The combination of the twist down moment and aerodynamic twist lowers the aileron reversal speed even more.

2.2.2 Morphing Wing

Apart from discreet translation and rotation techniques in order to achieve a variable wing geometry, morphing techniques can be applied. A morphing wing has the ability to change its shape by using actuators or aerodynamic loads that deform its shape. In this section some of these morphing concepts are treated.

Actuated Shape Change

In the past, several concepts are built capable of modifying the shape of a wing by the use of actuators. Full morphing concepts, e.g. the Lockheed Martin Z-wing and the NextGen MFX[12], are able to radically change their wing shape. The Z-wing is able to change its surface area significantly by folding its wing towards the fuselage as shown in Figure 2.11a. NextGen Aeronautics created a shape changing UAV design, shown in Figure 2.11b, by changing the sweep angle of the wing. Both linear and rotating actuated shape change examples are discussed in this section.

Linear Actuated – Smooth Camber Conventional variable camber systems produce a discontinuous wing surface which increases the drag of the wing. The Mission Adaptive Wing (MAW), of the Advanced Fighter Technology Integration (AFTI) F-111, consisted of leading and trailing edge variable camber surfaces that could be deflected in flight to provide a near-ideal wing camber shape

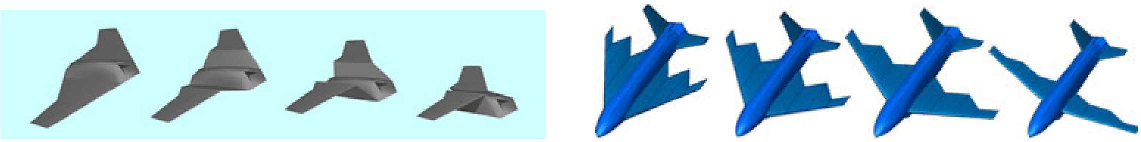

(a) Lockheed Martin Z-Wing (b) NextGen Aeronautics shape-changing UAV

Figure 2.11: Full morphing concepts

for any flight condition. These surfaces featured smooth, flexible upper surfaces and fully enclosed lower surfaces as can be seen in Figure 2.12. Results of the project showed a drag reduction at the design cruise point and also on off-design conditions.[13,14]

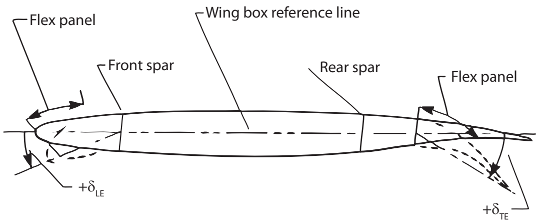

Figure 2.12: The Mission Adaptive Wing smooth variable-camber flap shape[15]

Rotation Actuated – Twist Distribution A different way to adjust the wing lift characteristics is to change the twist distribution along the span. By rotating a rod that is coupled to a particular wing section, a twist angle is introduced at that rib section. In Figure 2.13a an example of such a wing is given were twist can be introduced on three points along the span. A disadvantage of such a system is that it requires a lot of power to induce twist. The aerodynamic loads and stiffness of the wing need to be overcome before wing twist can be induced.[16]

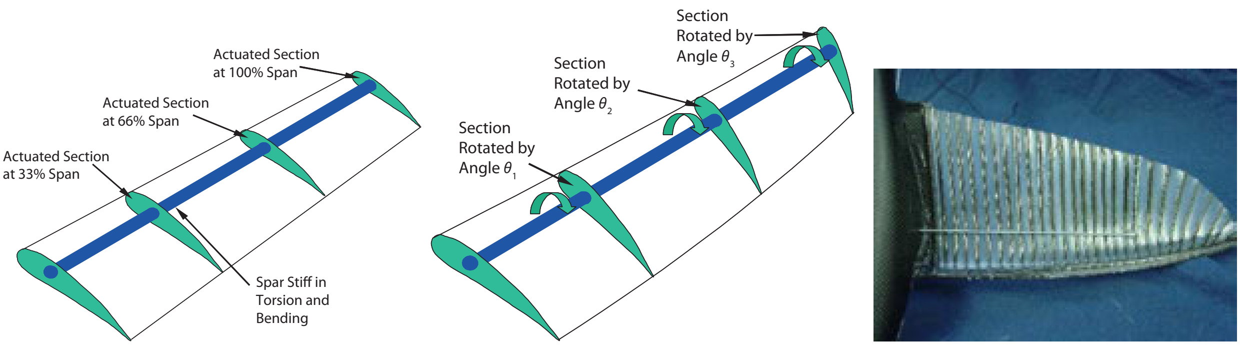

(a) Schematic view of a twisting system[16] (b) Membrane wing[17]

Figure 2.13: Forced twist distribution

A more suitable type of wing for this concept is a membrane wing as it requires a smaller torque to introduce twist on a rib section. Figure 2.13b shows an example of such a system that can rotate a rod to induce twist at a certain wing section. Test results shown a satisfying improvement of the roll rate and lift-to-drag ratio.[17,18]

Aerodynamic Shape Change

A different and more energy efficient approach is to change the shape of a wing by making small adjustments to the wing (e.g. a leading and/or trailing edge deflection or an internal structural change). These small adjustments that change the pressure distribution or structural properties, combined with a relative flexible wing or wing segment results in a deformation of the wing structure that are caused by the aerodynamic loads. By applying these adjustments in a correct way, the desired wing shape can be achieved. A selection of such "active aeroelastic wings" is presented by classifying them into two categories: "External Shape Changes" and "Internal Structure Changes".

External Shape Change One way of using the aerodynamic loads is to introduce twist. This method uses the change in aerodynamic moment that is created by the deflection of leading and trailing edge devices, shown in Figure 2.14, to twist the wing.

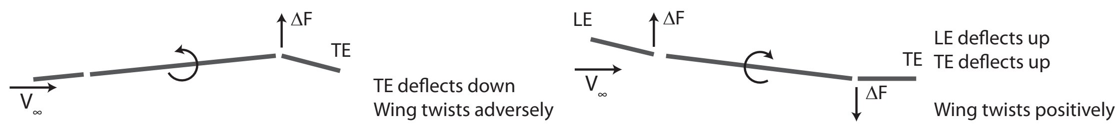

(a) Conventional approach (b) Aeroelastic approach

Figure 2.14: Control methods[19]

In the mid-1980s Rockwell International and NASA initiated the Active Flexible Wing (AFW) program to provide weight saving and improved aerodynamics.[20] This concept does not use the control surfaces as primary control devices but are used as aerodynamic tabs to control the aeroelastic deformations of the wing. Therefore it is the total wing deformations that are used to produce controlling forces. The required deformations of the wing are shown in Figure 2.15.

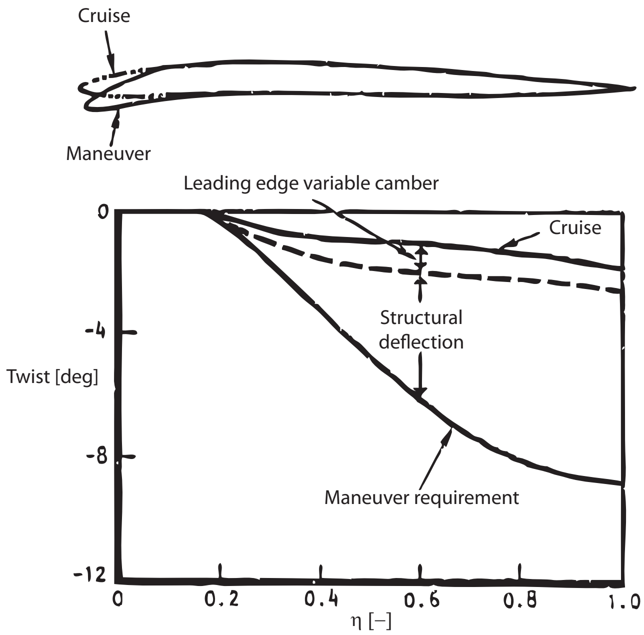

Figure 2.15: AFW aeroelastic tailoring challange[21]

During a study the required deflections were determined. The deflections were based on maintaining a 66 degree per second steady state roll for various dynamic pressures. This resulted in control surface deflection that never exceeds a value of $5°$. Compared with a conventional "stiff" wing design, a typical trailing edge control surface deflections in the range of $30°$ to $40°$ are required to maintain an equal roll rate. As a result of the AFW roll control concept, the drag of the wing during a maneuver is much lower in comparison to a wing with conventional roll control. In addition the smaller control surface deflections result in a reduction of the surface hinge moments, requiring smaller, lighter, and lower power actuators.

This way of control is further researched in a joint flight research program, involving the United States Air Force (USAF), NASA, United States Navy, and industry. It has been initiated in order to demonstrate the Active Aeroelastic Wing (1996) technology in flight experiment hosted by a NASA Dryden owned F/A-18 fighter aircraft, shown in Figure 2.16. This aircraft was an ideal choice for the AAW technology demonstration because of its high-speed flight capability and the thin flexible wings with multiple control surfaces. All these features together produced the aeroelastic characteristics that can be exploited by the application of AAW technology.

Figure 2.16: The X-53 Active Aeroelastic Wing Flight Research aircraft[22]

The AAW program started with a pre-production version of the F/A-18 aircraft that had been used earlier for the high alpha research vehicle. For this program several modifications were made. The wing skin panels were changed to increase aircraft flexibility. A leading edge flap drive system has been added that drove an independent outboard and inboard leading edge flap. Finally, new flight control computer hardware and software were designed and a research instrumentation system has been added to the aircraft to monitor and evaluate the aircraft dynamics and loads.

In Figure 2.17 the non dimensionalized roll rate is plotted versus the Mach number for the control law test flights at $5,000$ ft MSL and $10,000$ ft MSL. According to Chen et al.[23] it is required to have a roll rate of 120 deg/s or more at transonic Mach numbers. As can be seen in this figure, the AAW wing control power alone can compete very favorably with the production stiffened wings on roll response that uses the ailerons and horizontal tail. This AAW roll performance has been achieved by exploiting the wing's aeroelastic twist. When the differential stabilator has been activated during testing, the AAW responses would have been much higher than those using the conventional approach (i.e. stiffened and flexible wing).

Another important feature of the AAW technology is that it has the ability to manage loads while achieving large amounts of control power. This ability was shown during a 5g wind up turn whereby the AAW technology reduced the wing root bending moment by 10%.

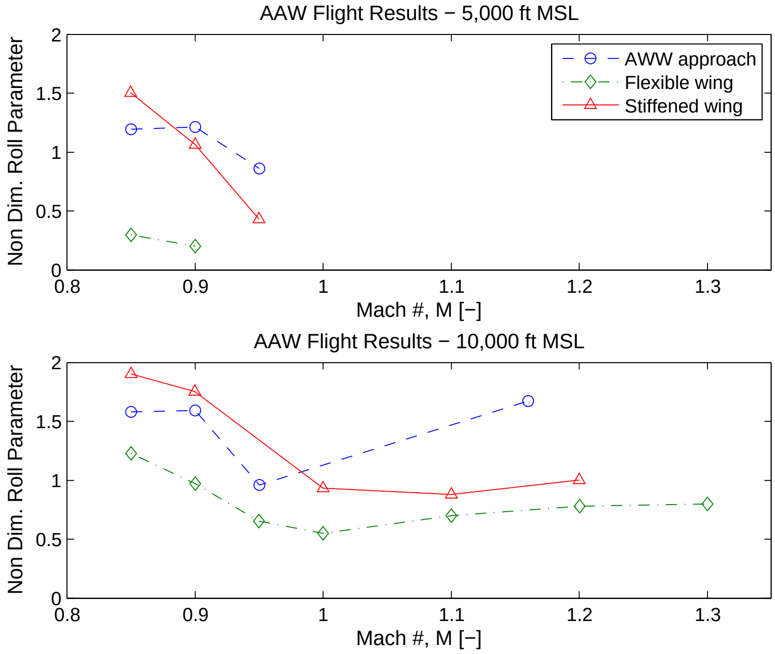

Figure 2.17: Comparison of AAW flights vs. production F/A-18[22]

The flight demonstration program showed that the AAW design approach is ready for the next step: using this process to design new wings that are thinner, lighter and have higher aspect ratio than might have been used for previous conventional applications.[19,22]

Internal Shape Change One of the first projects in the direction of morphing wings was the variable camber wing design created by H.F. Parker of NASA in 1920. His idea was to use a variable airfoil in order to supplement lift generated by the rigid planform (biplane or triplane configuration) for slower speeds. At high speeds the variable planforms are set to carry no loads and are to be in streamline (symmetrical) shape. At low speeds they are to carry their share of the weight and are deeply cambered. This change in airfoil shape is caused by a change in aerodynamic loading of the airfoil. While the other concepts explained in this section rely on an active change of the internal structure to shift the elastic axis.

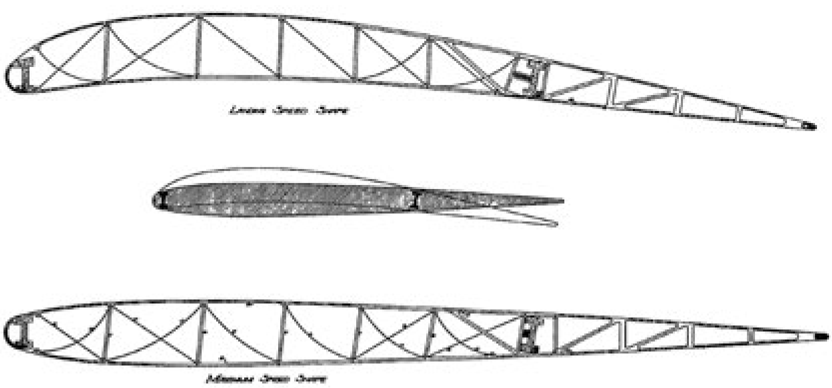

Figure 2.18: Variable camber rib design proposed by Parker in 1920[24]

For these lower speeds the angle of attack must be increased. The stream-line plane is carried through the same angle and has now unbalanced forces acting on it, tending to deform it upward. These forces are the largest near the leading edge, and decrease rapidly as the trailing edge is approached. Figure 2.18 shows the rib design of the variable planform section. A front spar is placed near the leading edge and a second spar is placed at about two-thirds of the chord back from it. The part between the spars is made flexible, so it can deflect upwards, and the rear part is rigid. Furthermore, the ribs must be able to slide over the rear spar. To prevent the camber to increase after its normal, an internal bracing system comes into operation when the maximum deflection is reached.[24]

A more recent project of the European Union is called "Active Aeroelastic Aircraft Structures" (3AS). The University of Manchester participated with two concepts to the project. These concepts are able to change the aerodynamic twist by means of changing the position of a spar or rotating the spars.

The first concept, shown in Figure 2.19, is made of three identical uniform spars, where the outer spars remain at the same position while the middle spar can be moved anywhere within the box. Such a design enables the torsional stiffness and position of the flexural axis to be adjusted, whereas the bending stiffness remains constant.

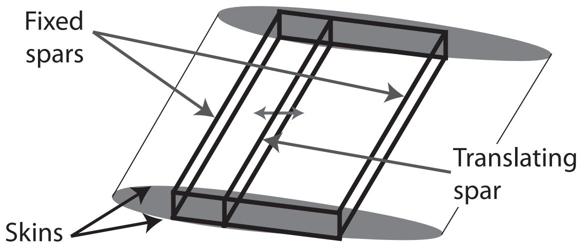

Figure 2.19: Model of a rectangular wing box with a translating middle spar[25]

By moving the spar towards the front, the elastic axis shifts in opposite direction (aft). This causes a change in the length of the moment arm of the lift force around the elastic axis, shown in Figure 2.20. This change in the moments around the elastic axis, changes the amount of twist. Beside the fact that the spar can relatively easy be actuated, it is difficult to transfer the bending moment from an aeroelastic wing section to the stiffer inboard section of the wing.[25,26]

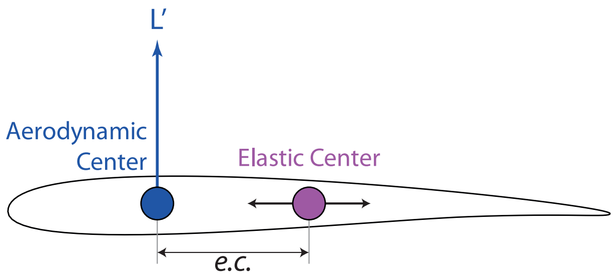

Figure 2.20: Schematic representation of the model

A different way, the second concept, of controlling the amount of twist is done by rotating a front and rear spar, shown in Figure 2.21. Each rotating spar has the ability to rotate $90°$. This rotation range of the spars allows the elastic axis to shift over a relative small distance (between 45% and 55% chord).[25] Furthermore, it is difficult to transfer the bending moments from the aeroelastic section to the inner wing section.

A continuation of the "smart spars" project has been focused on the integration of hinged spars in a high aspect ratio wing. To demonstrate the results, a 1.8 meter span sub-scale UAV with only lateral and directional control has been modified. Modifications were performed on the outer wing

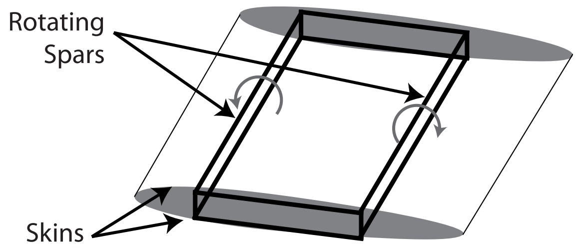

Figure 2.21: Model of a rectangular wing box with rotating spars[25]

section, shown in Figure 2.22. The main spar has been replaced by a spar that could be swept from 4.5° forward to 9.5° aft. With this rotation range of the main spar, the elastic axis can be changed between 30% chord and 70% chord.

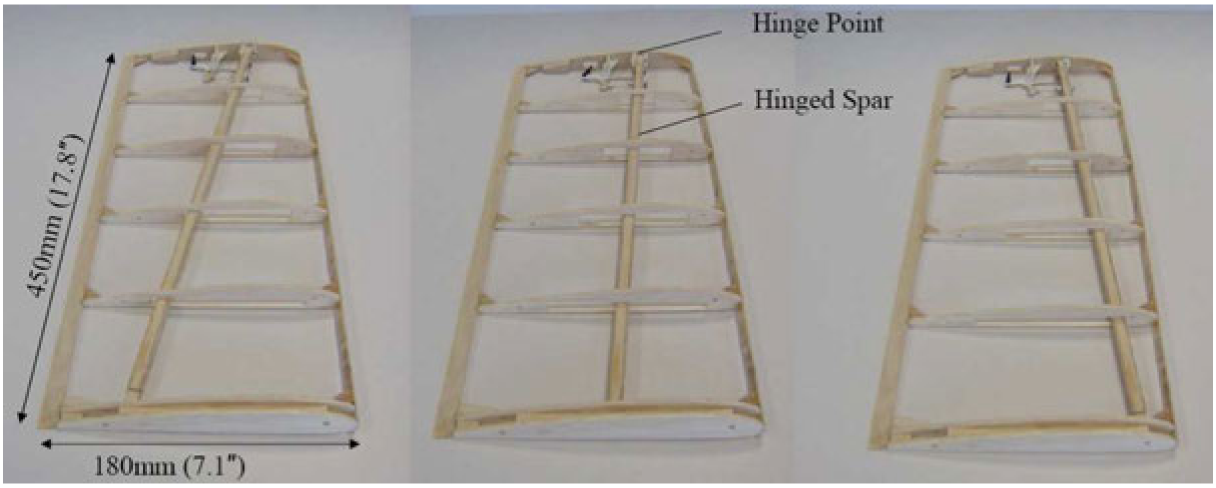

Figure 2.22: Active Aeroelastic Wing panels[3]

During wind tunnel testing of the wing panels at velocity of 10 m/s). It was shown that the peak-to-peak change in twist totaled up to 3.7°, resulting in a change of 35% in the lift coefficient. At higher angles of attack the amount of twist increased to a maximum of 9.1° peak-to-peak. Flight testing proved that a rolling motion could be induced and showed that the system was able to return the UAV back to its normal flight conditions by sweeping the main spar.[3]

2.2.3 Concept Decision

Based on the concepts mentioned in Section 2.2.2 a decision has been made. The concepts treated under "actuated shape change" are not chosen to use because a smooth camber system still uses leading and trailing edges to control the aircraft. A system that is able to adjust the twist distribution along the wingspan is relative heavy. Furthermore, the system needs to be powerful to twist the wing structure and resist the aerodynamic loads. The concepts discussed in "external shape change" are not chosen since they use the leading and trailing edge devices to imply a beneficial twisting moment around the elastic axis. However all these concepts do not use an alternation of the elastic axis position.

The three remaining concepts use different methods to alter the position of the elastic axis. These methods are

- Translating spar
- Rotating spar
- Sweepable spar

With these methods the wing can be split up into different segments where the outer segments are the aeroelastic panels and the inner panels are normal.

The variation of the elastic axis that is created by the rotating spar concept is relative small compared to the other two concepts. Furthermore the bending stiffness is also reduced when the spars are rotated. Based on these reasons the concept has been dropped.

By translating a spar forward and aft the largest alternation of the position of the elastic axis can be obtained. Nevertheless, it is difficult to transfer the bending loads from the outer wing segment to the inboard segment. Since the position of the spar can be changed, there is no fixed point that can be reinforced to handle the load.

This problem is solved by attaching the inboard end of the moveable spar to a fixed hinge point, i.e. sweepable spar. Therefore the bending moment is transferred to the inner through a fixed point. The position of the elastic center at the wing tip changes linearly with the sweep angle of the spar. Although the position of the elastic center varies from the hinge point towards the wing tip, compared to a constant position of the elastic center for the translating spar.

Based on these conclusions the concept of the sweepable spar is chosen. An overview of the advantages and disadvantages is presented in Table 2.1.

Table 2.1: Overview of the advantages and disadvantages

Concept	Advantages	Disadvantages
Translating spars	• Easy to actuate • Large change of the elastic axis	• Bending moment transfer
Rotating spars	• –	• Small change of the elastic axis • Change in bending stiffness
Sweepable spars	• 40% change of the elastic axis • Maximum twist peak to peak change of 9.1°	• –

2.3 Roll Parameters

In order to obtain an estimate of the roll performance of the wing, a number of parameters are required. These parameters are the lateral control effectiveness and roll damping coefficient. The lateral control effectiveness refers to the influence of a deflected roll control device on the rolling moment coefficient. This rolling moment is counteracted by a roll damping moment, which is caused by the upward going wing. This upward motion reduces the effective angle of attack and therefore reducing the rolling moment.

With both parameters known, the roll performance of the wing can be determined by using the roll helix angle $\frac{pb}{2V}$. Finally the helix angle can be used to calculated the steady state roll rate.

2.3.1 Lateral Control Effectiveness

To determine the lateral control effectiveness of a deflected lateral control device, the resulting rolling moment is required. A method to calculate this moment, according to Raymer[27], is given by

$$C_l = \frac{2qC_{L_a}}{qSb}\int_{y_i}^{y_o} c\,(y,\lambda)\,y\,\mathrm{d}y \tag{2.1}$$

$$= \frac{2C_{L_a}}{Sb}\int_{y_i}^{y_o} c\,(y,\lambda)\,y\,\mathrm{d}y \tag{2.2}$$

where C_{L_a} is the lift increment of the aileron.

For straight tapered wings, the local chord length can be determined by

$$c\,(y,\lambda) = c_r\left[1 + 2\left(\frac{\lambda - 1}{b}\right)y\right] \tag{2.3}$$

Combining this definition with the spanwise integral over the aileron area (where y_i is the inboard position of the aileron and y_o the outboard position) of Equation (2.2) leads to

$$\int_{y_i}^{y_o} c\,(y,\lambda)\,y\,\mathrm{d}y = c_r\left[\frac{y^2}{2} + \frac{2}{3}\left(\frac{\lambda - 1}{b}\right)y^3\right]_{y_i}^{y_o} \tag{2.4}$$

To determine the lift coefficient of the deflected aileron, it is assumed that the behavior is similar to a plain flap. In Torenbeek[28] the resulting lift increment coefficient is determined by

$$C_{L_a} = \Delta_a\,c_{l_o} = \eta_\delta\,\alpha_\delta\,c_{l_\alpha}\,\delta_f \tag{2.5}$$

depending on the lift effectiveness factor η_δ, theoretical flap lift factor α_δ, airfoil lift coefficient slope c_{l_α}, and flap deflection angle δ_f.

The theoretical flap lift coefficient can be estimated by using the diagram in Figure 2.23a for a particular flap to chord ratio. However this factor should be corrected to incorporate the condition of the boundary layer and to account for the appearance of a gap. This correction factor η_δ can be determined by using Figure 2.23b.

The expression found for the rolling moment coefficient, Equation (2.1), in combination with the increment of the lift coefficient, Equation (2.5), results in an equation for the rolling moment coefficient due to an aileron deflection.

$$C_l = \frac{2\,\eta_\delta\,\alpha_\delta\,c_{l_\alpha}\,\delta_a}{Sb}c_r\left[\frac{y^2}{2} + \frac{2}{3}\left(\frac{\lambda - 1}{b}\right)y^3\right]_{y_i}^{y_o} \tag{2.6}$$

From this equation the aileron control effectiveness can be determined by

$$C_{l_{\delta_a}} = \frac{2\,\eta_\delta\,\alpha_\delta\,c_{l_\alpha}}{Sb}c_r\left[\frac{y^2}{2} + \frac{2}{3}\left(\frac{\lambda - 1}{b}\right)y^3\right]_{y_i}^{y_o} \tag{2.7}$$

where

$$\delta_a = \frac{\delta_{a,\text{left}} - \delta_{a,\text{right}}}{2} \tag{2.8}$$

Note that the aeroelastic effects and influence of the Mach number are not incorporated.

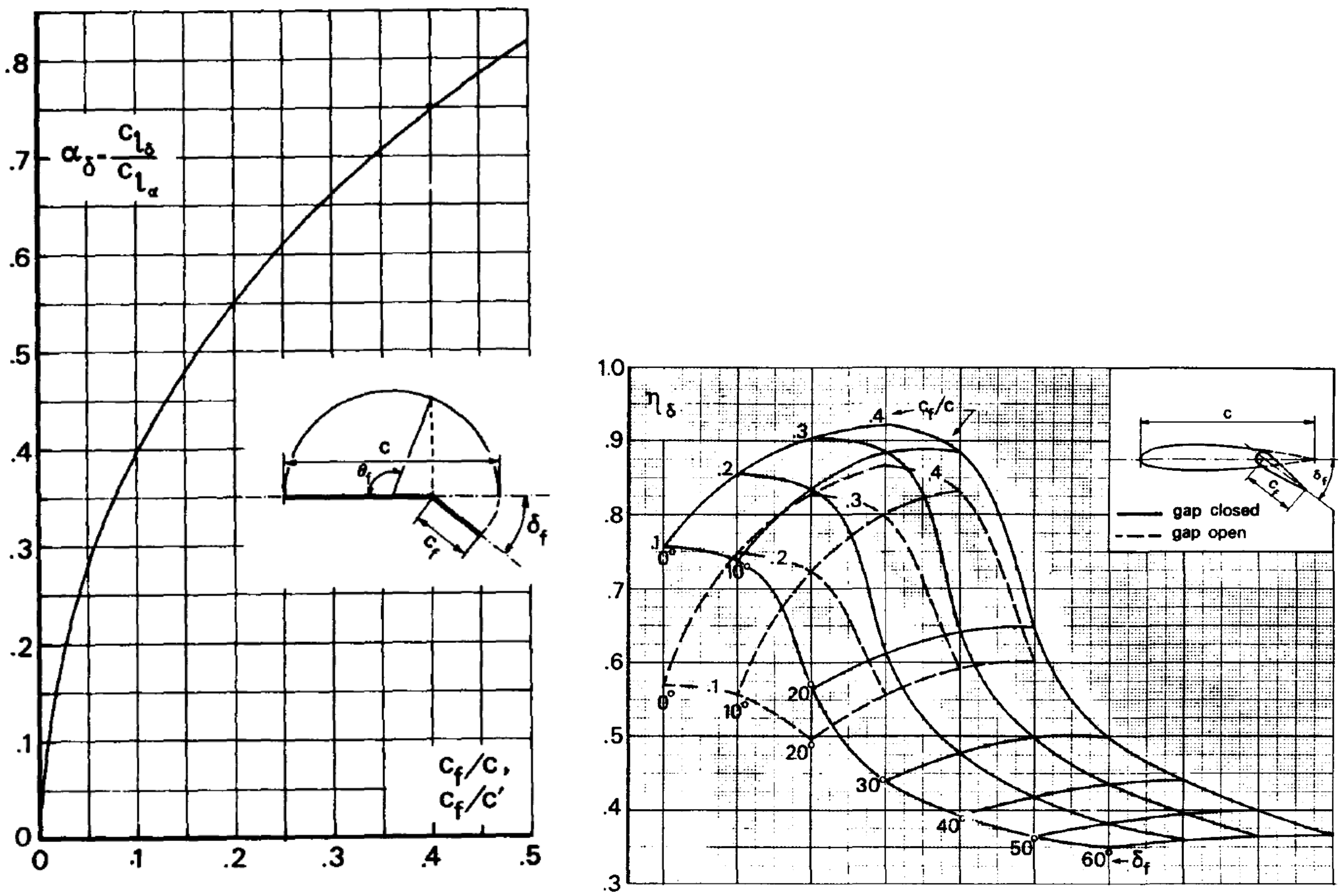

(a) Theoretical flap lift factor[28]

(b) Lift effectiveness factor for plain flaps (derived from experimental data)[28]

Figure 2.23: Plain flaps characteristics

2.3.2 Roll Damping

When a rolling motion is initiated, an opposing moment is introduced that tries to slow this motion. The main contribution to this roll damping C_{lp} is generated by the wing. However, the contribution of the horizontal and vertical tail cannot be neglected; except for the fuselage contribution which is normally neglected.

For this case only the contribution of the wing to the roll damping is considered. The reducing effect of the rolling motion on the angle of attack is shown in Figure 2.24. According to Barlow et al.[29], the damping moment can be written as

$$DM = \frac{pb}{2V}\frac{\rho}{2}SV^2 b\frac{C_l}{pb/2V} \tag{2.9}$$

$$= \frac{\rho}{2}SV\frac{b^2}{2}\frac{\mathrm{d}C_l}{\mathrm{d}\,(pb/2V)} \tag{2.10}$$

Where $\frac{\mathrm{d}C_l}{\mathrm{d}(pb/2V)}$ is called the damping-in-roll coefficient, often written as C_{lp}. This coefficient is a function of the wing taper and aspect ratio.

A simple method to calculate the roll damping of the wing, Equation (2.11), is derived by Polhamus[31]. This is a modified version of the lifting-line equation for the damping in roll[32] to incorporate the

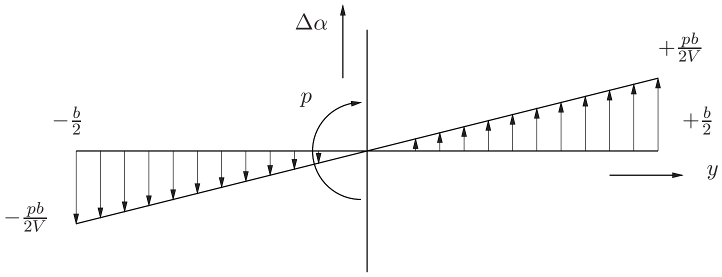

(a) Variation in geometric angle of attack

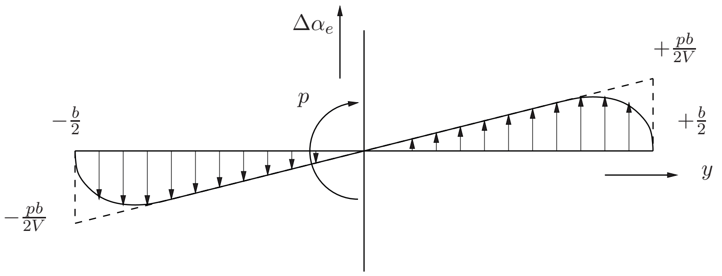

(b) Variation in effective angle of attack

Figure 2.24: The variation of the local geometric and effective angle of attack along the span of a rolling wing[30]

effects of sweep back and taper. By comparing the results from a number of low speed wind tunnel experiments with the new method, it was shown that there was an overestimation of the damping-in-roll coefficient. Therefore Polhamus suggested that Equation (2.11) should be multiplied with a correction factor of 0.94.

$$C_{lp} = -\frac{1}{2}\frac{a_o Æ\left(\frac{y_{L'_p}}{b/2}\right)^2}{2\cos\left(\Lambda_{c/4}\right)\sqrt{\frac{Æ^2}{4\cos^4\left(\Lambda_{c/4}\right)}+4}+\frac{2a_o}{\pi}} \tag{2.11}$$

2.3.3 Steady State Roll Performance

With the expressions for the rolling moment and damping of the roll motion found, the resultant roll performance caused by the use of lateral control device (e.g. aileron deflection) can be calculated. By determining the equation of motion around the longitudinal axis of the aircraft, the roll performance can be found. In Equation (2.12)[33] the equation of motion is given, assuming only a pure rolling motion. To determine the roll characteristics with this equation, the rolling moment coefficient and roll damping coefficient are required. These coefficients are determined in Section 2.3.1 and 2.3.2.

$$I_{xx}\dot{p} = \frac{1}{2}\rho V^2 Sb\left(C_l + C_{lp}\frac{pb}{2V}\right) \tag{2.12}$$

At some point, the motion has become continuous, resulting in a steady state motion (i.e. $\dot{p} = 0$). This reduces Equation (2.12) to the following expression

$$0 = C_l + C_{lp}\frac{pb}{2V} \tag{2.13}$$

By rearranging the parameters of Equation (2.13) an expression is found for the roll helix angle

$$\frac{pb}{2V} = -\frac{C_l}{C_{lp}} \tag{2.14}$$

Based on the rolling moment coefficient and the roll damping coefficient, the roll helix angle can be determined with Equation (2.14). The roll rate can be determined by rewriting Equation (2.14):

$$p = -\frac{2V}{b}\frac{C_l}{C_{lp}} \tag{2.15}$$

Ultimately, the roll rate can be determined by using Equation (2.15) in combination with velocity, wingspan, rolling moment coefficient, and roll damping coefficient.

Chapter 3

Experimental Setup

To determine the performance of the active aeroelastic wing, a test article is manufactured to carry out wind tunnel tests. This chapter describes the building of the test article, the setup of the bench tests to find the actual stiffness parameters of the test article. Finally, the wind tunnel test setup is described.

3.1 Test Article

To check if the predicted behavior of the simulation tool corresponds with the wind tunnel test data, a half wing span model has been built. Before building has been initiated, a three dimensional model has been created to serve as a construction plan.

The dimensions for the test article are based on the wing of the Global Hawk. For the wing span of the model is chosen for 3.0 m, so that the semi span model (i.e. 1.5 m) is well under the maximum of 0.8 for the span to tunnel width ratio. With the span determined, the length of the root and tip chord can be calculated. This resulted in a root chord of 210 mm and 65 mm for the tip chord. In order to create more space for the sweepable spar, the length of the tip chord has been increased to 125 mm. Consequently the aspect ratio of the test article is decreased to about 18 instead of the 25 for the Global Hawk[34].

In order to allow the wing to create a rolling moment, the outer section differs from the inner wing section. The outer section therefore has a rotational main spar that can be moved forward and aft. Besides that the outer segment also has an alternative skin cover to reduce the torsional stiffness. In Figure 3.1 several important dimensions are shown, such as root and tip chord, hinge position and semi span. A complete overview of the dimensions is shown in Table 3.1.

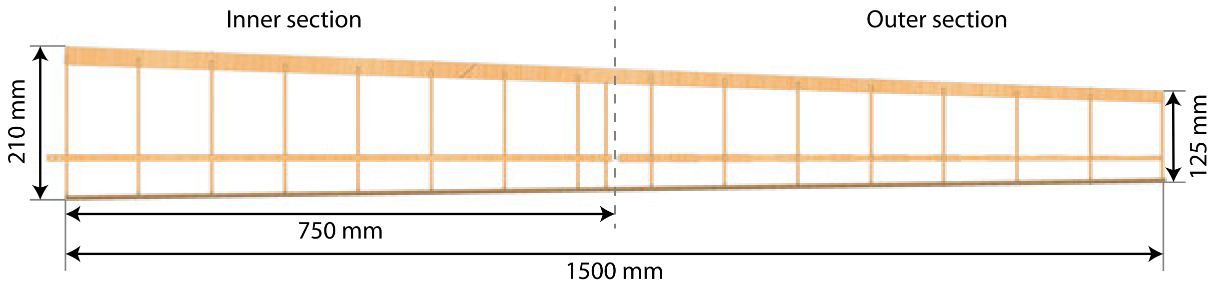

Figure 3.1: SolidWorks model with annotated dimensions (top view)

For the wind tunnel tests, a coupling mechanism has been designed. This mechanism couples the test article with the balance system. Furthermore it provides the ability to change the angle of attack and sweep angle of the wing. The resulting mechanism is described in Section 3.3.1.

Table 3.1: Wing Characteristics

Property	Value	Property	Value
Semi span	1500 mm	Wing area	0.251 m^2
Aeroelastic segment	750 mm	Aspect ratio	17.91
Root chord	210 mm	Airfoil	Clark Y
Tip chord	125 mm	Taper ratio	0.595

Internal Structure

The final shape of the wing is determined by its internal structure. In Figure 3.2 the internal structure is shown with all the components annotated. The most important structural parts, to allow deformations under aerodynamic loads, are the sweepable spar construction and the leading edge cover (not shown in Figure 3.2) of the outer wing segment.

The main function of the main spar is to carry the bending loads created by the lift force of the wing. This is done by placing two balsa wooden beams (5×10 mm) on the bottom and top at 28% chord of each rib along the inner wing segment. On the outer wing segment, a single beam is placed. Both beams are coupled together by an aluminum hinge, so that the outer beam is able to rotate and change the position of the elastic axis of the wing segment.

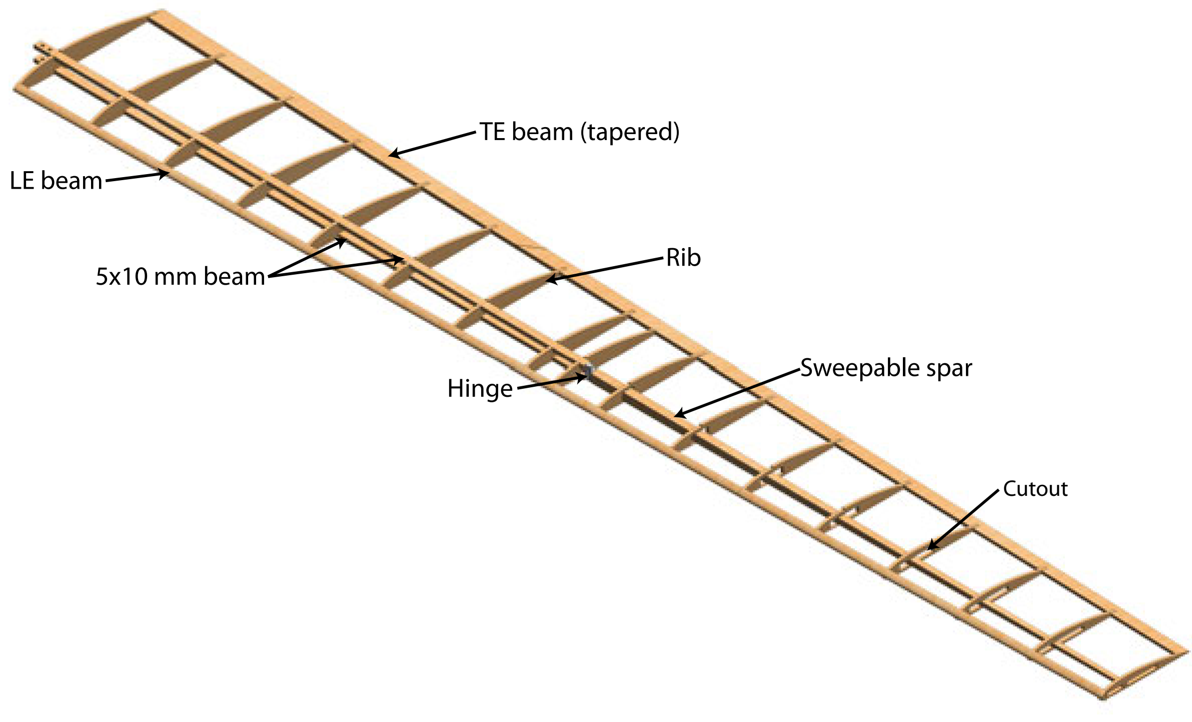

Figure 3.2: SolidWorks model with annotated items (isometric view)

For the shape of the airfoils the Clark Y airfoil is chosen. This airfoil has a flat bottom part which makes manufacturing easier. These ribs have been created of 4 mm thick balsa wood and are placed with an interspacing of 96 mm to resist shear and torsional loads. Just inboard of the hinge point, an additional rib has been placed to act as the transition point of the two different skin cover materials. Furthermore, rectangular cutouts have been made to allow the sweeping motion of the main spar. These cutouts are also shown in Figure 3.2.

Sweepable Spar The rotational spar has the ability to move 22 mm $(1.68°)$ forward and 42 mm $(3.21°)$ aft. To carry the bending loads from the outer wing to the inner wing, an aluminum hinge, shown in Figure 3.3, is used. For achieving the rotational range, the spar has been tapered in two directions. When the thickness reduction would not have been applied, the spar would be too high and too wide for the rib cutouts since the section thickness decreases with increasing spanwise position. However the application of taper reduced the stiffness of the tapered spar significantly. therefore it has been laminated with a carbon sleeve to increase its stiffness.

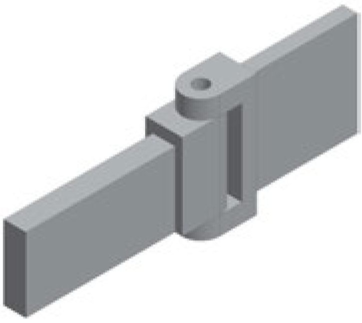

Figure 3.3: Aluminum hinge (isometric view)

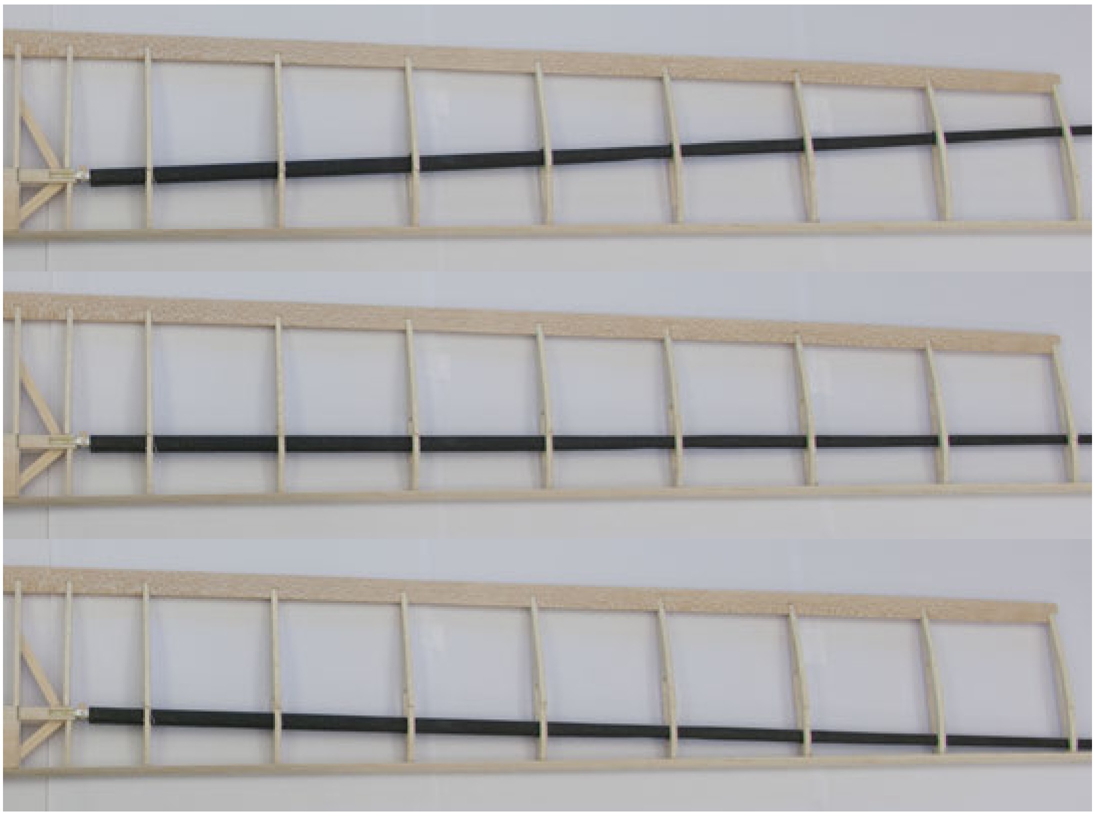

Figure 3.4: Spar positions: most aft position (top); zero angle position (center); most forward position (bottom)

In Figure 3.4 the aeroelastic part is shown with the main spar placed at different locations. To secure the position of the main spar, two MDF beams are placed at the tip of the wing. In these beams five holes have been made, shown in Figure 3.5, to lock the main spar in a certain position with a metal pin.

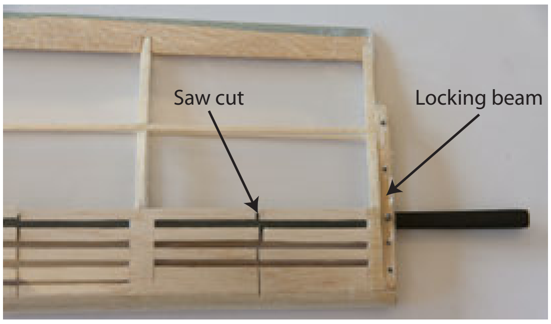

Figure 3.5: Close up of the spar fixation mechanism and leading edge cover panel

Leading Edge Cover The purpose of the leading edge cover is to preserve the curvature on the front part of the airfoil. For the cover, 1.5 mm thick balsa wood panels have been bonded to the rib. These panels cover about the first 30% of the airfoil on the bottom and top side of the wing. On the inner section the cover panel is also bonded to the main spar.

By applying the same cover panels to the aeroelastic wing part, the torsional stiffness would be too high. It would require larger forces to create equal deformations, diminishing the effect gained by the sweepable spar. To compensate for this high stiffness, several rectangular cutouts (3×9 mm and 5 mm apart) have been made in the cover between two ribs.

During the first wind tunnel tests it appeared that the torsional stiffness increased to much as the main spar approached the leading edge. This resulted in an increase of the twist angle instead of a further decrease of the twist angle. As a consequence the rolling moment also increased again as the main spar is swept forward reducing the maximum achievable rolling moment. In order to solve this problem, the first 30% chord of the aeroelastic section has been made more flexible, by making a saw cut between two ribs in the cover panel as can be seen in Figure 3.5.

Skin Cover

With the internal frame finished, the skin cover has been applied on to the wing. The main part is covered with a heat shrink plastic film that has an adhesive side, so the film can be glued to the wing frame. With the plastic film glued to the frame, it can be shrink fitted around the wing. As a result of the shrinking, the stiffness of the wing is increased significantly.

When the shrink film would have been used for the aeroelastic part, the stiffness would be too high to allow for torsional deformations under aerodynamic loads. This would require a larger lift force to produce the same deformations. In order to prevent that, a different material has been used for this part of the wing. A so called cling film or plastic wrap has been used. This is a low density polyethylene (LDPE) film that is normally used to preserve food. Such film is flexible and elastic under small deformations. Other materials that could be used are latex or vacuum bags (used to create composites). Nevertheless, those materials are harder to obtain compared to cling film. The final result is shown in Figure 3.6.

3.2 Bench Test Setup

To be able to compare the simulation model with the wind tunnel tests, the actual stiffness of the test article has been determined. These tests have been carried out to determine an equivalent Young's and shear modulus (E and G respectively) of the inboard and aeroelastic outboard structure of the wing.

Figure 3.6: Complete wing with wing cover

3.2.1 Varying Rigidity

A better distribution of the rigidity can be obtained by varying the second moment of area I and the torsion constant J along the span. When these distributions are known, the Young's and shear modulus of both wing parts can be determined. To obtain a more realistic distribution of both rigidities, the wing is represented as a conical cylinder, shown in Figure 3.7.

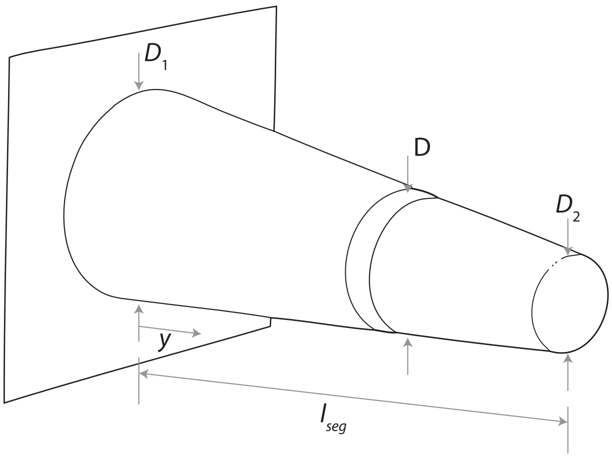

Figure 3.7: Conical cylinder[35]

The diameter D_1 is determined by calculating the area of the Clark Y airfoil at the wing root. The same thing has been carried out for the wing tip, resulting in diameter D_2. So the diameter variation with the spanwise position becomes

$$D(y) = D_1 - (D_1 - D_2)\frac{y}{l_{\text{seg}}} \tag{3.1}$$

$$= D_1(1 - \alpha\, y) \tag{3.2}$$

where

$$\alpha = \frac{(D_1 - D_2)}{D_1 \cdot l_{\text{seg}}} \tag{3.3}$$

With this distribution of the diameter, the variation of the second moment of area is described as

$$I(y) = \frac{\pi D(y)^4}{64} = \frac{\pi D_1^4}{64}(1 - \alpha\, y)^4 \tag{3.4}$$

And the distribution of the torsion constant is given by

$$J(y) = \frac{\pi D(y)^4}{32} = \frac{\pi D_1^4}{32}(1 - \alpha\, y)^4 \tag{3.5}$$

3.2.2 Torsion Tests

To determine shear modulus G of the wing segments a torque has been applied at the end of each segment. To fixate a segments root, the wing has been clamped-in just outboard of the wing root to test the inboard part. For the outboard part, the wing has been built-in just inboard of the hinge point. Therefore the beam lengths of both sections are not the same. The torsion test setup, for the outboard part, is shown in Figure 3.9. A schematic representation of the test setup is given in Figure 3.8.

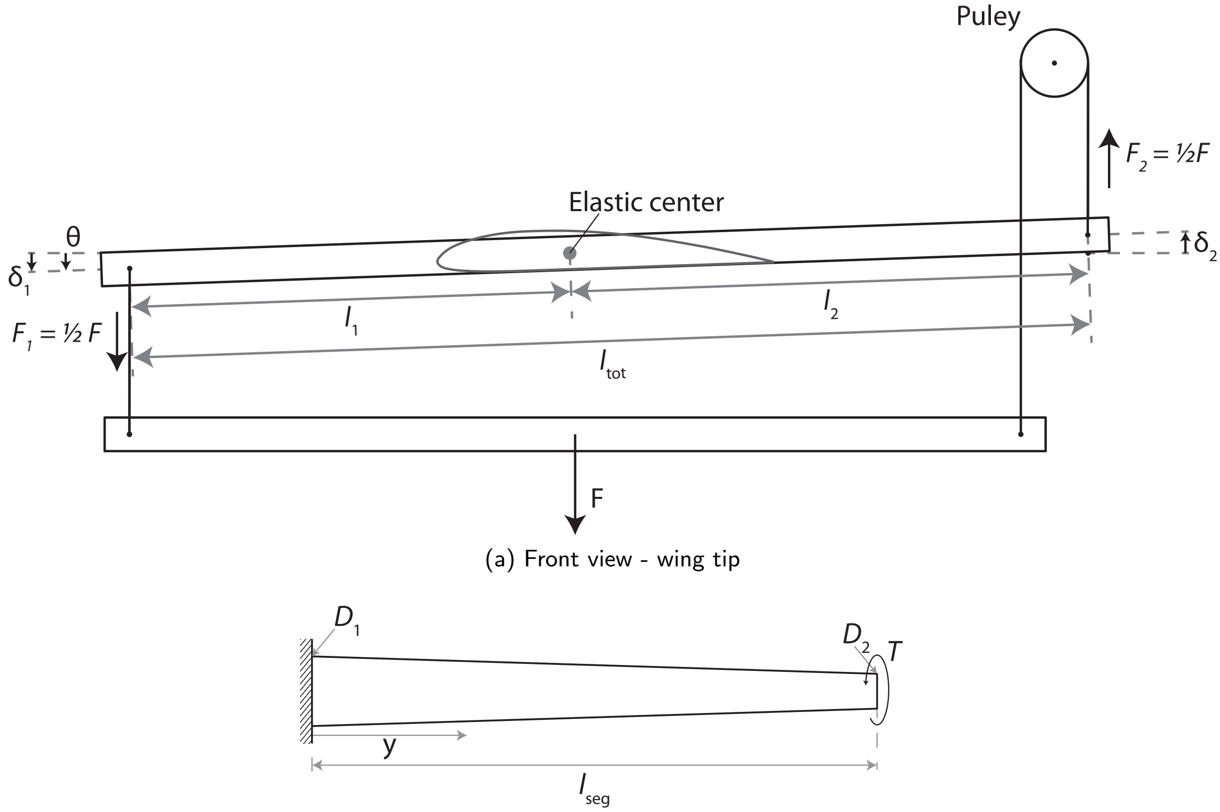

Figure 3.8: Schematic representation of the static test setup for torsion

With the used construction, the attached mass pulls the leading edge downwards and the trailing edge upwards. Hereby a pure torsion motion is applied onto the wing. The resulting displacements (δ_1 and δ_2) are measured using two rulers with a resolution of 0.5 mm. With these measured displacement the measured displacements the twist angle θ is calculated as follows

$$\theta = \arcsin\left(\frac{\delta_1 + \delta_2}{l_{\text{tot}}}\right) \tag{3.6}$$

The torque, positive in counterclockwise direction, that has been applied can be calculated by

$$T = F_1 \cdot l_1 + F_2 \cdot l_2 \tag{3.7}$$

where l is the distance between the force application point and the elastic center of the wing tip. Since the forces applied on both points are the same, the applied torque can be expressed as

$$T = \frac{1}{2} F \, l_{\text{tot}} \tag{3.8}$$

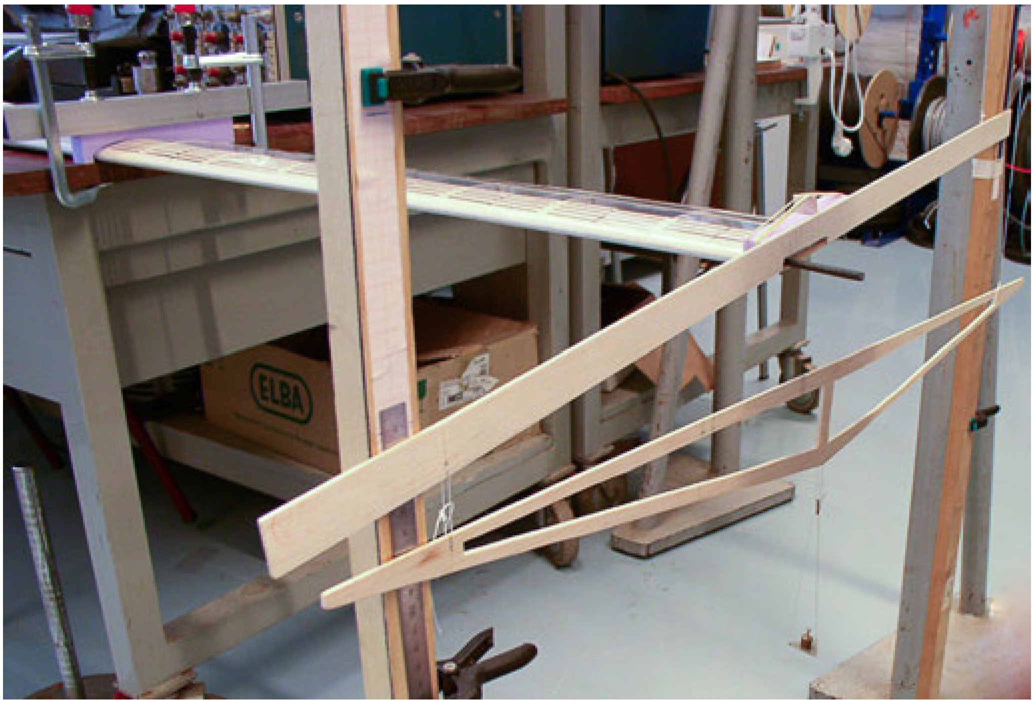

Figure 3.9: Photograph of the static torsion test setup for outboard wing segment

In Table 3.2 the used forces are listed.

With all the components known, the shear modulus G of a conical cylinder[35] is determined by

$$G = \frac{T}{3\,\alpha\,\theta\,J_1}\left[\frac{D_1}{D_2} - 1\right] \tag{3.9}$$

where

$$J_1 = \frac{\pi D_1^4}{32} \tag{3.10}$$

$$\alpha = \frac{D_1 - D_2}{D_1 \cdot l_{\text{seg}}} \tag{3.11}$$

D_1 and D_2 are the equivalent diameters of the wing segment at the built-in end and segment end respectively.

Table 3.2: Torsion test characteristics

		Inboard part		**Outboard part**	
Beam length	l_{seg}	725	mm	765	mm
Arm length	l_{tot}	800	mm	805	mm
Applied forces	F	0.284	N	0.113	N
		0.481	N	0.132	N
		0.775	N	0.162	N
		1.020	N	0.181	N
		1.265	N	0.211	N
		1.511	N	0.260	N
				0.309	N
				0.358	N

3.2.3 Bending Tests

To determine the Young's modulus E of both sections, a mass has been attached on the elastic center at the end of a segment. The resulting end deflection δ, for each applied force F, has been measured with a ruler with a resolution of 0.5 mm. In Table 3.3 the applied forces are listed that have been used for the bending tests.

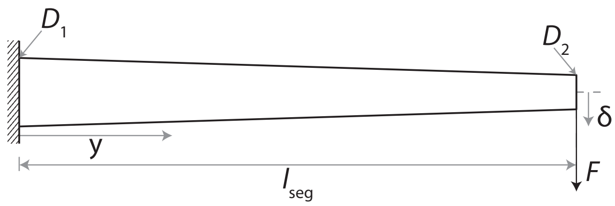

Figure 3.10: Schematic representation of the static test setup for bending

Table 3.3: Bending test characteristics

		Inboard segment		Outboard segment	
Beam length	l_{seg}	725	mm	765	mm
Applied forces	F	0.498	N	0.188	N
		0.989	N	0.385	N
		1.479	N	0.679	N
		1.970	N	0.924	N
		2.460	N	1.169	N
		2.951	N	1.415	N
		3.441	N		
		4.422	N		
		5.403	N		
		7.365	N		

To determine the Young's modulus of a conical cylinder, for a given force and end deflection, the moment-curvature equation can be expressed as follows

$$\frac{\mathrm{d}^2\delta}{\mathrm{d}y^2} = \frac{-F}{EI_1}\left(l_{\text{seg}} - y\right)\left(1 - \alpha y\right)^{-4} \tag{3.12}$$

By integrating Equation (3.12) twice, an expression is obtained for the deflection of the beam. The following boundary conditions are applied during the integration

$$\delta\left(y = 0\right) = 0 \tag{3.13}$$

$$\left.\frac{\mathrm{d}\delta}{\mathrm{d}y}\right|_{y=0} = 0 \tag{3.14}$$

stating zero deflection and slope at the built-in end of the beam. This resulted in the following expression for the end deflection of the conical cylinder

$$\delta\left(y = l_{\text{seg}}\right) = \frac{-Fl_{\text{seg}}^3}{3EI_1}\left[\frac{D_1}{D_2}\right] \tag{3.15}$$

where

$$I_1 = \frac{\pi D_1^4}{64} \tag{3.16}$$

By rewriting Equation (3.15) an expression is found to determine the Young's modulus. This results in

$$E = \frac{-F l_{\text{seg}}^3}{3 I_1 \cdot \delta \left(y = l_{\text{seg}} \right)} \left[\frac{D_1}{D_2} \right] \tag{3.17}$$

3.3 Wind Tunnel Test Setup

To test the semi-span wing model, the Open Jet Facility (OJF) of the Aerodynamics and Wind Energy department has been used. This wind tunnel has an open test section and therefore the test section is more flexible to install external measurement equipment.

In Figure 3.11 a schematic representation of the circuit is given. A set of five dense wire meshes are placed in the settling chamber to reduce velocity deviations and turbulence in the flow. Via a contraction, a smooth flow is blown into the open test section. After the test section, a radiator system is placed to extract the added heat in the flow to control the properties of the flow.

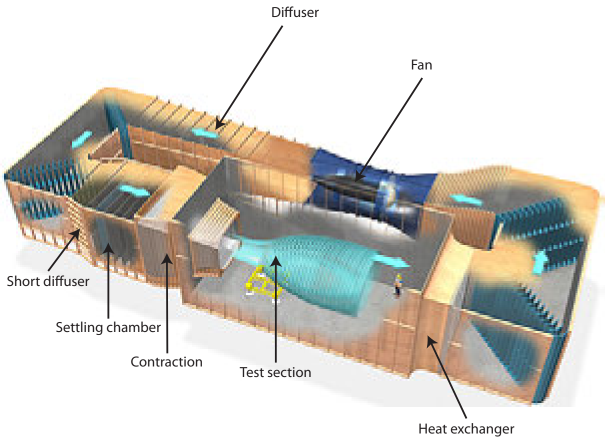

Figure 3.11: Drawing of the OJF circuit

- Maximum test section flow: 30 m/s
- Octagonal jet with a width and height of 2.85 m (equivalent diameter of 3.1 m)
- Velocity deviations smaller than 0.5%
- Longitudinal turbulence intensity is better than 0.24%

3.3.1 Measurement System

To measure the forces, moments and displacements of the designed semi span wing model several tools have been used. These tools consist of an external balance system to measure the resulting forces and moments, laser displacement sensors to determine the displacement of the leading and trailing edge at the wing tip. Furthermore, two mounts have been used to set the angle of attack and sweep angle of the wing.

In Figure 3.12a the angle of attack turntable is shown. This turntable is mounted on the model plate of the balance system. With this mount the angle of attack can be specified with a resolution of $0.5°$. For the wind tunnel test the zero angle of attack of the test article has been defined as the flat bottom side parallel to the wind stream, as can be seen in Figure 3.12b.

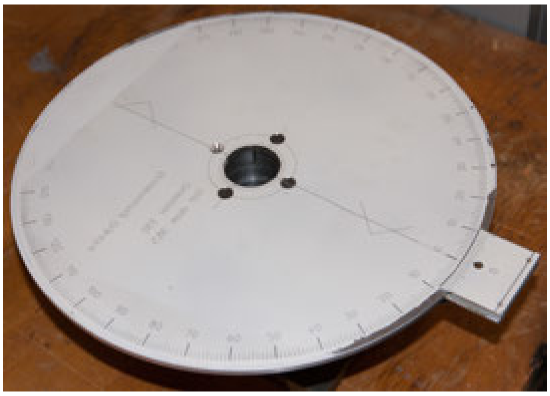

(a) Angle of attack mount

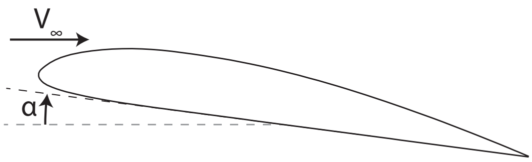

(b) Angle of attack definition

Figure 3.12: Angle of attack setup

To determine the influence of the sweep angle of the wing a new mount has been designed that fitted into the angle of attack turntable. This mount consists of two parts that are bolted together, shown in Figure 3.13a. The bottom part of the mount fits into the turntable and top part has been placed between the two spars of the wing. With this setup the sweep angle, at 28% chord, of the wing can be defined. To determine the sweep angle of the test article a digital angle measuring tool, shown in Figure 3.13b, has been used. Although the angle measurement tool has an accuracy of $0.1°$, this accuracy could not be achieved as both parts where tightened together. Therefore the accuracy of the sweep angle has become $0.5°$.

(a) Wing sweep mount

(b) Digital angle measuring tool

Figure 3.13: Wing sweep angle setup tools

The balance system that has been used is created by the NLR[36]. It can measure the forces in three directions together with the moments around those axes. The axis system that is used by the external balance is presented in Figure 3.14. To reduce the influence of the balance system on the air stream, a table has been placed over it. Another function of this table is that it functions as a reflection plane for the model.

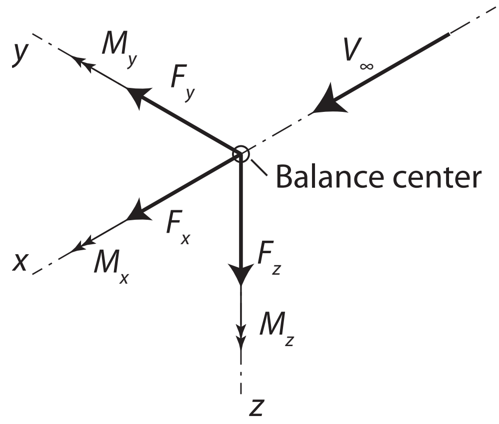

Figure 3.14: Definitions of the OJF axis system, forces, and moments

As a consequence of the installed mounts, the position of the wing root moves in two directions when the sweep angle is adjusted. For the x-direction the displacement can be calculated with the following equation

$$x_{\text{offset}}\left(\Lambda_{0.28c}\right) = \left[42.5 \cdot \sin\left(\Lambda_{0.28c}\right)\right] \cdot 10^{-3} \tag{3.18}$$

The vertical displacement, z-direction, is calculated as follows

$$z_{\text{offset}}\left(\Lambda_{0.28c}\right) = \left[168.5 + 42.5 \cdot \cos\left(\Lambda_{0.28c}\right)\right] \cdot 10^{-3} \tag{3.19}$$

To correct the measured moments for the induced offset, the following correction are applied

$$M_{x,\text{corrected}} = M_{x,\text{measured}} - F_y \cdot z_{\text{offset}}\left(\Lambda_{0.28c}\right) - F_z \cdot x_{\text{offset}}\left(\Lambda_{0.28c}\right) \tag{3.20}$$
$$M_{y,\text{corrected}} = M_{y,\text{measured}} - F_x \cdot z_{\text{offset}}\left(\Lambda_{0.28c}\right) - F_z \cdot x_{\text{offset}}\left(\Lambda_{0.28c}\right) \tag{3.21}$$
$$M_{z,\text{corrected}} = M_{z,\text{measured}} - F_y \cdot x_{\text{offset}}\left(\Lambda_{0.28c}\right) \tag{3.22}$$

For the measurement of the displacement at wing tip, two Keyence laser heads (LK-G402)[37], shown in Figure 3.15 have been used. These laser heads are connected to the controller (KG-G3001V), which is able to determine the distance with an accuracy of 2 μm. Furthermore the controller is capable of recording the measured distances for a certain time frame.

Figure 3.15: Keyence laser head[37]

By installing the laser heads on a beam quick repositioning is possible, when the angle of attack or sweep angle has been adjusted. The position of the laser attachment beam, with respect to the distance between the wing and laser heads, can also be adjusted. To be able to measure the displacements, the distance between the wing and laser heads needed to be larger than 300 mm and smaller than 500 mm. By pointing the lasers on the flat bottom surface to measure the displacements, the influence of the curvature is less compared to when the curved top side is used.

In Figure 3.16 the complete setup in the open test section is shown. A schematic top and side view of the setup are presented in Figures 3.17 and 3.18.

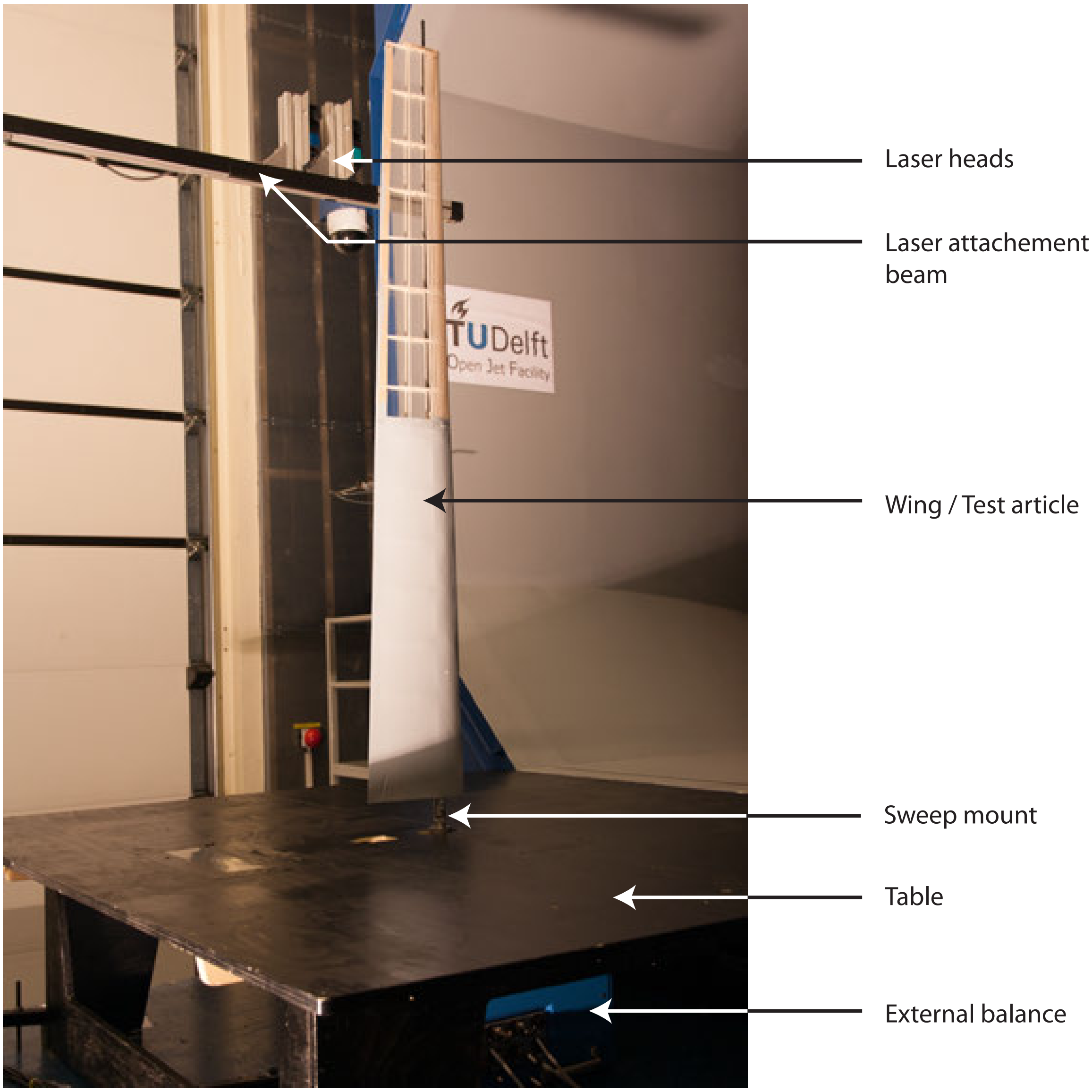

Figure 3.16: Photo of the wind tunnel setup

Overview of the equipment that has been used of the wind tunnel tests:

- NLR external six component balance[36]
- Keyence lasers head – LK-G402 – Measurement range 400 ± 100 mm[37]
- Keyence laser controller – LK-G3001V – Capable to control two laser heads[37]
- National Instruments data acquisition system for balance system and laser controller

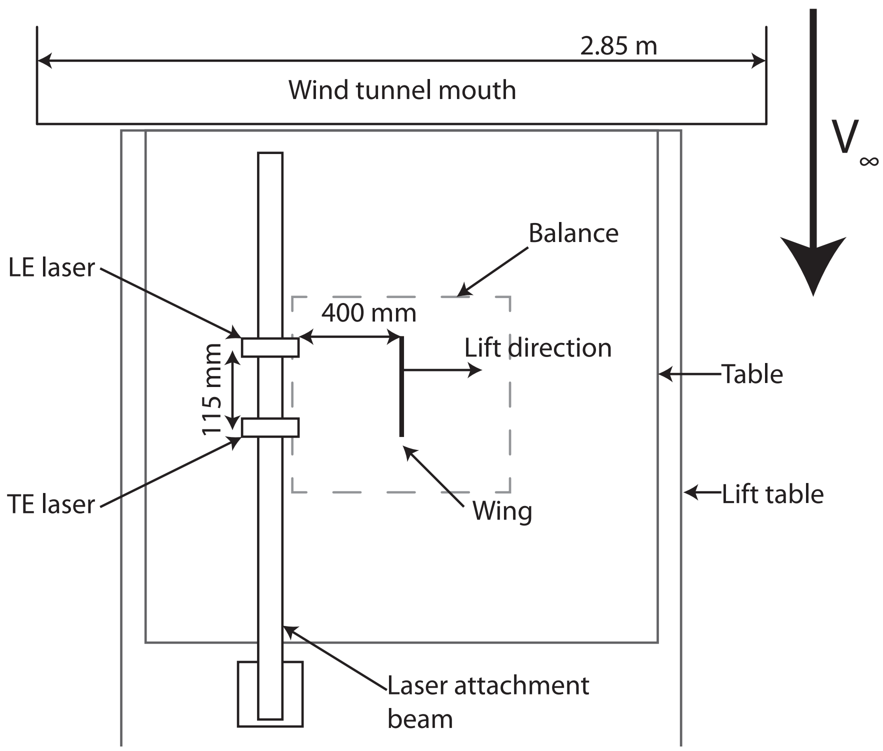

Figure 3.17: Schematic top view of the wind tunnel setup

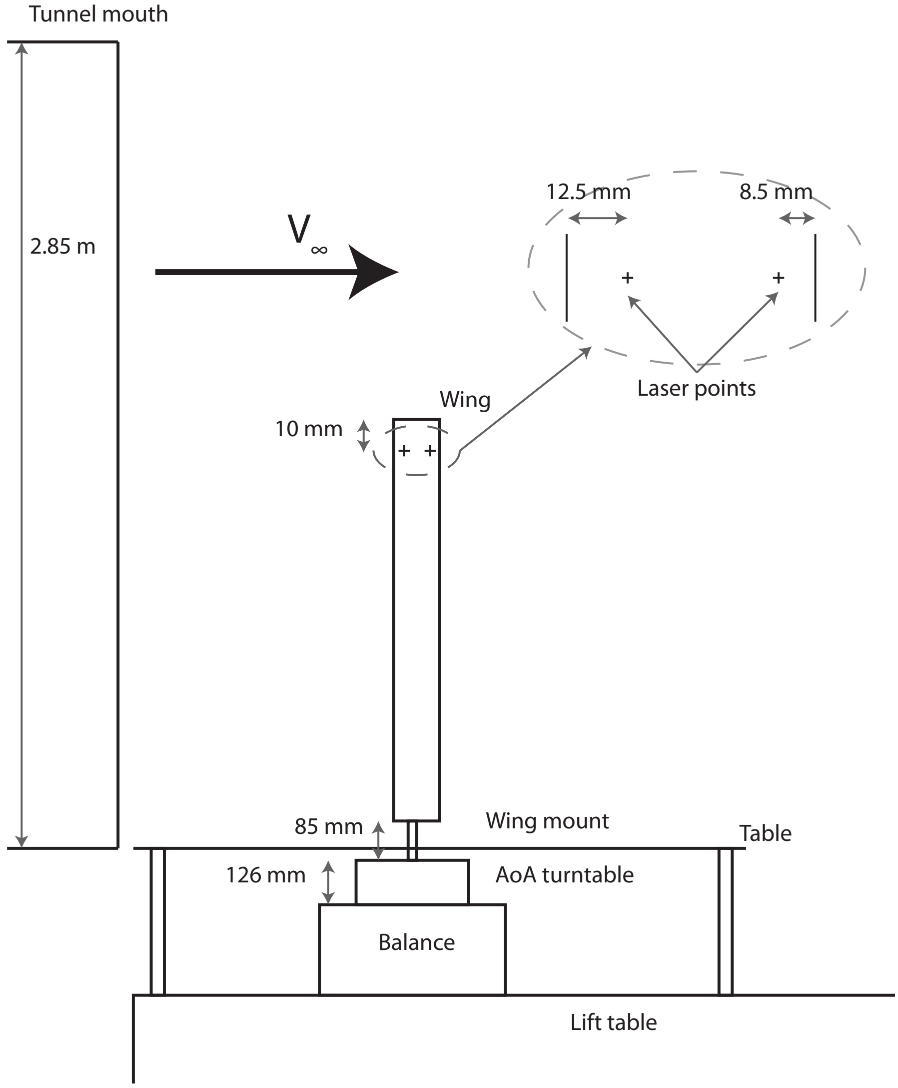

Figure 3.18: Schematic side view of the wind tunnel setup

3.3.2 Boundary Corrections

The results from the wind tunnel measurements do not fully represent the results that are obtained in unbounded or in "free air". The presence or absence of walls causes a difference in flow conditions. To compensate for these different flow conditions, correction factors are applied to the measured values. These changes of the flow conditions are determined according to Barlow et al. [29].

For this test setup the following effects are of importance:

Normal Downwash Change refers to the component of the induced flow in the lift direction at the test article. It is changed due to the finite distances to the boundaries. An open jet makes the lift too small and the drag too large at a given geometric angle of attack corresponding to a higher downwash at the test article than in an unbounded stream.
The change in angle of attack due to the boundaries is determined by

$$\Delta\alpha_{dc} = \delta \left(\frac{S}{C}\right) C_{LW} \tag{3.23}$$

where C_{LW} is the wing lift coefficient, S is the wing area, C is the tunnel cross sectional area and δ is the boundary correction factor. Furthermore the induced drag is lower than the wing would have under normal conditions. This correction is expressed as follows

$$\Delta C_{D,dc} = \delta \left(\frac{S}{C}\right) C_{LW}^2 \tag{3.24}$$

Streamline Curvature refers to an alternation of the streamline curvature in the flow about a body in a wind tunnel as compared to the corresponding curvature in an infinite stream. For a wing the moment coefficient, lift coefficient, and angle of attack are decreased in an open jet.
The change in angle of attack is determined by

$$\Delta\alpha_{sc} = \tau_2 \delta \left(\frac{S}{C}\right) C_{LW} \tag{3.25}$$

The amount of correction needed is most easily handled as a "τ_2" effect, which corrects for the boundary induced upwash at a point P behind the wing quarter chord. This so called "tail length" is set to $\frac{1}{4}c$ to determine the downwash correction factor τ_2. The additive lift correction is given as

$$\Delta C_{L,sc} = -\Delta\alpha_{sc} \cdot C_{LW_\alpha} \tag{3.26}$$

where C_{LW_α} is the wing lift curve slope. The additive correction to the moment coefficient is derived as

$$\Delta C_{m,sc} = -0.25 \cdot \Delta C_{L,sc} \tag{3.27}$$

The correction factors are determined in Appendix B resulting in a value of -0.127 for δ and 0.036 for τ_2.

With the use of semi span models, the largest possible model size can be created. Hence this creates the largest possible experimental Reynolds number. These models are called reflection plane models as they use a plane to "reflect" their behavior. However, under some conditions (e.g. aileron down, which normal situation is antisymmetric, as shown in Figure 3.19) the reflection is not exactly the condition that is desired. Therefore the tunnel measurement data include a small carryover from the reflection and will show from one-tenth to one-fourth more increment of lift, drag, pitching moment, yawing moment, and rolling moment than would occur for the actual asymmetric flight article.

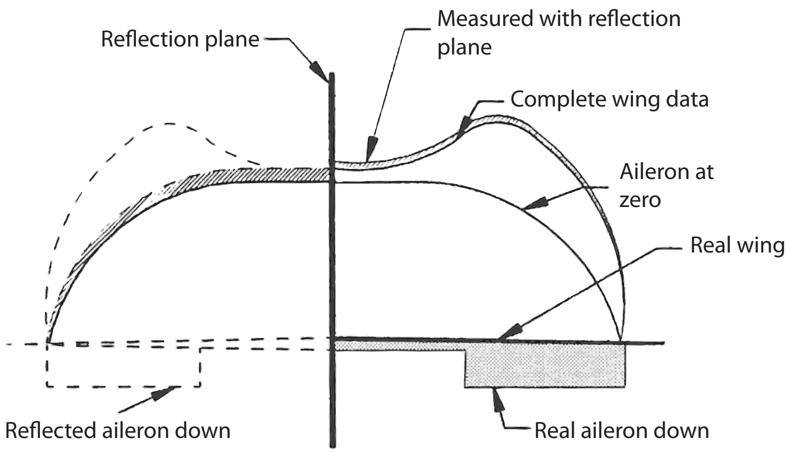

Figure 3.19: Effect of reflection plane on panel with aileron down[29]

To obtain the complete wing lift, drag, and pitching moment, the measured data are too large as they include the reflection. Thus wing data for the asymmetrical model (only one wing half has its control surface deflected) may be found from

$$C_L = \frac{1}{2}\left(C_{L,0} + C_{L,d}\right) \tag{3.28}$$

$$C_D = \frac{1}{2}\left(C_{D,0} + C_{D,d}\right) \tag{3.29}$$

$$C_m = \frac{1}{2}\left(C_{m,0} + C_{m,d}\right) \tag{3.30}$$

where the subscript d represents the asymmetric control deflection, and 0 the neutral control. The neutral control configuration is defined as the configuration where the main spar has no sweep angle.

In testing a semi span model of a wing, it is observed that a yawing and rolling moment about the centerline is produced which, in reality, would be canceled by the wing on the other side. Thus the actual moments can be obtained by subtracting the moments with the control surface in neutral position from the moments with the control surface deflected. This becomes then

$$C_l = C_{l,d} - C_{l,0} \tag{3.31}$$

To prevent the formation of a vortex at wing root, a cover has been created to fill the gap, shown in Figure 3.16, between the wing and the table. This cover is shown in Figure 3.20.

3.3.3 Experimental Variables

To identify the effect of the sweep angle on the rolling moment coefficient, several combinations of sweep angles and angle of attack are tested. The sweep angle, at 28% chord, varied from -20° (forward) to 20° (aft) and the angle of attack varied between 0 and 8°. All combinations that have been used are shown in Table 3.4.

Based on the results of these tests, the most beneficial sweep angle is chosen. At this sweep angle, additional higher angle of attack measurements are performed in order to complete the lift curve diagram. This is done for angles of attack from 9° until 12°, with increments of 1°, and for the five spar sweep angles. A summary of the measurement variables is shown in Table 3.5.

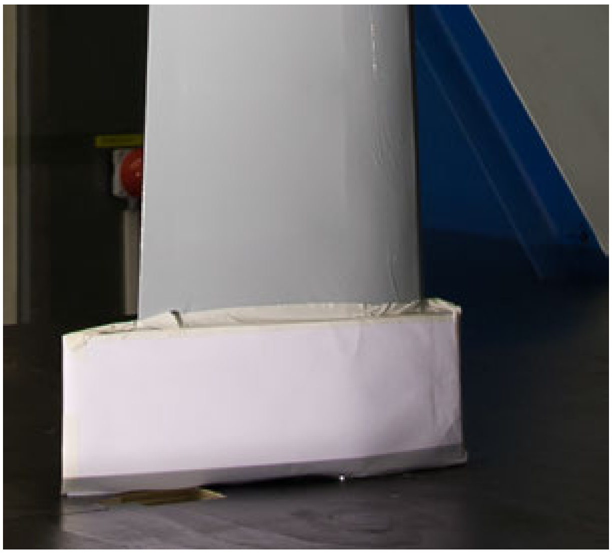

Figure 3.20: Photo of the wing root cover

Table 3.4: Measurement variables to identify the effect of sweep

Parameter		**Value**
Velocity	V	15 m/s
Sweep angle	$\Lambda_{0.28c}$	$-20°$, $-10°$, $-5°$, $0°$, $10°$, and $20°$
Angle of attack	α_r	$0°$, $4°$, $8°$
Main spar sweep angle	Λ_{sp}	$-1.68°$, $-0.80°$, $0°$, $1.56°$, and $3.20°$

Table 3.5: Measurement variables of the beneficial configuration

Parameter		**Value**
Velocity	V	15 m/s
Sweep angle	$\Lambda_{0.28c}$	To be determined
Angle of attack	α_r	$0°$, $4°$, $8°$, and 9 until $12°$ ($1°$ steps)
Main spar sweep angle	Λ_{sp}	$-1.68°$, $-0.80°$, $0°$, $1.56°$, and $3.20°$

3.3.4 Dynamic Test Setup

To determine if and at what velocity the wing is susceptible to flutter the wing is excited by pushing the trailing edge of the wing tip downwards. In Figure 3.21a the position is shown were the excitation, Figure 3.21b, is applied on the wing. The resulting oscillation, a combination of bending and pitching, of the wing is recorded with use of the two laser heads. After the oscillations is successfully damped out, the velocity is increased with 0.5 m/s. The velocity is increased until flutter occurs or the bending displacement become too large for the used setup.

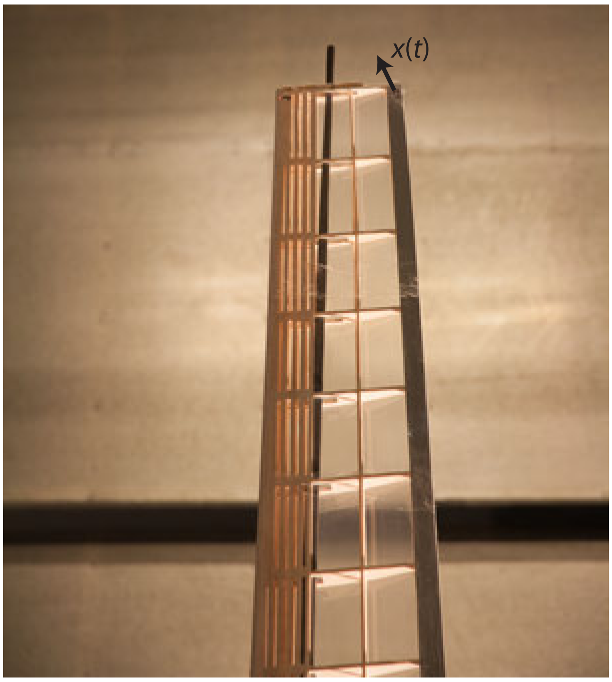

(a) Displacement of the trailing edge of the wing tip (photograph)

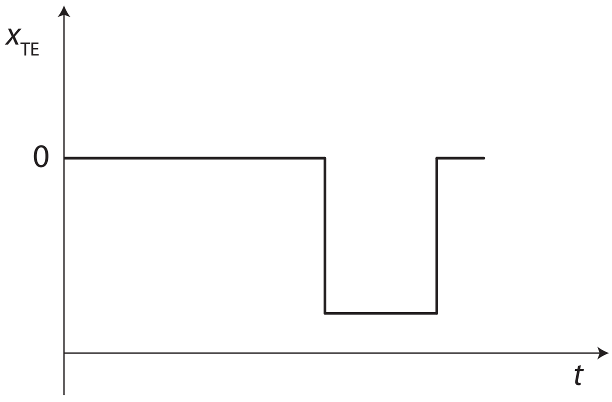

(b) Displacement versus time plot of the trailing edge

Figure 3.21: Excitation of the wing for flutter test

Chapter 4

Modeling Tool

At this stage, the concept for the aeroelastic part is known. The next step is to create a simulation model of the aeroelastic part in order to analyze the performance for different wing configuration. For simulation of aeroelastic behavior, several programs are available (e.g. MSC.Nastran and ZAERO). The most suitable program needs to be selected. Based on the selected program, the required modifications are discussed.

4.1 Simulation Programs

Flick et al.[38] states the following about conceptual design:

> Typically a conceptual design will undergo many changes very rapidly, and it is difficult to build the models and perform high fidelity analyses quickly enough to influence the conceptual design decisions.

Therefore the selected program should meet a certain level of fidelity that is able to analyze a concept quickly. To determine the performance of an active aeroelastic wing, several commercial and research programs are available. Such a program must be able to output the relevant parameters (e.g. twist angle, rolling moment, and bending deflection). The following programs have been considered:

ZAERO - Is a powerful engineering tool that integrates all essential disciplines required for advanced aeroelastic analysis.[39] Since the program itself does not provide the structural finite element solutions, a finite element method (FEM) program (Nastran based) is required to compute the structural free vibration solutions or normal modes solutions. Nevertheless this program is too advanced for the conceptual design and a license is not available at the university.

MSC.Nastran - Is a program that is capable of analyzing the structural deformations of a FEM model. To include aerodynamic loads MSC.Nastran can be extended with the Aeroelastic module. This module allows the calculation of the aeroelastic behavior of a wing.
For the aerodynamic calculations several theories (e.g. Doublet-Lattice Method, Strip theory)[40] can be used to determine the aerodynamic forces. The structural and aerodynamic loads are coupled by interpolating the connection between the structural and aerodynamic grids.
With the structural and aerodynamic meshes setup, the static and dynamic instability problems can be solved. To solve the dynamic problem and the equation of motion for the static problem, a k method[8] or p-k method[9] can be used.

Proteus - A generic morphing wing analysis and design framework for MATLAB developed by de Breuker et al.[41] for fast analysis of morphing wings incorporating aeroelastic effects (in the present tool only static aeroelastic effects are considered) and actuator energy. The framework is intended to aid quick preliminary design of morphing wing to trade-off contradictory requirements in a flight mission.

The type of wings that can be modeled with this program are assumed to be slender, so that the wing structure can be discretized using non-linear beam elements. For the modeling of the aerodynamics Weissinger's L-method[42] is used, which uses the modified lifting line theory to incorporate wing sweep. Based on a number of input variables, e.g. the specified planform, the number of beam elements, the stiffness properties at each node, and the number of aerodynamic panels, the undeformed mesh of the wing is calculated. The resulting aerodynamic forces and moments are calculated using the lifting line theory.

Based on the previously described characteristics, the Proteus aeroelastic program is selected for the design of the wing. There are a number of reasons why the other programs are discarded. ZAERO requires the use of an additional program to compute the structural response of the model. Furthermore the level of fidelity is too high for the current design stage and a license is not available. MSC.Nastran is also not selected since its level of fidelity and therefore the computational time is too high. Proteus is selected because of its fast and relatively simple to use framework. However the program has some limitations. The airfoil is assumed to be symmetric such that the lift at zero angle of attack is zero and the pitching moment coefficient about the aerodynamic center is zero.

4.2 Proteus Implementation

Within Proteus there are two types of actuation available: inter-rib mechanisms operating across a wing segment, and intra-rib mechanisms acting between two adjacent wing segments. With these actuation mechanisms virtually any shape can be obtained by distributing four morphing modes over the entire morphing wing.[41] Three of them are an intra-rib mechanism and one is an inter-rib mechanism. The intra-rib mechanisms are called wing shear, twist, and extension shown in Figures 4.1a until 4.1c and the inter-rib mechanism is called wing folding shown in Figure 4.1d.

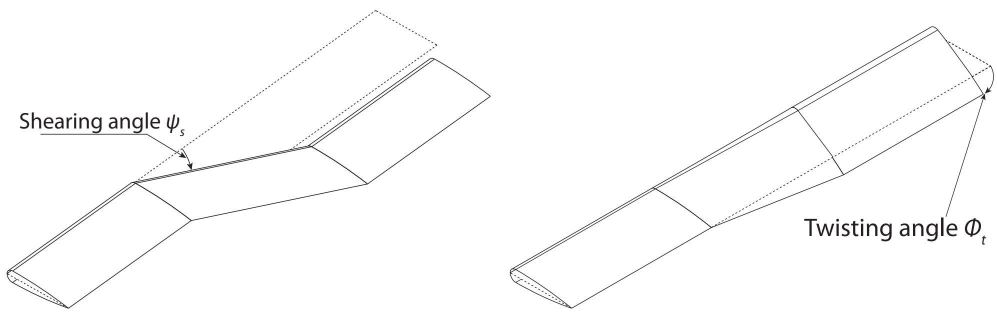

(a) Shear morphing (b) Twist morphing

Figure 4.1: Proteus' different morphing modes[41]
Note: Dashed line is the original configuration

The wings are discritized using non-linear beam elements, see Figure 4.1. Each beam element represents a wing segment. Such a wing segment is connected to an adjacent segment by a rib or chord on the one dimensional (1D) level, also called wing station. The transformation from a three dimensional wing to a 2D wing can be done adequately, when the cross-sectional properties of the 3D wing are well translated into nodal beam stiffness matrices.

For modeling the aerodynamic characteristics, Weissinger's L-method[42] is used. This method is a modified lifting line theory that incorporates the effects of wing sweep. Furthermore, large angles of attack are allowed by the brake up of the trailing vortices. Therefore, each horseshoe vortex is split up in a part that runs parallel to the wing and a part that extended from the trailing edge of the wing into the wake, parallel to the free stream, shown in Figure 4.2. Compressibility effects are

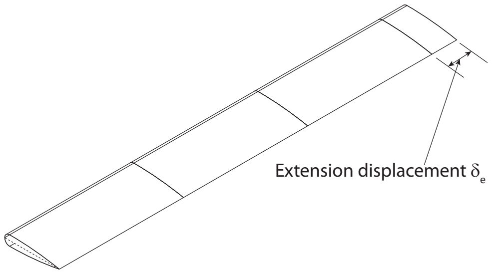

(c) Extension morphing

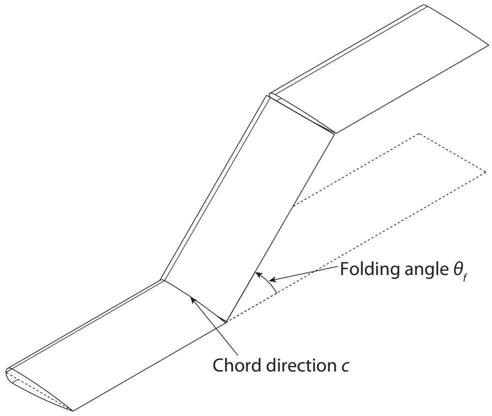

(d) Fold morphing

Figure 4.0: Proteus' different morphing modes[41] (cont'd)
Note: Dashed line is the original configuration

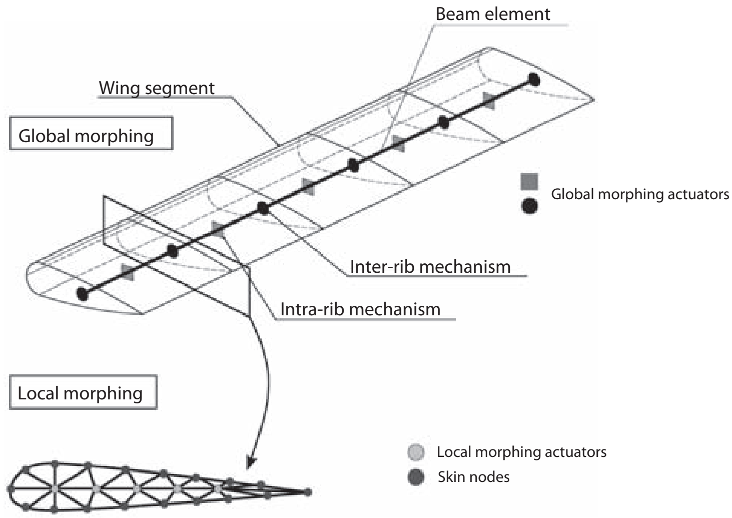

Figure 4.1: Proteus wing model[41]

incorporated by the use of the Prandtl-Glauert compressibility correction. Nevertheless, Weissinger's method does not allow the direct calculation of the viscous drag. Therefore an estimation is made by using the drag polar of the two dimensional airfoil sections.

Discretization of the morphing wing is done by specifying the number of horseshoe vortices and the number of beam elements that are used. Hereby, it is possible to place multiple horseshoe vortices on a single structural beam element. Consequently, the number of aerodynamic elements must always be equal or larger than the number of beam elements. The aerodynamic forces are calculated on each of the horseshoe vortex and converted to statically equivalent forces at the nodes of the corresponding structural beam.

4.3 Proteus Modifications

The original version of Proteus is not suitable for modeling the selected morphing mode concept, a sweepable spar. Therefore several modifications have been made to the structural and aerodynamic part to incorporate this concept. These modifications are described in this section.

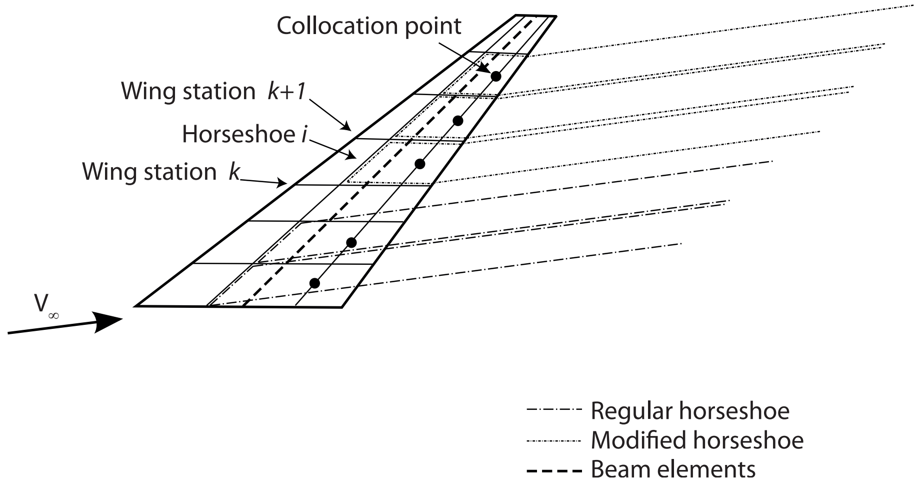

Figure 4.2: Modified horseshoe vortex for large angles of attack[43]

4.3.1 Structural Modifications

The concept of a sweeping spar has been implemented as a linear change of the elastic axis from the rotation point to the wing tip. A change of the elastic axis can be achieved by specifying the chordwise position of the elastic center at the tip or by the sweep angle of the elastic axis $\Lambda_{\text{ea,swept}}$, illustrated in Figure 4.3.

When the elastic center at the tip is specified some extra steps are required to calculate the new elastic axis. First the displacement caused by the sweep angle of the elastic axis $\Lambda_{\text{ea,fixed}}$ at the tip has to be calculated. This is done by

$$\Delta x = \Delta y_{\text{elas}} \cdot \tan\left(\Lambda_{\text{ea,fixed}}\right) \tag{4.1}$$

The change in the position of the elastic center at the wing tip is needed to determine the sweep angle of the elastic axis. This displacement is given by

$$\Delta\xi_{\text{tip}} = \xi_{\text{tip}} - \xi_{\text{fixed}} \tag{4.2}$$

where ξ is chordwise position of the elastic axis.

With the displacement of the swept elastic axis Δx and the shift of the elastic center $\Delta\xi_{\text{tip}} \cdot c_{\text{tip}}$ known, the sweep angle of the elastic axis can be determined by

$$\Lambda_{\text{ea,swept}} = \arctan\left(\frac{\Delta x + \Delta\xi_{\text{tip}} \cdot c_{\text{tip}}}{\Delta y_{\text{elas}}}\right) - \Lambda_{\text{ea,fixed}} \tag{4.3}$$

Now that the sweep angle of the elastic axis is known, the shift of the elastic center is calculated for every position on the aeroelastic section with

$$\Delta\xi\left(y\right) = \frac{\left|y - y_{\text{rot. point}}\right|}{c\left(y\right)} \left[\tan\left(\Lambda_{\text{ea,fixed}} + \Lambda_{\text{ea,swept}}\right) - \tan\left(\Lambda_{\text{ea,fixed}}\right)\right] \tag{4.4}$$

requiring the absolute distance to the rotation point $|y - y_{\text{rot. point}}|$, the chord at position y, the sweep angle of the elastic axis $\Lambda_{\text{ea,fixed}}$ and the sweep angle of the sweepable elastic axis $\Lambda_{\text{ea,swept}}$. The new distance between the leading edge and elastic center is thus

$$\xi\left(y\right) = \xi_{\text{fixed}} + \Delta\xi\left(y\right) \qquad \text{for } -y_{\text{rot. point}} > y > y_{\text{rot. point}} \tag{4.5}$$

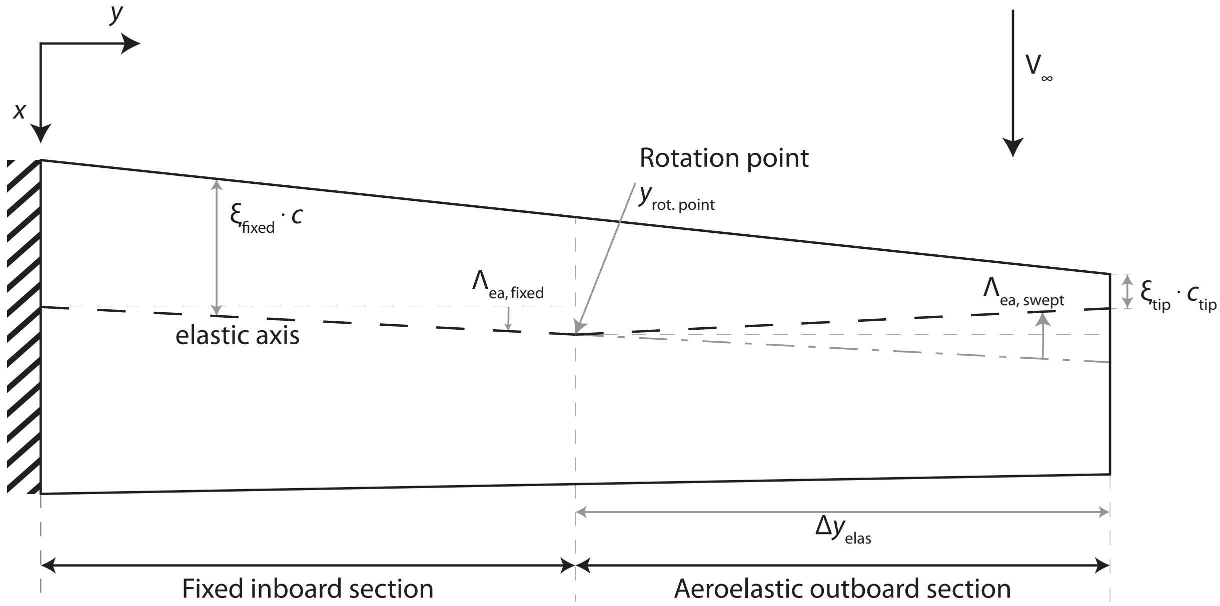

(a) Complete wing

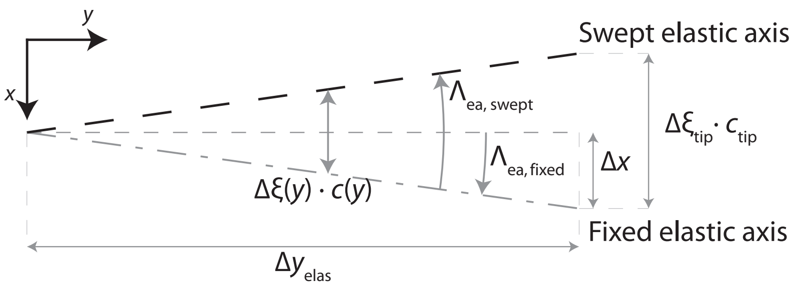

(b) Detailed view of the elastic axis on the aeroelastic section

Figure 4.3: Determine sweep angle of the sweepable spar

In Figure 4.4 the resultant model (the left wing only) is shown, where the structural nodes are represented by the dots and the aerodynamic elements by the quarter chord line.

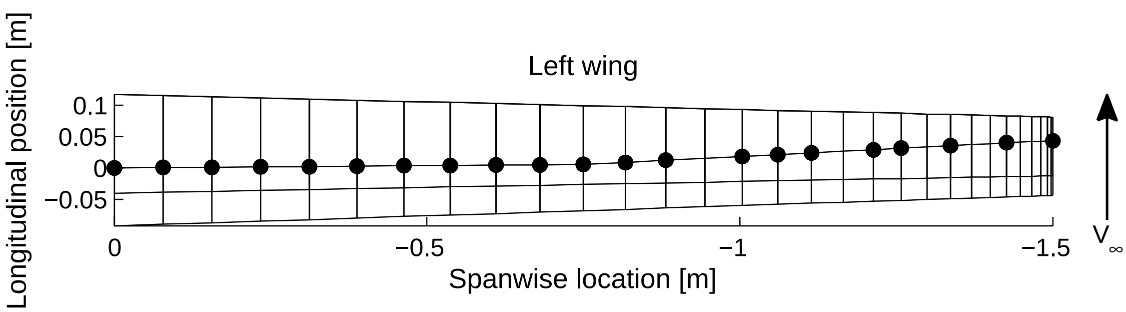

Figure 4.4: Wing model in Proteus – elastic axis moved aft

Now the elastic axis has been positioned on the correct place, the only structural item that needed to be adjusted is stiffness distribution of the wing. This is done by specifying the Timoshenko stiffness matrix at every structural node. The coupling between bending and torsion has been neglected, so the Timoshenko stiffness matrix becomes

$$C = \begin{bmatrix} EA & 0 & 0 & 0 & 0 & 0 \\ 0 & k \cdot GA & 0 & 0 & 0 & 0 \\ 0 & 0 & k \cdot GA & 0 & 0 & 0 \\ 0 & 0 & 0 & GJ & 0 & 0 \\ 0 & 0 & 0 & 0 & EI_{22} & 0 \\ 0 & 0 & 0 & 0 & 0 & EI_{33} \end{bmatrix} \tag{4.6}$$

To determine the Timoshenko stiffness matrix several experiments, described in Section 3.2, have been carried out for the inboard and outboard segments. With these experiments the flexural rigidity EI_{22} and torsional rigidity GJ have been determined. When these parameters are implemented in this form, a uniform stiffness distribution along the span is created on both wing parts. Such a distribution is not correct since it is a tapered wing and therefore the area of a wing section decreases when the spanwise location is increased. Consequently the second moment of area I and torsion constant J also vary with the span position. The remaining parameters that need to be set are EA, GA and EI_{33}. According to De Breuker[44], the properties EA and GA can be assumed to be infinite stiff, i.e. $5 \cdot 10^2$ Nm^4. Furthermore, EI_{33} can be set to ten times the value of EI_{22}.

To obtain a better distribution of the stiffness along the wingspan, the wing is represented by a conical cylinder, as described in Section 3.2.1. With the Young's and shear modulus determined in Section 3.2 a varying Timoshenko stiffness matrix can be created.

4.3.2 Aerodynamic Modifications

To incorporate cambered airfoils in Proteus several modifications have been made to the calculations of the lift force and pitching moment. In Figure 4.5 the relevant parameters are shown that are used in the modifications. The width of an element is given by l_i, the wing surface of an element is S_i and the average chord is obtained by

$$c_{\text{avg},i} = \frac{S_i}{l_i} \tag{4.7}$$

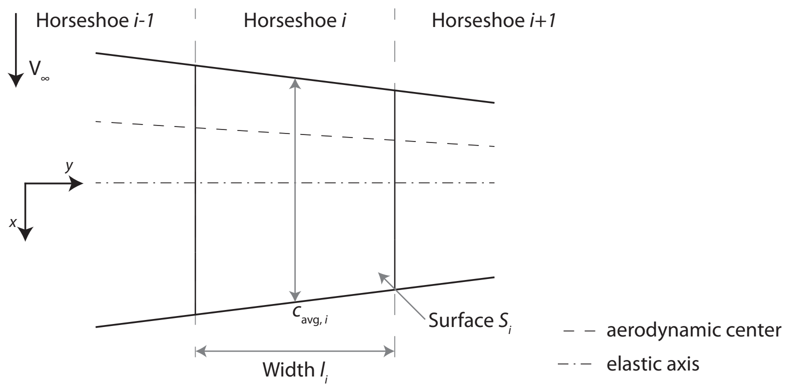

Figure 4.5: Uniform aerodynamic mesh with relevant parameters

For the lifting line theory the lift force generated by a horseshoe vortex at zero angle of attack is equal to zero. This is calculated by

$$L_i' = \rho V \Gamma_i l_i \tag{4.8}$$

To allow the usage of cambered airfoils, the wing lift coefficient at zero angle of attack has been added to Equation (4.8). This resulted in the following equation

$$L'_i = \rho V \Gamma_i l_i + C_{L_{\alpha=0}} \cdot \frac{1}{2} \rho V^2 S_i \tag{4.9}$$

where $C_{L_{\alpha=0}}$ is determined from the wind tunnel test results.

Furthermore, the pitching moment of symmetric airfoils is created by the lift force L' and the distance between the quarter chord point and elastic axis, $(x_\xi - x_{\mathsf{ac}})_i$. This is expressed as

$$M'_i = (x_\xi - x_{\mathsf{ac}})_i \, L'_i \tag{4.10}$$

The calculation of the pitching moment for cambered airfoils is improved by adding the airfoil pitching moment around the aerodynamic center to Equation (4.10). This gives the following equation

$$M'_i = (x_\xi - x_{\mathsf{ac}})_i \, L'_i + c_{m_{\mathsf{ac}}} \cdot \frac{1}{2} \rho V^2 S_i \, c_{\mathsf{avg},\, i} \tag{4.11}$$

where $c_{m_{ac}}$ is the two dimensional pitching moment coefficient of the airfoil. Pinkerton and Greenberg[45] give a pitching moment coefficient of -0.069 for the Clark Y airfoil, which is obtained by wind tunnel tests.

The final modification to the program that had to be made is the implementation of the rolling moment calculation. On each aerodynamic segment the lift force, L', is calculated on the midpoint of each segment. Therefore the moment around the center line is calculated as

$$l = \sum_{i=1}^{N_a} -y_{\mathsf{mid},\, i} \cdot L'_i \tag{4.12}$$

where $y_{\mathsf{mid},\, i}$ is the distance from the centerline to the midpoint and a rolling motion turning the right wing down is defined as positive.

Chapter 5

Results

In this chapter, the results of the performed tests and simulations are shown and compared. First, the bench test results are shown in Section 5.1. From these tests the position of the elastic center at the wing tip has been determined. Furthermore the variation of the stiffness parameters have been determined for the different sweep angles of the main spar, Λ_{sp}. Figure 5.1 shows how this angle is defined. These parameters are used to improve the simulation model.

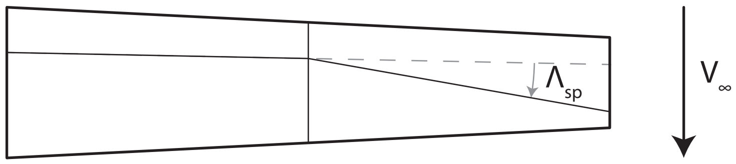

Figure 5.1: Main spar sweep angle definition

Section 5.2 presents first the results of the wind tunnel tests, to identify the effect of the sweep angle on the rolling moment coefficient of the semi span wing. From these results, the configuration is chosen that gives the best rolling moment over the angle of attack range (0° until 8°). For the chosen configuration a number tests are carried out at larger angles of attack. This configuration is compared to the results produced by the Proteus simulation. After the aerodynamic results of the test article are shown, the dynamical behavior of the wing is presented in Section 5.3 to see if and when flutter occurs.

Finally the maximum roll performance for a complete wing is presented in Section 5.4. Based on these results a comparison is made with aircraft that use ailerons for roll control (i.e. the Global Hawk and Boeing 747-200).

The first results are shown on the next page to keep the text and graph together.

5.1 Bench Tests

In this section the results of the structural test are presented. These results are needed to obtain a correct representation of the test article that has been used for the wind tunnel test. First the results of the elastic center position at the wing tip are shown. Followed by the bending and shear modulus determined from the bending and torsion tests.

5.1.1 Elastic Center

The first wing property that has been determined is the location of the elastic center at the wing tip for the different main spar positions. In Figure 5.2 the results of the different main spar sweep angles are shown. From this graph it is clear that there is a linear relation between the main spar sweep angle and the relative position of the elastic center at the tip of the wing. The elastic center at the tip can be shifted from 15.5% chord to 53.7% chord, resulting in a 38.2% position shift of the elastic center.

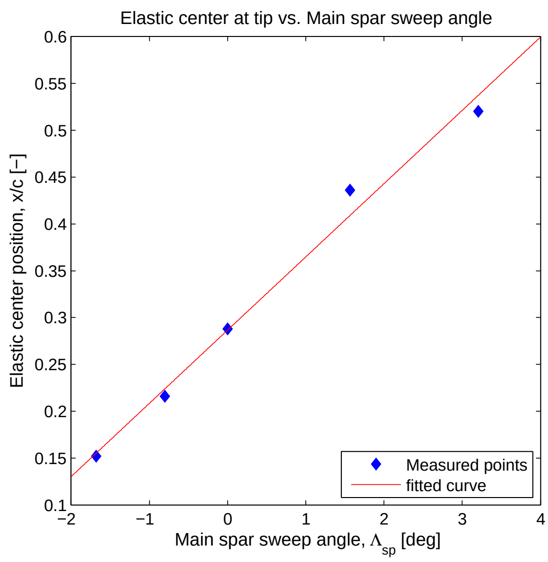

Figure 5.2: Variation of the elastic center at the tip for different main spar positions

Compared to the position of the elastic center at 40% chord, on the inboard segment, it can be moved 24.5% forward and a smaller distance, 13.7%, aft. With this range of the elastic center at the wing, the pitching moment of a wing section can be changed to decrease or increase the local twist angle.

With the position of the elastic center at the wing top known, the different configurations for the Proteus model can be created. These different configurations are shown in Figure 5.1.

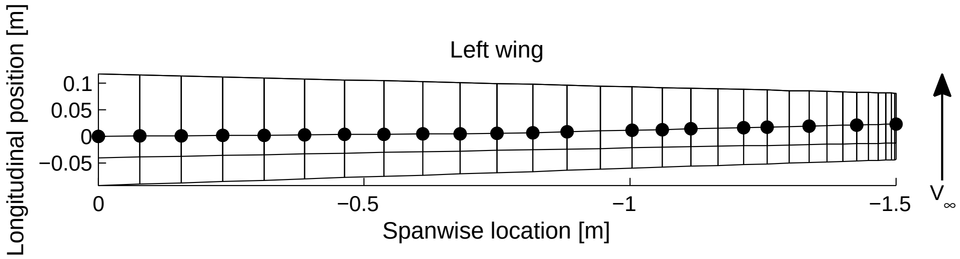

(c) Proteus configuration for $\Lambda_{sp} = 3.20^{\circ}$

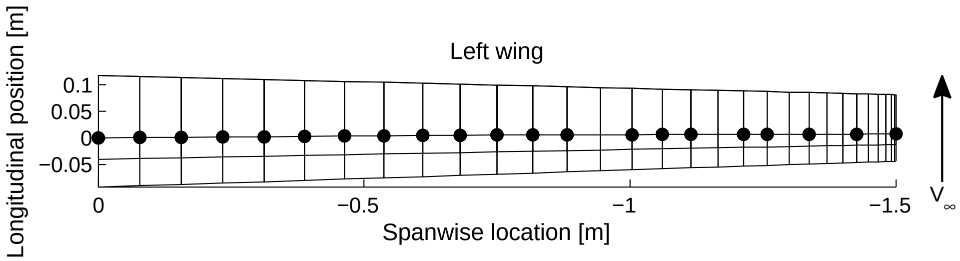

(d) Proteus configuration for $\Lambda_{sp} = 1.56^{\circ}$

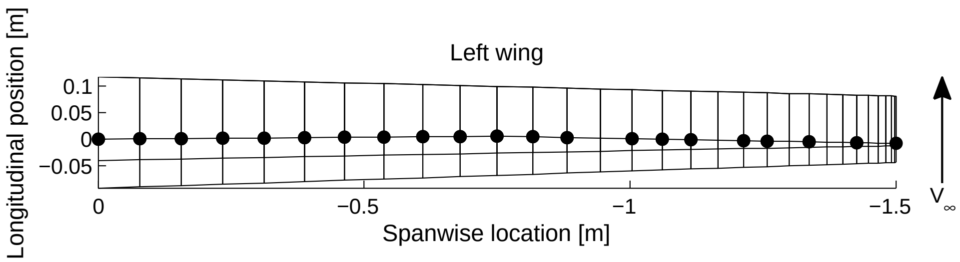

(e) Proteus configuration for $\Lambda_{sp} = 0.00^{\circ}$

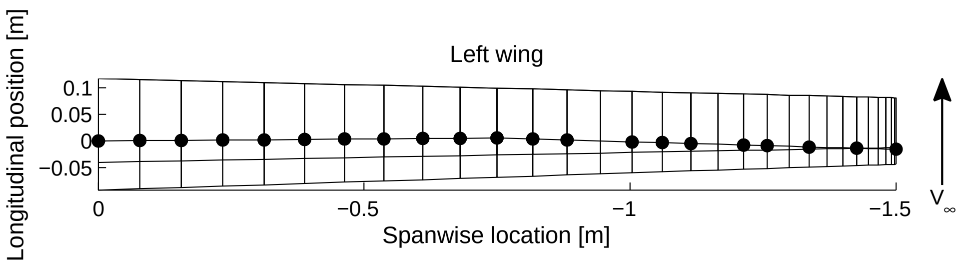

(f) Proteus configuration for $\Lambda_{sp} = -0.80^{\circ}$

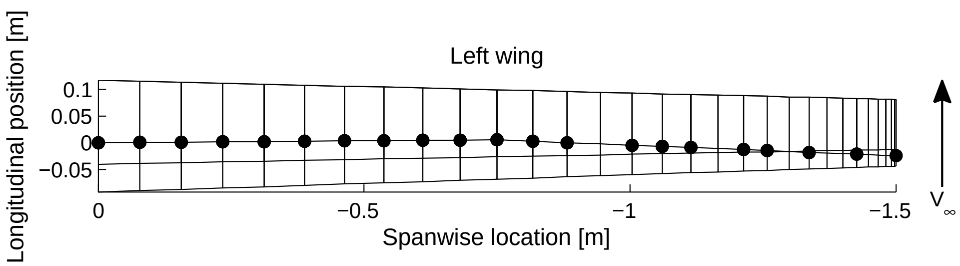

(g) Proteus configuration for $\Lambda_{sp} = -1.68^{\circ}$

Figure 5.1: Proteus wing configurations for the different spar positions (cont'd)

5.1.2 Stiffness Parameters

With the use of the method described in Section 3.2, the stiffness parameter of the outboard and inboard segment of the test article are determined. For both segments the stiffness parameter versus the applied force or torque is plotted. Additionally the variation of the stiffness with the main spar sweep angle is determined for the outboard segment.

In Figure 5.2a, the Young's modulus, of aeroelastic wing segment, for several applied forces is shown. From this graph can be seen that the Young's modulus converges to a certain value with increasing force. However, the measurements with the lower applied force misrepresent the stiffness and are for that reason not used in determining the bending stiffness.

Therefore only the last three points are used in determining the quadratic regression fit of the bending stiffness shown in Figure 5.2b. This quadratic fit is represented by

$$E\left(\Lambda_{\text{ea,swept}}\right) = 4.089 \cdot 10^5 \Lambda^2_{\text{ea,swept}} + 1.552 \cdot 10^5 \Lambda_{\text{ea,swept}} + 40.28 \cdot 10^6 \tag{5.1}$$

with $\Lambda_{\text{ea,swept}}$ in degrees.

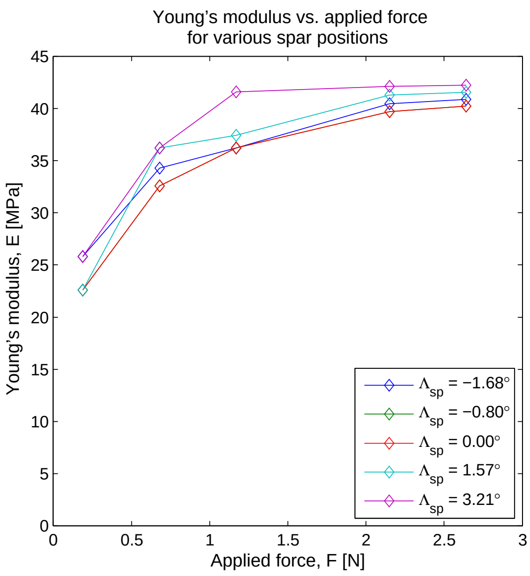

(a) Young's modulus versus the applied force

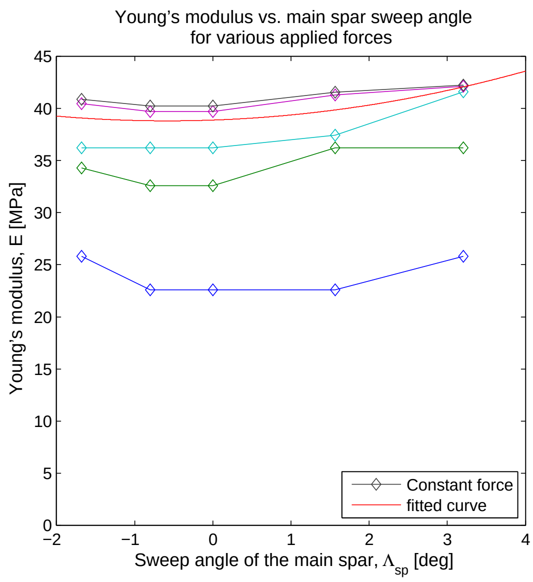

(b) Young's modulus versus main spar sweep angle

Figure 5.2: Young's modulus of the aeroelastic wing segment

For the aeroelastic part the variation of the shear modulus is shown in Figure 5.3. From this graph a spread of the measurement values can be seen. Because of the spread in the measurement results, a fitted curve does not represent the behavior of the actual wing model. Another observation that can be made, is that the torsional stiffness increases when the spar is swept from $-0.80°$ to $-1.68°$.

Figure 5.4 shows the measurement results of the inner wing section. The first four measurement points of the rigid segment showed the same behavior as the aeroelastic segment. Therefore the first four points are neglected in calculating the mean value. This resulted in a Young's modulus of 53.8 MPa. In Figure 5.4b a small spread in the measurement results of the shear modulus is shown. By taking the mean value of these points, a shear modulus of 20.3 MPa has been determined. This is about ten times larger than the aeroelastic section.

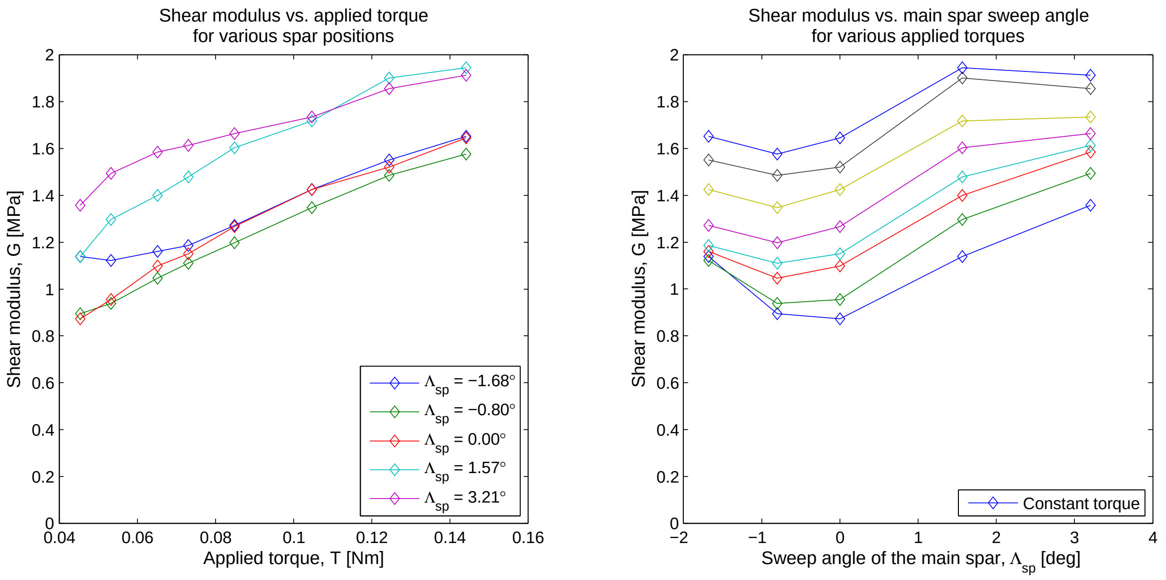

(a) Shear modulus versus the applied torque (b) Shear modulus versus main spar sweep angle

Figure 5.3: Shear modulus of the aeroelastic wing segment

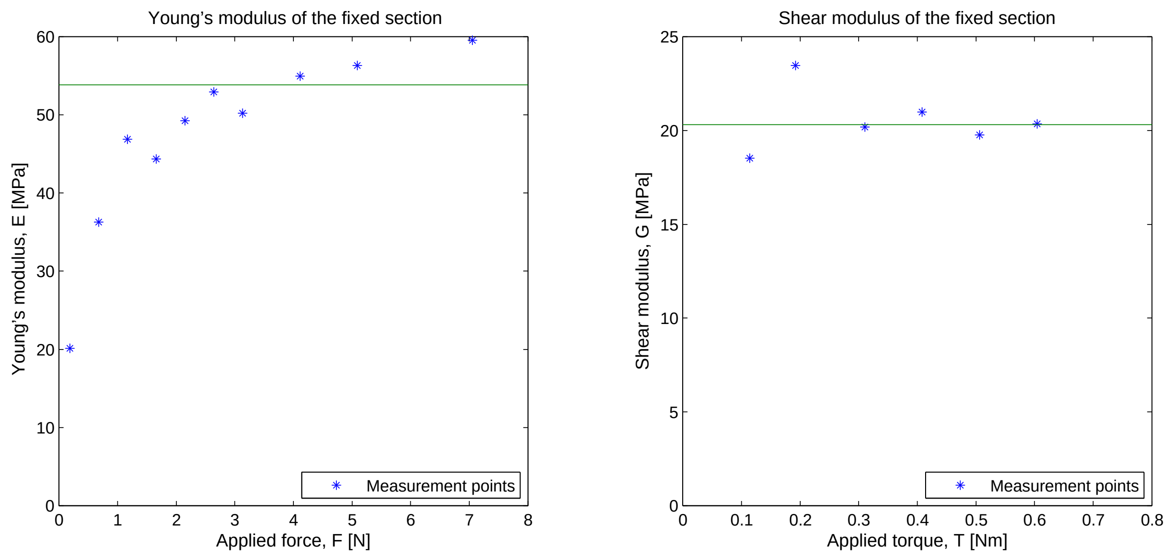

(a) Young's modulus versus the applied force (b) Shear modulus versus the applied torque

Figure 5.4: Stiffness measurements of the inboard wing segment

5.2 Simulation and Wind Tunnel Results of the Semi Span Model

This section shows the results of the Proteus simulation and the wind tunnel tests. First, the effect of wing sweep on the rolling moment is tested during the wind tunnel tests. To determine the effect of wing sweep, six sweep angles have been tested varying from -20° to 20°. Based these results, a configuration has been chosen and further analyzed during the wind tunnel tests and in the Proteus simulation.

During the wind tunnel tests, the target velocity of 15 m/s was too high, since the resulting bending displacement was too high for zero degrees of angle of attack. Therefore the velocity has been reduced to 5 m/s to keep the bending displacement at a safe limit of around 50 mm.

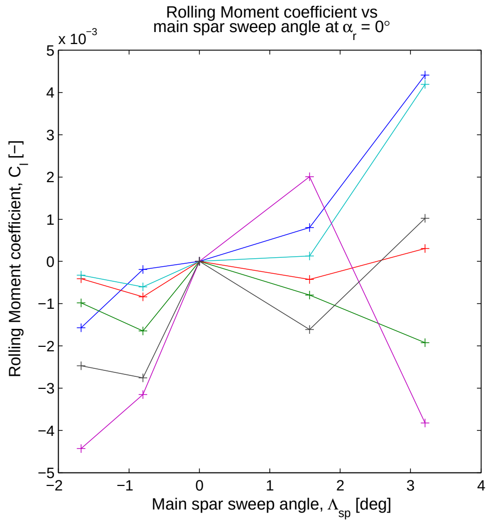

(a) Rolling moment coefficient for $\alpha_r = 0^\circ$

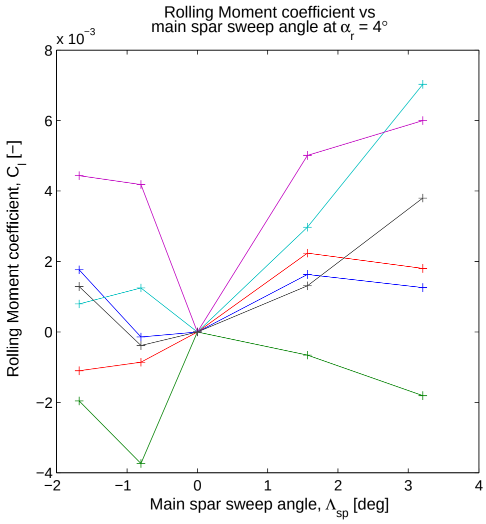

(b) Rolling moment coefficient for $\alpha_r = 4^\circ$

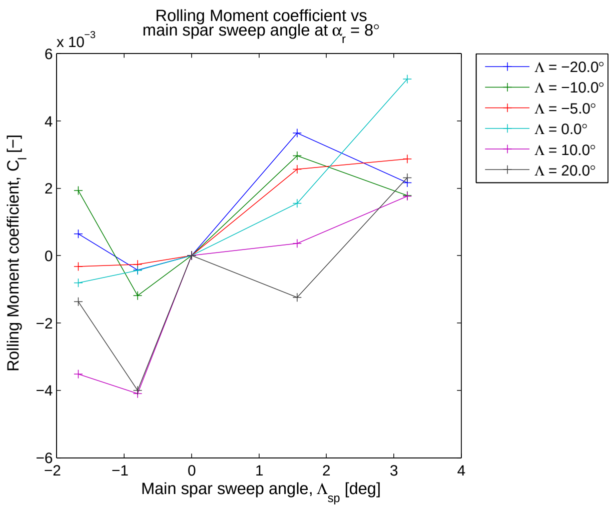

(c) Rolling moment coefficient for $\alpha_r = 8^\circ$

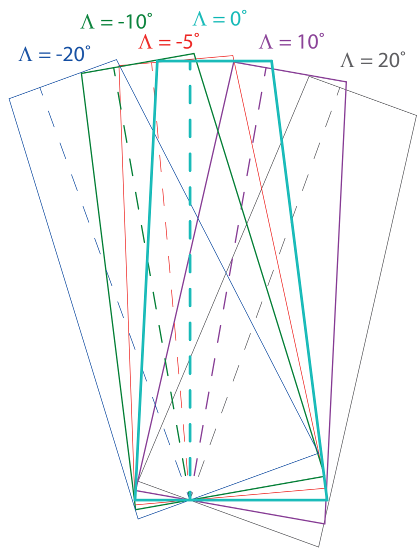

(d) Different configurations

Figure 5.5: Rolling moment coefficient versus main spar sweep angle for different angles of attack

To determine the most beneficial configuration of the test article, several sweep angles are tested. These results are presented in Figure 5.5. Based on these results, the configuration with no sweep has been chosen. Since the overall results of this configuration are the most constant over the tested range of angles of attack. The configurations with forward sweep (i.e. $\Lambda_{0.28c} < 0$) are not showing any beneficial effects of the aerodynamic twist. Furthermore these configurations show inconsistent behavior for the different angles of attack. For the two configurations with aft sweep (i.e. $\Lambda_{0.28c} > 0$) also different behavior is seen for the angles of attack.

5.2.1 Initial Proteus Results

With the chosen sweep configuration, of $\Lambda_{0.28c} = 0^\circ$, the angle of attack range, of the wind tunnel tests, has been extended to 12°. These results of the wind tunnel experiments are compared to the results produced by Proteus.

In Figure 5.6 the initial results of the Proteus simulation are shown. The lift coefficient versus angle of attack plot, Figure 5.6a, shows a difference in the lift curve slope between the wind tunnel data and simulation results. This difference is caused by the viscous effects which are not included in the lifting line theory that is used by Proteus. A more detailed explanation is given in Section 5.2.2.

The twist angle at the wing tip is shown in Figure 5.6b. Because of the difference in lift curve slope, two extra angles of attack for the Proteus simulation are added. These angles of attack, 2.75° and 5.75°, have the same lift coefficient as the wind tunnel test for an angle of attack of 4° and 8°. The twist angle for the wind tunnel tests remain negative over the complete range, while the results from Proteus become positive when the main spar is swept.

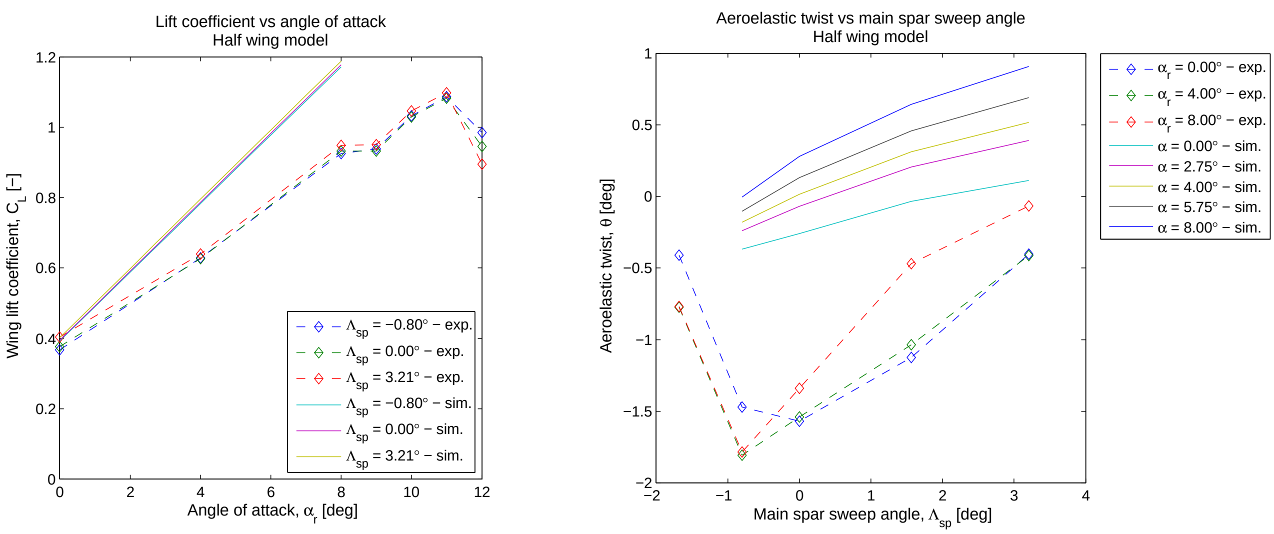

(a) Lift coefficient versus angle of attack

(b) Tip twist versus main spar sweep angle

Figure 5.6: Results of the initial Proteus simulation

To determine were this difference in twist angle comes from, an airfoil section has been drawn with its parameters on it, shown in Figure 5.7. The shown parameters that affect the twist angle can be divided into two categories. One that determines the moment and one that represents the material properties. These parameters are

- Moment parameters:
  - the aerodynamic moment coefficient, $c_{m_{ac}}$
  - the lift force, L'
  - the distance between the aerodynamic center and elastic center, $(x_\xi - x_{\text{ac}})$

- Material properties:
  - the shear modulus, G
  - the torsion constant, J

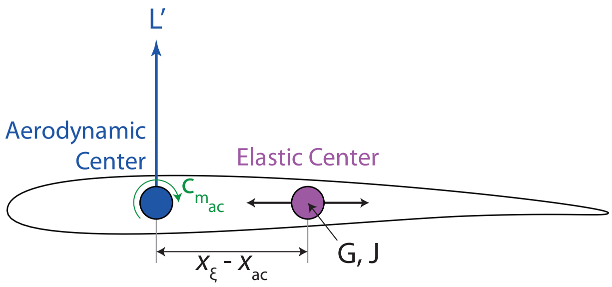

Figure 5.7: Airfoil twist causes

The parameters in the moment category define the sign of the resultant twist angle. This moment is calculated by

$$M_i' = (x_\xi - x_{\mathsf{ac}})_i \, L_i' + c_{m_{\mathsf{ac}}} \cdot \frac{1}{2}\rho V^2 S_i \, c_{\mathsf{avg},\,i} \tag{5.2}$$

The resulting twist angle can be calculated by the following approximate equation

$$\theta = \frac{lM_i'}{GJ} \tag{5.3}$$

stating the relation between the moment and material properties. This relation shows that the shear modulus only affects the magnitude of the twist angle.

5.2.2 Adjusted Proteus Results

In order to match the simulation data with the measured data, the model needs to be adjusted. From Equation (5.2) can be seen that the magnitude of the twist angle can be increased by adjusting the distance between the aerodynamic center and elastic axis. By adjusting this distance with 5%, the resulting twist was still too large. Another option is to adjust the aerodynamic moment coefficient. Multiplying the aerodynamic moment coefficient with three results into:

$$c_{m_{ac}} = -0.069 \cdot 3 \tag{5.4}$$

Using this new aerodynamic moment coefficient, a negative pitching moment is obtained along the complete span of the wing. With this negative pitching moment the amplitude of the twist angle can be fine tuned by adjusting the shear modulus. This fine tuning resulted into a shear modulus G of 1.83 MPa for the most aft position ($\Lambda_{sp} = 3.21°$) and to 1.17 MPa for the spar at $\Lambda_{sp} = -0.80°$. In Figure 5.8a the wing lift curve is shown for three main spar sweep angles of the semi span model. The average lift curve slope, of the wind tunnel test, has been determined between an angle of attack of $0°$ and $8°$ resulting in a C_{L_α} varying between 3.90 and 4.00 per radian. For the Proteus simulation the same procedure has been applied, resulting in a C_{L_α} varying between 5.55 and 5.63 per radian. Figure 5.8a also shows that the half wing stalls between an angle of attack of $11°$ and $12°$. The variation of the lift coefficient created by changing the sweep angle of the main spar is shown in Figure 5.8b. From this figure can be seen that the impact of changing the sweep angle is in the order of hundredths (0.02 until 0.036).

The differences between the lift force obtained by Proteus and wind tunnel data is caused by the fact that viscous effects are neglected in Proteus due to the usage of the lifting line theory. One of the

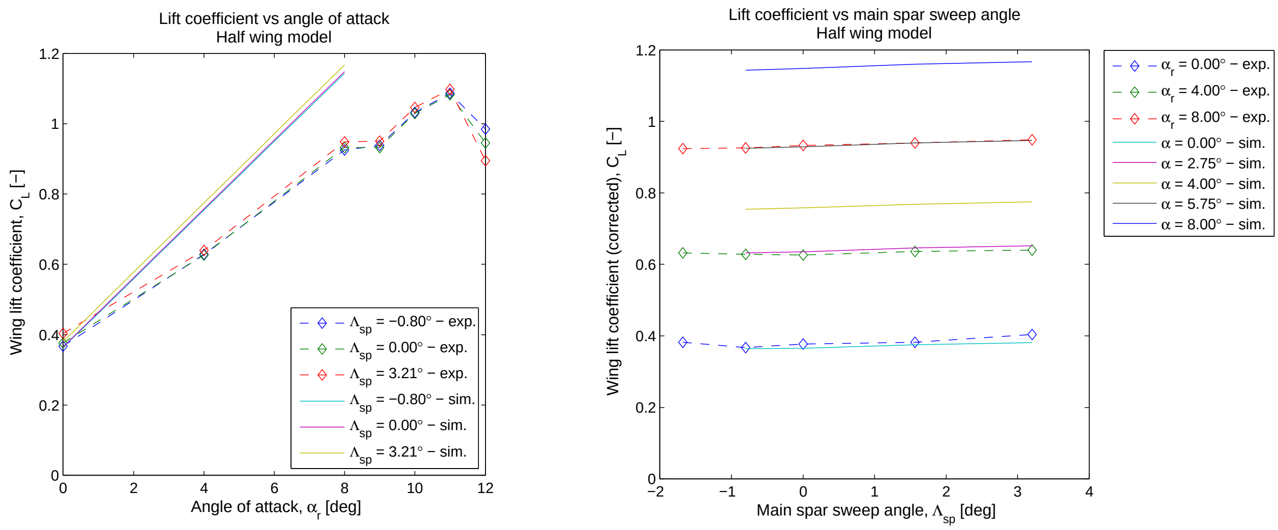

(a) Half wing lift coefficient versus angle of attack

(b) Corrected half wing lift coefficient versus main spar sweep angle for several angles of attack

Figure 5.8: Lift coefficient of the semi span model

effects of a viscous flow is that it forms a boundary layer on a body in a moving fluid. The formation of a boundary layer reduces the actual curvature of a body. Due to this curvature reduction, the lift curve slope is lowered. The influence of the viscous effects can be determined with the Reynolds number, which is a measure of the ratio between inertia and viscous forces. For the wind tunnel tests the Reynolds number was $56,655$.

Figure 5.9 shows the measured rolling moment l of the half wing model with the applied correction for the offset between the balance center and wing root. In this plot a significant difference can be seen. For a simulation angle of attack of $2.75°$, which has the same lift coefficient as the wind tunnel test at $4°$, the difference is 0.5 Nm.

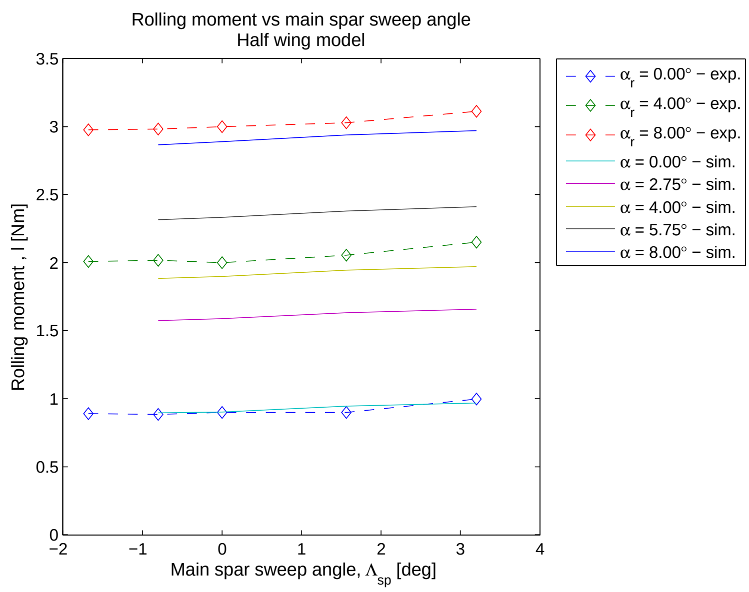

Figure 5.9: Rolling moment of the semi span model

At a higher angle of attack of $5.75°$, corresponding to $8°$ for the wind tunnel test, the difference is increased to 0.7 Nm. Based on this observation it can be said that the outboard segment of the wind tunnel model has a greater lift force than is calculated for the Proteus model. A possible cause for this difference can be the geometric twist that has been induced during the manufacturing of the test article.

The rolling moment coefficient is calculated as follows

$$C_l\left(\Lambda_{sp}\right) = C_{l,\mathrm{m}}\left(\Lambda_{sp}\right) - C_{l,\mathrm{m}}\left(\Lambda_{sp} = 0°\right) \tag{5.5}$$

From this equation can be seen that the main spar sweep angle of $0°$ is used as the control neutral position. The results shown in Figure 5.10 is based on this equation, with a variation of the main spar sweep angle. For a main spar sweep angle of $-1.68°$ the rolling moment coefficient is increased, shown in Figure 5.10, instead of the expected decrease. This increase of the rolling moment is caused by the increase of the torsional rigidity for this main spar position, as shown in Figure 5.3b.

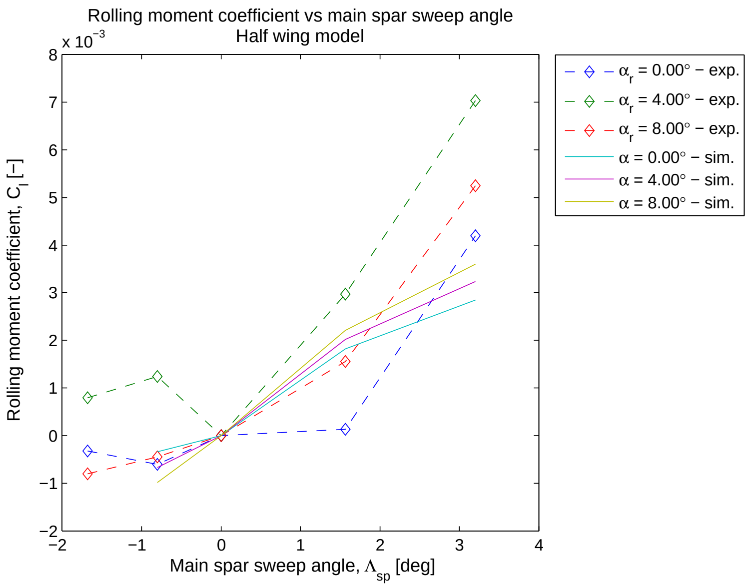

Figure 5.10: Rolling moment coefficient

In Figure 5.11 the tip twist is shown. When the spar is placed in the most forward position an increase of the twist angle is shown instead of a continuing decrease. This increase is caused by the raised shear modulus when the spar is positioned in the most forward position. Therefore the spar position, with a sweep angle of $-0.80°$ is set as the most forward position. This results in a rotation range for the main spar varying between $-0.80°$ and $3.21°$. Within this range a maximum variation in twist angle of $1.7°$ is measured.

The results of the Proteus simulation are very similar to the wind tunnel results except for a sweep angle of $-0.80°$ and $0°$. Especially at the forward position a larger difference is noticed. This difference can be caused by the assumption that the elastic axis changes linearly from the hinge point to the wing tip. Another reason can be the underestimation of the lift contribution of the outer segment of the wing. Which has been discussed at the rolling moment curves.

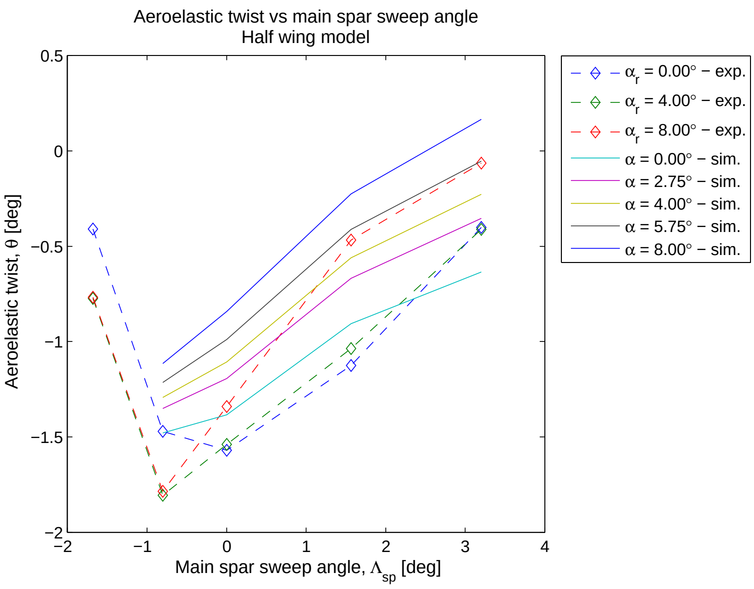

Figure 5.11: Tip twist versus main spar sweep angle

5.3 Dynamic Tests

Based on the description of Section 3.3.4, the flutter tests have been carried, starting at a velocity of 5.0 m/s. Moreover the test article has been positioned at the most critical configuration, i.e. angle of attack of 8° and the main spar sweep angle at 3.20°. For this configuration the largest lift force is generated and the distance between the aerodynamic and elastic center is the largest.

In Figure 5.12 the measured displacements are shown for the test velocities. The resulting vibration of the applied excitation is a combination of a bending and pitching motion. For the three test velocities the resulting vibration damps out successfully.

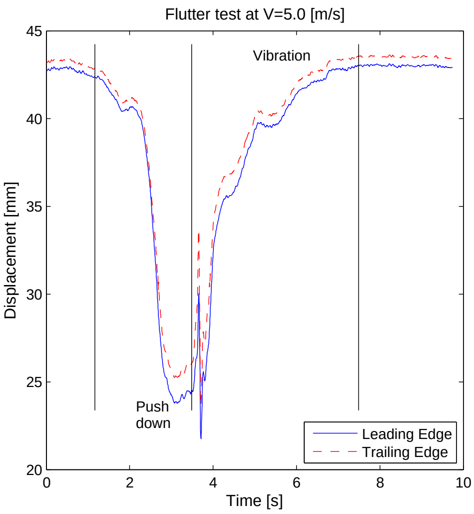

(a) $V = 5.0$ m/s

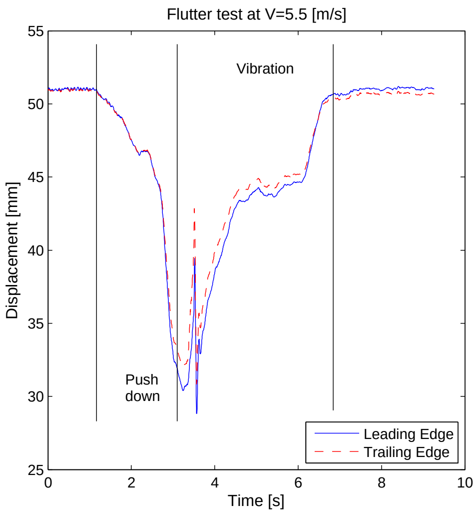

(b) $V = 5.5$ m/s

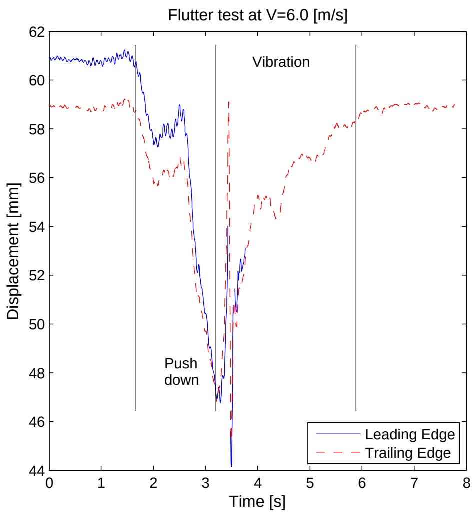

(c) $V = 6.0$ m/s

Figure 5.12: Measured response of the wing tip for various velocities

From Figure 5.12c can be noted that the displacement after approximately four seconds disappears from the graph. This is caused by the laser drifting of the leading edge. Based on this observation, it was decided to not increase the free stream velocity beyond 6.0 m/s. Besides that there was also a limit of 500 mm on the maximum displacement distance that can be measured by the laser heads.

5.4 Complete Wing Model

To determine the maximum rolling characteristics of a complete wing, the data of the wind tunnel tests has been used. In order to create maximum rolling characteristics, the main spar of the left wing is swept $3.21°$ and on the right wing $-0.80°$, shown in Figure 5.13a. With this configuration, a right wing down rolling motion is created. The left wing will create extra lift while the right wing reduces the generated lift. The lift curve slope has been reduced to 3.95 and 5.61 per radian for the simulation respectively wind tunnel test. In Figures 5.13b and 5.13c the resultant lift and rolling moment coefficient curves are shown.

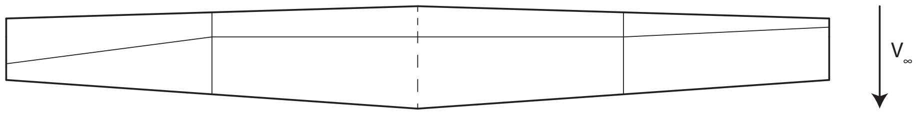

(a) Configuration of the sweepable main spar on the test article

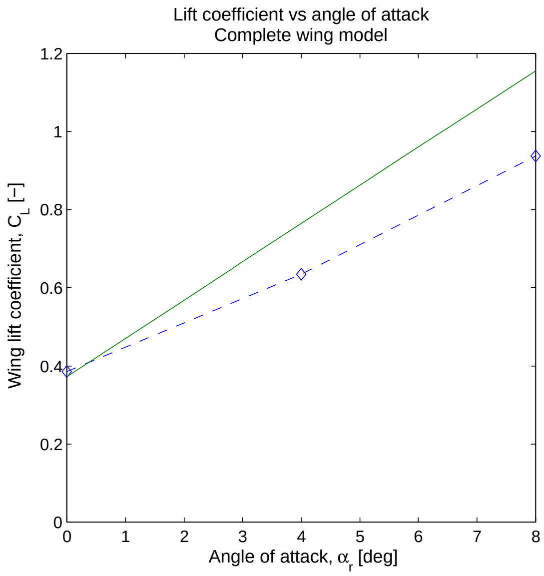

(b) Wing lift coefficient versus angle of attack

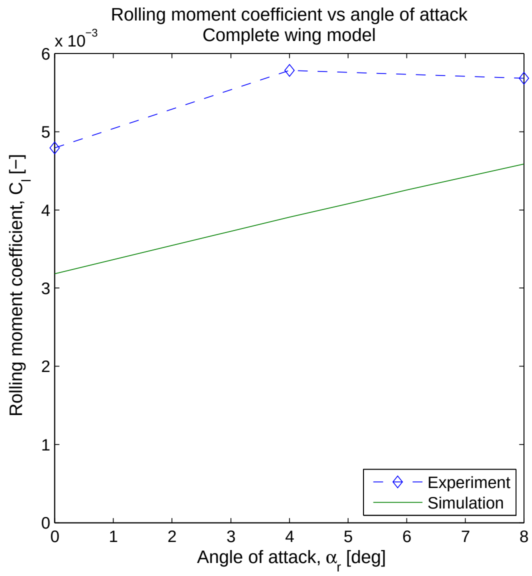

(c) Wing rolling moment coefficient versus angle of attack

Figure 5.13: Aerodynamic performance of the wing for $V = 5.0$ m/s

With the rolling moment coefficient known it is possible to calculate the roll helix angle $\frac{pb}{2V}$. For this the damping in roll coefficient of the wing is needed. The value for C_{lp} is calculated in Appendix C.2, resulting in a value of -0.393 for C_{lp}. With the following expression, given in Section 2.3.3, the helix angle can be calculated as follows

$$\frac{pb}{2V} = -\frac{C_l}{C_{lp}} \tag{5.6}$$

This resulted in a helix angle $\frac{pb}{2V}$ of $0.83°$ at an eight degree angle of attack. For the Proteus simulation the roll helix angle is $0.61°$ at the same lift coefficient. In Table 5.1 the helix angles for the other angles of attack are presented.

Table 5.1: Test article – resulting roll helix angle for $V = 5.0$ m/s

	$\alpha = 0°$	$\alpha = 2.75°$	$\alpha = 4°$	$\alpha = 5.75°$	$\alpha = 8°$	
Wind tunnel	0.70	–	0.84	–	0.83	Roll helix angle [°]
Proteus	0.46	0.54	0.57	0.61	0.67	

Comparison with Aileron Control

To get an idea about the effectiveness of the aeroelastic wing, the measurement results are compared to a conventional wing configuration with ailerons for roll control.

For the wing of the Global Hawk, shown in Figure 5.14, the aileron control effectiveness $C_{l_{\delta_a}}$ has to be determined in order to calculated the roll helix angle. The value for the aileron control effectiveness has been calculated in Appendix C, together with the roll damping coefficient C_{lp}. This resulted in the following values $C_{l_{\delta_a}} = 0.1605$ and $C_{lp} = -0.6796$.

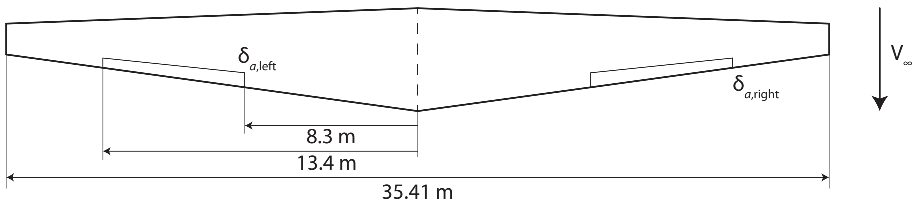

Figure 5.14: Configuration of the Global Hawk wing with ailerons

By giving both wings the same roll helix angle, an equivalent aileron deflection angle can be calculated. This is done by solving the following equation

$$- \left. \frac{C_{l_{\delta a}} \delta_a}{C_{lp}} \right|_{\text{aileron}} = - \left. \frac{C_l}{C_{lp}} \right|_{\Lambda_{sp}} \tag{5.7}$$

The equivalent aileron deflection angle has been determined to $2.96°$ and $3.51°$ for an angle of attack of $0°$ and $8°$ respectively. Where the aileron deflection angle is defined as

$$\delta_a = \frac{\delta_{a,\text{left}} - \delta_{a,\text{right}}}{2} \tag{5.8}$$

With the ailerons fully deflected, i.e. $\delta_a = 20°$, a maximum roll helix angle of $4.72°$ can be obtained. Note that aeroelastic effects have been neglected. When an aileron is deflected, the lift generated by it, causes the wing segment to twist downwards, reducing the aileron control effectiveness.

For a comparison, the roll helix angle of a Boeing 747-200 is calculated. The values for the aileron control effectiveness and roll damping coefficient are given by Roskam [46]. Roskam gives the data for three different conditions, i.e. approach, low altitude cruise (20,000 ft and Mach 0.65), and high altitude cruise (40,000 ft and Mach 0.90). The resulting helix angles are shown in Table 5.2 for an aileron deflection of $20°$. Furthermore, a large difference can be noticed between the aileron control effectiveness for the approach and cruise condition. This difference is caused by the aeroelastic effects during cruise.

For the two cruise phases of the Boeing 747-200 the test article has almost the same roll helix angle. At the approach condition, the roll helix angle of the test article is about three times lower. Since these values of the Boeing are calculated for an aileron deflection of $20°$. During a normal cruise

Table 5.2: Boeing 747-200 – Roll characteristics

	Aileron effectiveness $C_{l_{\delta a}}$ [1/rad]	**Roll damping** C_{lp} [1/rad]	**Roll helix angle** (max.) [°]
Approach	0.053	-0.502	2.11
Cruise (low altitude)	0.013	-0.340	0.76
Cruise (high altitude)	0.014	-0.320	0.88

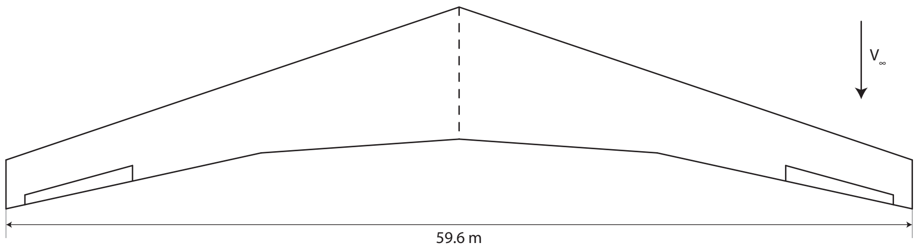

Figure 5.15: Configuration of the Boeing 747-200

flight the required aileron deflections are smaller[47]. Compared to the maximum determined helix angle for the Global Hawk wing, the obtained helix angle with the test article is about six times smaller. When aeroelastic effects are taken into account, this difference will be smaller.

The resulting roll helix angle of the test article is expected to increase with velocity and position of the elastic axis. By increasing the velocity the aerodynamic deformations of the wing are also increased, therefor the resulting rolling moment coefficient is increased. This leads to an increase of the roll helix angle.

Chapter 6

Conclusions & Recommendations

This chapter provides an overview of the conclusions drawn from the research on the performance of the active aeroelastic wing. Additionally, recommendations for future research and further development of the design tool are given.

6.1 Conclusions

In Chapter 1 the following two research questions were stated:

Given the same planform parameters, how does an Active Aeroelastic Wing compare to a conventional aileron-controlled wing?

How well can roll performance be predicted using a non-linear beam model combined with lifting line theory?

Based on the results shown in Chapter 5 these questions are answered.

How does an Active Aeroelastic Wing compare to a conventional aileron-controlled wing?

Using the AAW concept, an alternation of the elastic center at the wing was realized. The position of the elastic axis can be varied with 38% chord length by means of varying the main spar sweep angle between $-1.68°$ and $3.21°$. The variation of the elastic center position varied linear with the sweep angle of the main spar. The most forward position of the elastic center is located at 15.5% chord and the most aft position is located at 53.7% chord. In the shear modulus a reduction of ten times was possible, where the shear modulus of the inboard wing part is 20.3 MPa. The shear modulus of the aeroelastic part varies between 1.17 and 1.83 MPa, which is caused by the sweepable main spar.

During the wind tunnel tests it was shown that the sweep angle (forward and aft) of the wing had a very small effect on the rolling moment coefficient. Therefore the sweep angle was set to zero degrees on 28% chord line ($\Lambda_{0.28c} = 0°$). Furthermore, it was shown that for the most forward swept main spar the twist angle at the wing increased instead of a continuing decrease. The smaller twist angle is caused by the increase of the shear modulus for this sweep angle. Therefore the most forward position of the main spar sweep angle has been reduced to $-0.80°$. For this range of the main spar sweep angle, a maximum peak-to-peak twist angle of $1.7°$ is obtained at a velocity of 5 m/s and an angle of attack of $8°$. The effect of the main spar sweep angle on the lift coefficient was several hundredths, between 0.02 and 0.036.

To determine the characteristics of a complete wing, the results of two semi-span wing models have been used. One with a main spar sweep angle of $3.21°$ and the other with a main spar sweep angle of $-0.80°$. The obtained rolling moment coefficient C_l varies between $4.79 \cdot 10^{-3}$ and $5.68 \cdot 10^{-3}$ for a difference in main spar sweep angle of $\Delta\Lambda_{sp} = 4.0°$ and an angle of attack of $0°$ and $8°$, respectively. This variation in C_l is caused by a change in angle of attack which increases the lift force, resulting in larger twist deformations. Combining the rolling moment coefficient with the damping in roll coefficient C_{lp} of -0.393, allows it to determine the roll helix angle. This resulted in a roll helix angle varying from $0.70°$ to $0.83°$ for an angle of attack of $0°$ and $8°$, respectively. Furthermore, the roll helix angle can be increased by increasing the velocity.

Based on the results of the AAW control concept, a comparison has been made with the roll performance of the Global Hawk and Boeing 747-200, which both use ailerons for roll control. The Global Hawk has a similar wing as the test article, except for the taper ratio which is larger for the test article. To obtain the same roll helix angle of $0.83°$, with a damping in roll coefficient of -0.6796, an equivalent aileron deflection of $3.51°$ is required. With fully deflected ailerons ($\delta_a = 20°$) a maximum roll helix angle of $4.72°$ can be obtained. Note that the aeroelastic effects have not been taken into account for the Global Hawk. Therefore the equivalent aileron deflection will be larger and the roll helix angle will be reduced.

The Boeing 747-200 has a roll helix angle of $0.88°$ for the cruise condition, which is very similar to the roll helix angle of the test article. This angle is obtained when the ailerons are fully deflected ($\delta_a = 20°$). During approach conditions the roll helix angle is much larger for the Boeing. An angle of $2.11°$ can be achieved, which is three times the roll helix angle of the test article.

Based on these results it can be said that Active Aeroelastic Wing is capable of producing a large enough roll helix angle for cruise conditions when comparing the wing of the test article with a Boeing 747-200. However the roll performance should be increased for the approach condition. When comparing the Active Aeroelastic Wing to the wing of the Global Hawk one can conclude that there is a large difference in roll performance. The roll helix angle is five times higher for the wing of the test article. Note that the aeroelastic effects have not been taken into account for the Global Hawk.

How well can roll performance be predicted using a non-linear beam model and lifting line theory?

To incorporate the concept of the moveable elastic axis, Proteus has been modified to allow a change in elastic axis by specifying the sweep angle or position at the wing tip. Furthermore the aerodynamic model has been extended to incorporate the effects of cambered airfoils. For the lift calculation of the wing, the lift coefficient at zero angle of attack has been added. In addition the pitching moment has been adjusted by adding the two-dimensional aerodynamic moment coefficient to the pitching moment equation.

By comparing the lift coefficient versus angle of attack curves, a difference in lift curve slope is shown. The simulation results have a larger lift curve slope than the wind tunnel results. This difference is caused by the lifting line theory, which does not include viscous effects in the calculation. To compare the results, the corresponding angle of attack for the simulation is determined where the lift coefficient is the same as the wind tunnel tests. During the wind tunnel test the increased angle of attack resulted in ar larger measured rolling moment in comparison to the simulation results. Furthermore, the rolling moment coefficient shows a large difference when the main spar is placed at the most aft position. This difference can be caused by an incorrect distribution of the twist angle along the span.

To conclude, it can be said that Proteus is not yet capable of modeling the aeroelastic effects that are caused by a change of the elastic axis by means of a sweepable main spar.

6.2 Recommendations

Based on the research performed several recommendations can be made for further research and development. These recommendations are divided into three categories: Test article, Wind tunnel tests, and Proteus.

Test Article

- To be able to test the AAW configuration at higher velocities, the bending stiffness of the test article has to be increased to reduce the bending of the wing. This configuration can be used to determine the variation of the rolling moment coefficient with the velocity.
- Another possibility to increase the twist angle can be done by increasing the spacing between the ribs on the aeroelastic wing part. With this increased spacing the torsion stiffness can be reduced further. Therefore the resulting twist angle is increased in absolute sense.
- Find a technique that is able to determine the position of elastic center, so that the elastic axis can be implemented in a correct way.
- Find a more accurate measurement technique to determine the shear modulus. This will result in a reduction of the spread in the measurement results.

Wind Tunnel Tests

- In the current setup of the wind tunnel test only the deformations at the wing tip can be measured. By adding extra measurement points between the wing root and tip a better representation of the deformations can be obtained and used to verify the deformations of the modeling tool that is used.
- To get a more accurate curve of the rolling moment coefficient with respect to the angle of attack, the measurement points between an angle of attack of $0°$ and $8°$ should be increased. Therefore it should be easier to remove errors from the measurement results.
- When it is possible to obtain a larger roll performance, it would be of great interest to compare the drag that is produced for a certain rolling moment with an AAW and conventional wing with ailerons.

Proteus

With the use of a more sophisticated aerodynamic model (such as a vortex lattice method), the effects of cambered airfoils can be better analyzed. Therefore the use of the two-dimensional aerodynamic moment coefficient and the lift coefficient at zero angle of attack are not needed anymore. This should also fix the problem of the aerodynamic moment coefficient, which has been multiplied by three to obtain a better tip twist.

References

[1] L. R. Newcome. *Unmanned Aviation – A Brief History of Unmanned Aerial Vehicles*. AIAA, Reston, first edition, 2004. ISBN 9781563476440.

[2] Anon. U.S. Air Force - Media Gallery. `http://www.af.mil/photos/mediagallery.asp`, January 2013.

[3] R. Vos, V. Hodigere-Siddaramaiah, and J. E. Cooper. Aeroelastic flight control for subscale uavs. In *Proceedings of the 48th AIAA Structures, Structural Dynamics, and Materials Conference, Honolulu, Hawaii*, number 1706. AIAA, 23–26 April 2007.

[4] R. Bisplinghoff, H. Ashley, and R. Halfman. *Aeroelasticity*. Dover Publications, dover edition, 1996. ISBN 0486691896.

[5] S. Hulshoff. AE4-930 Aeroelasticity. Lecture notes, Delft University of Technology, 2010.

[6] E. Obert, R. Slingerland, D. J. W. Leusink, T. van den Berg, J. H. Koning, and M. J. L. van Tooren. *Aerodynamic Design of Transport Aircraft*. IOS Press, 2009. ISBN 9781586039707.

[7] T. H. G. Megson. *Aircraft Structures for Engineering Students, Fourth Edition (Elsevier Aerospace Engineering)*. Butterworth-Heinemann, fourth edition, March 2007. ISBN 0750667397.

[8] T. Theodorsen. General Theory of Aerodynamic Instability and the Mechanism of Flutter. NACA report 496, National Advisory Committee for Aeronautics, 1935.

[9] H. J. Hassig. An approximate true damping solution of the flutter equation by determinant iteration. *Journal of Aircraft*, 8(11):885–889, 1971.

[10] A. K. Jha and J. N. Kudva. Morphing Aircraft Concepts, Classifications, and Challenges. In *Smart Structures and Materials 2004: Industrial and Commercial Applications of Smart Structures Technologies*, volume 5388, pages 213 – 224. SPIE, March 2004.

[11] W. G. Holder and R. H. George. The Swingers. *Air University Review*, November 1972. URL `http://www.airpower.maxwell.af.mil/airchronicles/aureview/1972/nov-dec/holder.html`.

[12] A. R. Rodriguez. Morphing Aircraft Technology Survey. In *Proceedings of the 45th AIAA Aerospace Sciences Meeting and Exhibit, Reno, Nevada*, number 1258. AIAA, 8–11 January 2007.

[13] W. W. Gilbert. Mission Adaptive Wing System for Tactical Aircraft. *Journal of Aircraft*, 18(7): 597–602, July 1981.

[14] K. L. Bonnema and S. B. Smith. AFTI/F-111 Mission Adaptive Wing Flight Research Program. In *Proceedings of the 4th AIAA Flight Test Conference, San Diego, California*, number 2118. AIAA, 18–20 May 1988.

[15] S. G. Powers, L. D. Webb, E. L. Friend, and W. A. Lokos. Flight Test Results From a Supercritical Mission. Adaptive Wing With Smooth Variable. In *Proceedings of the 6th AIAA Biennial Flight Test Conference, Hilton Head Island, South Carolina*, number 4101. AIAA, 24–26 August 1992.

[16] S. C. Patel, M. Majji, B. S. Koh, J. L. Junkins, and O. K. Rediniotis. Morphing wing: A demonstration of aero servo elastic distributed sensing and control. 2005.

[17] H. M. Garcia, M. Abdulrahim, and R. Lind. Roll control for a micro air vehicle using active wing. In *Proceedings of the AIAA Guidance, Navigation, and Control Conference and Exhibit, Austin, Texas*, number 5347. AIAA, 11–14 August 2003.

[18] M. Abdulrahim, H. Garcia, G. F. Ivey, and R. Lind. Flight testing a micro air vehicle using morphing for aeroservoelastic control. In *Proceedings of the 45th AIAA/ASME/ASCE/AHS/ASC Structures, Structural Dynamics & Materials Conference, Palm Springs, California*, number 1674. AIAA, 19–22 April 2004.

[19] P. S. Zink, D. N. Mavris, and D. E. Raveh. Maneuver Trim Optimization Techniques for Active Aeroelastic Wings. In *Proceedings of the 41st AIAA Structures, Structural Dynamics, and Materials Conference and Exhibit, Atlanta, Georgia*, number 1330. AIAA, 3–6 April 2000.

[20] B. Perry, S. R. Cole, and G. D. Miller. A Summary of the Active Flexible Wing Program. NASA-TM 107655, NASA, July 1992.

[21] G. D. Miller. Active Flexible Wing (AFW) Technology. AFWAL-TR 87-3096, Air Force Wright Aeronautical Laboratories, February 1988.

[22] E. Pendleton, P. Flick, D. Voracek, E. Reichenbach, K. Griffin, and D. Paul. The X-53, A Summary of the Active Aeroelastic Wing Flight Research Program. In *Proceedings of the 48th AIAA Structures, Structural Dynamics, and Materials Conference, Honolulu, Hawaii*, number 1855. AIAA, 23–26 April 2007.

[23] P. C. Chen, D. Sarhaddi, R. Jha, D. D. Liu, K. Griffin, and R. Yurkovich. Variable Stiffness Spar Approach for Aircraft Maneuver Enhancement Using ASTROS. *Journal of Aircraft*, 37(5): 865–871, 20000.

[24] H. F. Parker. The Parker Variable Camber Wing. NACA report 77, National Advisory Committee for Aeronautics, 1920.

[25] M. Amprikidis and J. Cooper. Development of smart spars for active aeroelastic structures. In *Proceedings of the 44th AIAA Structures, Structural Dynamics, and Materials Conference, Norfolk, Virginia*, number 1799. AIAA, 7–10 April 2003.

[26] M. Amprikidis and J. E. Cooper. Development of Moving Spars for Active Aeroelastic Structures. In *Proceedings of Smart Structures and Materials 2003: Industrial and Commercial Applications of Smart Structures Technologies, San Diego, USA*, volume 5054, pages 16–23. SPIE, 12 August 2003.

[27] D. P. Raymer. *Aircraft Design: A Conceptual Approach*. AIAA Education. AIAA (American Institute of Aeronautics & Astronautics), fourth edition, June 2002. ISBN 9781563478291.

[28] E. Torenbeek. *Synthesis of Subsonic Airplane Design*. Kluwer Academic Publishers, repr. 1999 edition, 1982. ISBN 9789024727247.

[29] J. B. Barlow, W. H. Rae, and A. Pope. *Low-Speed Wind Tunnel Testing*. Wiley, third edition, 1999. ISBN 9780471557746.

[30] J. Mulder, W. van Staveren, J. van der Vaart, and E. de Weerdt. AE3-302 Flight Dynamics. Lecture notes, Delft University of Technology, March 2007.

[31] E. C. Polhamus. A Simple Method of Estimating the Subsonic Lift and Damping in Roll of Sweptback Wings. NACA-TN 1862, National Advisory Committee for Aeronautics, April 1949.

[32] J. B. Scarborough. Some problems on the lift and rolling moment of airplane wings. NACA-TR 200, National Advisory Committee for Aeronautics, 1925.

[33] T. A. Weisshaar, C. Nam, and A. Batista-Rodriguez. Aeroelastic Tailoring for Improved UAV Performance. In *Proceedings of the 38th AIAA Structures, Structural Dynamics, and Materials Conference and Exhibit, Long Beach, California*, number 1757. AIAA, 20–23 April 1998.

[34] Anon. Northrop Grumman RQ-4 Global Hawk. In *Jane's Unmanned Aerial Vehicles and Targets database*. Jane's, June 2011. Online edition.

[35] R. T. Fenner. *Mechanics of Solids*. Computational Mechanics and Applied Analysis Series. Blackwell Scientific Publications, repr. 1999 by crc press edition, March 1989. ISBN 9780632020188.

[36] H. J. Alons. OJF External Balance - Documentation. NLR-CR-2008 695, Dutch National Aerospace Laboratory NLR, November 2008.

[37] Anon. *High-speed, High-accuracy 1D/2D Laser Displacement Sensors*. Keyence, fourth edition, 2008.

[38] P. M. Flick, M. H. Love, and P. S. Zink. The Impact of Active Aeroelastic Wing Technology on Conceptual Aircraft Design. In *RTO AVT Specialists' Meeting on "Structural Aspects of Flexible Aircraft Control", Ottawa, Canada*, number RTO-MP-36 AC/323(AVT)TP/17 in RTO Meeting Proceedings, pages 10–1 – 10–9. NATO Science and Technology Organization, 18–20 October 1999.

[39] Anon. *ZAERO User's Manual - Engineers' Toolkit for Aeroelastic Solutions*. ZONA Technology, Inc., twenty-first edition, June 2011. URL `http://www.zonatech.com/Downloads.htm`.

[40] W. P. Rodden and E. H. Johnson. *MSC.Nastran Aeroelastic Analysis User's Guide*. MSC.Software Corporation, Santa Ana, USA, version 68 edition, 2004. URL `http://store.mscsoftware.com/books/toc/aerotoc.html`.

[41] R. de Breuker, M. M. Abdalla, and Z. Gürdal. A Generic Morphing Wing Analysis and Design Framework. In *Journal of Intelligent Material Systems and Structures*, volume 22, pages 1025–1039. SAGE Publications, July 2011.

[42] J. Weissinger. The Lift Distribution of Swept-Back Wings. NACA-TM 1120, National Advisory Committee for Aeronautics, March 1947.

[43] R. de Breuker. *Energy-based Aeroelastic Analysis and Optimisation of Morphing Wings*. PhD thesis, Delft University of Technology, August 2011.

[44] R. de Breuker and J. H. van Emden. Timoshenko stiffness matrix. Personal Communication, 2012.

[45] R. M. Pinkerton and H. Greenberg. Aerodynamic characteristics of a large number of airfoils tested in the variable-density wind tunnel. NACA-TR 628, National Advisory Committee for Aeronautics, 1938.

[46] J. Roskam. *Airplane Flight Dynamics and Automatic Flight Controls*. Number Part 1. DARcorporation, 2001. ISBN 9781884885179.

[47] T. J. Mulder and J. H. van Emden. Aileron deflection and roll rates of commercial aircraft. Personal Communication, 2012.

Appendix A

Rectangular Beams

To determine the influence of an increase of the aspect ratio on the stiffness of a slender wing, the wing is replaced by a thin walled beam with wall thickness t, width a, height b, length L and $t \ll a, b$.

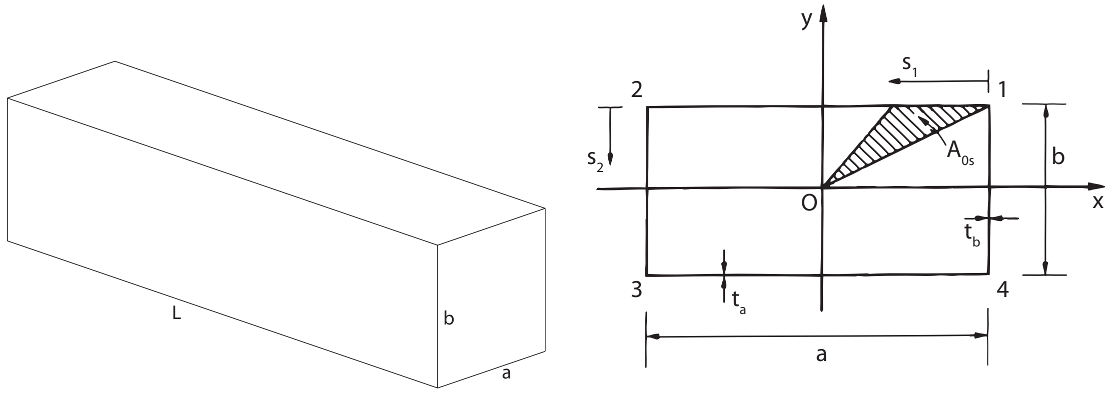

(a) Three dimensional beam (b) Torsion of a rectangular section beam[7]

Figure A.1: Rectangular beam

The aspect ratio can be defined as:

$$\mathcal{R} = \frac{b^2}{S} \tag{A.1}$$

$$= \frac{4L^2}{2La} = \frac{2L}{a} \tag{A.2}$$

A.1 Bending

Calculation of the deflection of a beam with a force F placed in the middle at the tip can be done by[35]:

$$\delta = \frac{FL^3}{3EI} \tag{A.3}$$

The second moment of inertia of a thin walled rectangular about the x-axis is:

$$I_{xx} = \frac{atb^2}{3} \tag{A.4}$$

Implementing the expression for the second moment of inertia into Equation (A.5) and introducing the aspect ratio gives equation (A.6).

$$\delta = \frac{FL^3}{Eab^2t} \tag{A.5}$$

$$= \frac{FL^2}{2Eb^2t}\text{Æ} \tag{A.6}$$

Bending stiffness of the beam is determined by Equation (A.7). Increasing the aspect ratio result in a larger deflection and thus in a lower bending stiffness.

$$K_h = \frac{F}{v_b} \tag{A.7}$$

A.2 Torsion

By moving the force from the previous section to the corner a torque is produced around the center of the section. The resulting twist can be calculated by[7]:

$$\theta = \frac{TL}{4a^2b^2G}\left(\frac{a}{t_a} + \frac{b}{t_b}\right) \tag{A.8}$$

Implementing the aspect ratio, Equation (A.2), into the twist angle:

$$\theta = \frac{T}{8ab^2G}\text{Æ}\left(\frac{a}{t_a} + \frac{b}{t_b}\right) \tag{A.9}$$

With an increase of the aspect ratio, the twist angle is also increased, resulting in a reduced torsional stiffness of the beam (Equation (A.10)).

$$K_\theta = \frac{T}{\theta} \tag{A.10}$$

Appendix B

Boundary Corrections Factors

The boundary corrections made in Section 3.3.2 depend on two correction factors, τ_2 and δ. The increase of boundary induced upwash at a point P behind the wing quarter chord is represented by τ_2.

For the OJF the aspect ratio is equal to 1.0. Therefore the correction for the octagonal jet are essentially those of a circular-arc jet, according to Barlow et al.[29]. This is the ratio of wind tunnel jet given by:

$$\lambda = \frac{h}{B} \tag{B.1}$$

From Figure B.1 the vortex span is determined of 0.8 which leads to an effective vortex span, b_e, of $0.9b$ by using Equation (B.2). With the effective vortex span known the span-to-tunnel-width ratio, k, can be calculated using Equation (B.3) resulting in 0.474.

$$b_e = \frac{b + b_v}{2} \tag{B.2}$$

$$k = \frac{b_e}{B} \tag{B.3}$$

With the usage of Figures B.2 and B.3 the boundary and downwash corrections are determined

$$\delta = -0.127$$
$$\tau_2 = 0.0360$$

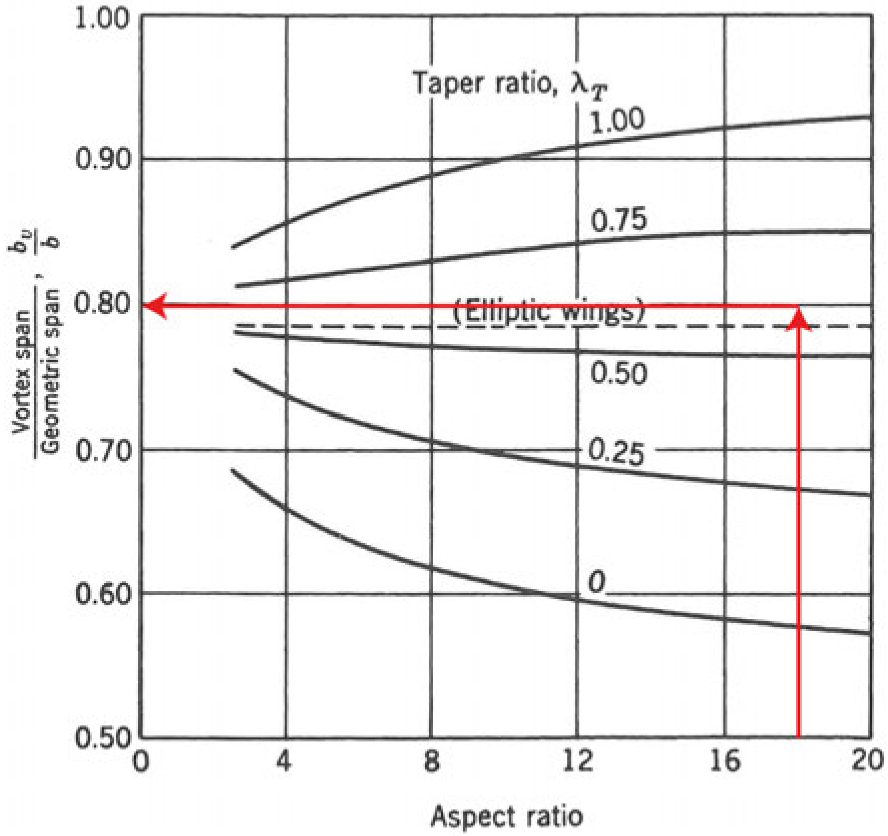

Figure B.1: Values of vortex span for elliptic, rectangular, and tapered wings[29]

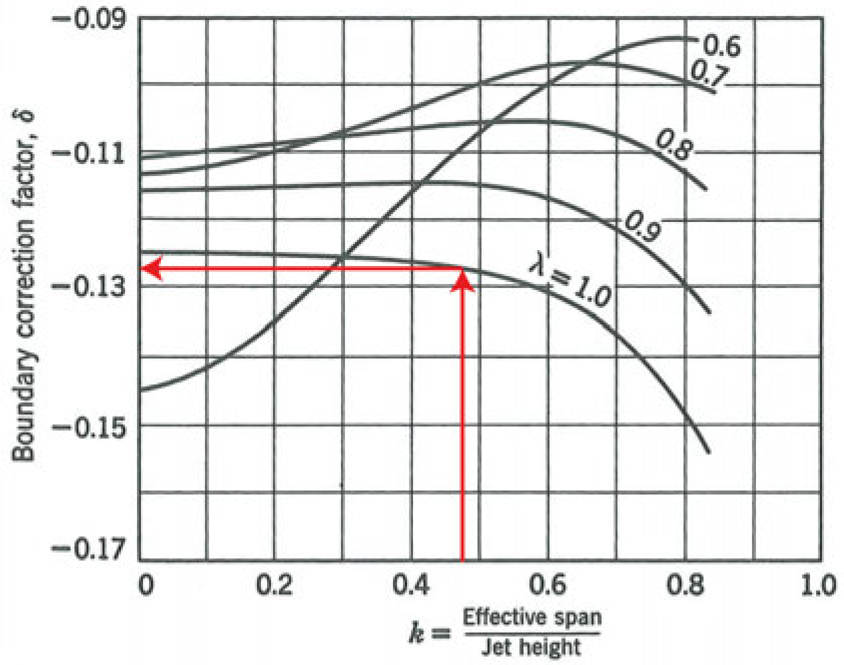

Figure B.2: Values for δ for a wing with uniform loading in an open circular-arc wind tunnel[29]

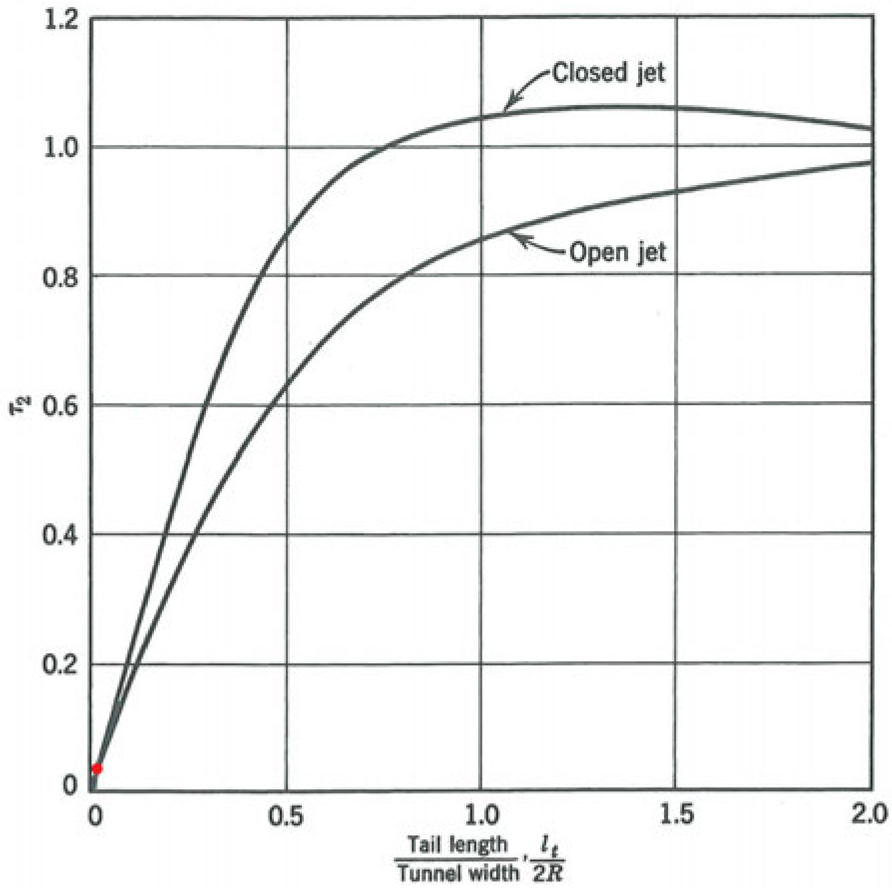

Figure B.3: Values for τ_2 for open and closed circular jets[29]

Appendix C

Rolling Parameters

In this chapter the aileron control effectiveness of the Global Hawk, and the roll damping coefficient of the Global Hawk and test article are determined. Both parameters are needed to calculate the steady state roll rate.

In Table C.1 the required properties of the Global Hawk are given. The values of the properties are retrieved from Jane's Unmanned Aerial Vehicles and Targets database[34].

Table C.1: Global Hawk - wing characteristics

Property		Value	Property		Value
Wing span	b	35.41 m	Airfoil		LRN1015
Wing area	S	50.17 m^2	Thickness to chord ratio	$\frac{t}{c}$	0.152
Aspect ratio	AR	25	Section lift curve slope	c_{l_α}	2π
Taper ratio	λ	0.33			
Sweep angle	$\Lambda_{c/4}$	5.9°	Inner position aileron	y_i	8.3 m
Root chord length	c_r	2.1 m	Outer position aileron	y_o	13.4 m
True airspeed	V_{TAS}	177 m/s	Aileron to chord ratio	$\frac{c_a}{c}$	0.20
Mach number	M	0.60	Maximum aileron deflection	$\delta_{a,\,\text{max}}$	20°

C.1 Aileron Control Effectiveness of the Global Hawk

The aileron control effectiveness of the Global Hawk can be determined by using the equations shown in Section 2.3.1. Therefore the following parameters need to be determined: the theoretical flap lift factor α_δ, and the lift effectiveness factor η_δ. From Figure C.1 these parameters are derived, resulting in a value of 0.55 for α_δ. This is based on an aileron to chord ratio of 0.20 and an effectiveness factor of 0.61 for η_δ assuming that the gap between the wing and aileron is closed and for a deflection angle of 20°.

This resulted in a $C_{l_{\delta_a}}$ of 0.1605 using Equation (2.7).

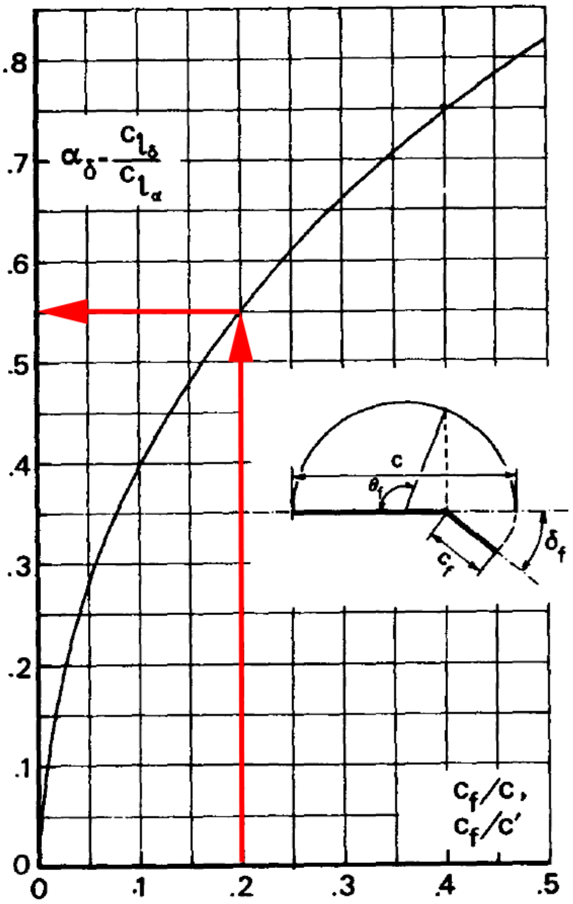

(a) Theoretical flap lift factor[28]

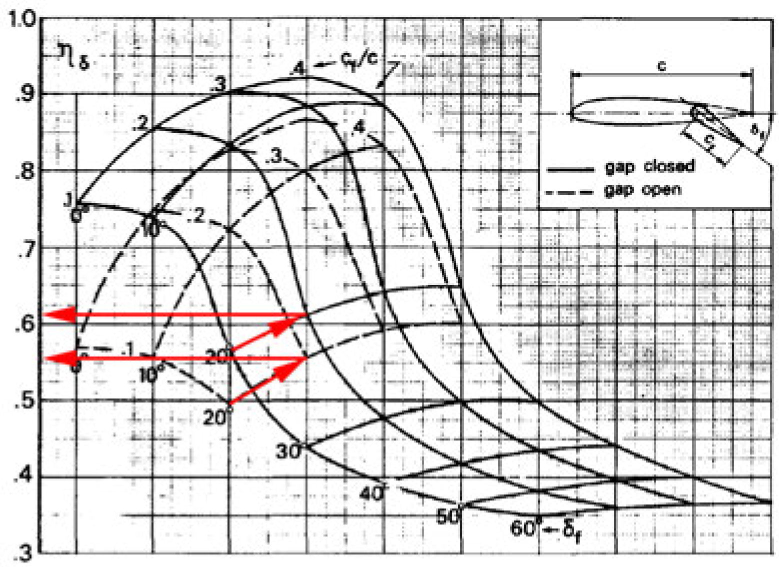

(b) Lift effectiveness factor for plain flaps (derived from experimental data)[28]

Figure C.1: Determine the characteristics of a plain flap

C.2 Damping in Roll

The roll damping for the Global Hawk and test article are determined in the following sections based on the formulas given in Section 2.3.2.

Global Hawk

To determine the roll damping coefficient for the Global Hawk, the section lift curve slope, the aspect ratio and quarter chord sweep angle are required. Since the Global Hawk is flying at a Mach number of 0.6, compressibility effects have to be considered. Therefore an equivalent aspect ratio is calculated by

$$A\!\!R_{\mathrm{e}} = A\!\!R\sqrt{1 - M^2} \tag{C.1}$$

and the equivalent quarter chord sweep angle is calculated by using

$$\tan \Lambda_{c/4,\,\mathrm{e}} = \frac{\tan \Lambda_{c/4}}{\sqrt{1 - M^2}} \tag{C.2}$$

which corrects the parameters with the Prandtl-Glauert factor.[31] This results in a $A\!\!R_{\mathrm{e}}$ of 20 and a $\Lambda_{c/4,\,\mathrm{e}}$ of $7.4°$.

Polhamus[31] created a diagram, shown in Figure C.2, to determine $\frac{\bar{y}_{L'_p}}{b/2}$, the effective lateral center of pressure for rolling moment due to rolling. This method should only be used as an approximate in estimating the taper effects of swept wings since it neglects any sweep effect on the spanwise position of the center of pressure. Furthermore, the results are extrapolated for an aspect ratio of 25. This resulted in a value of 0.485 for the effective lateral center of pressure.

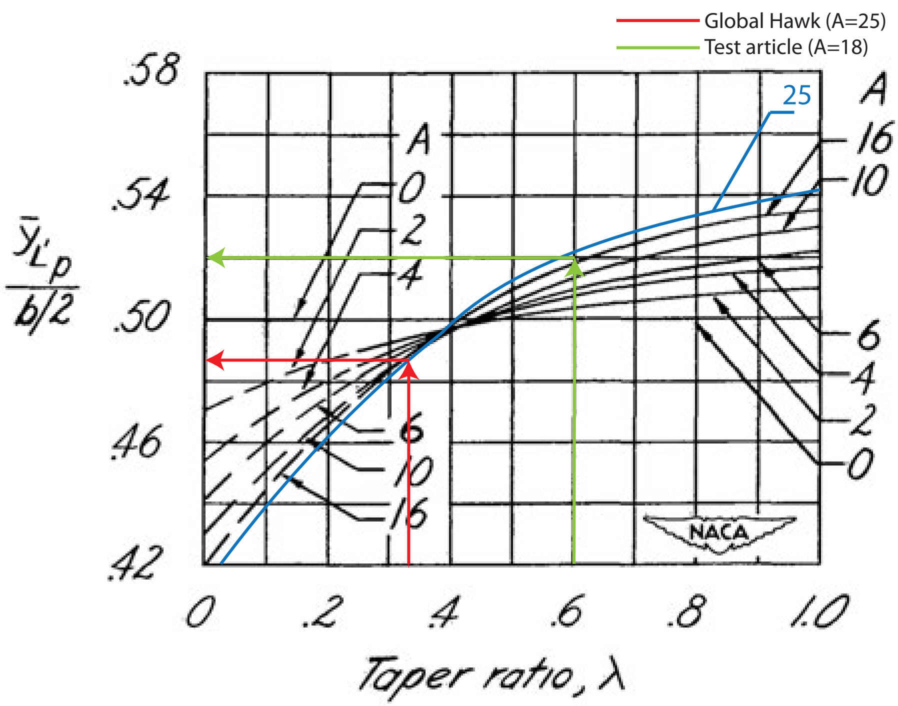

Figure C.2: Variation of the effective lateral center of pressure for rolling moment due to rolling with aspect ratio and taper ratio.[31]

This results in a damping in roll coefficient of -0.6796 for the Global Hawk.

Test Article

For the test article the roll damping coefficient is also determined. However, the aspect ratio and quarter chord sweep angle did not have to be corrected for compressibility effects. This resulted in an effective lateral center of pressure of 0.520.

With the effective lateral center of pressure known a roll damping coefficient of -0.3933 is determined for the test article.